POLITECNICO DI MILANO

Dipartimento di Fisica

Corso di Laurea in Ingegneria Fisica

RESONANT X-RAY SPECTROSCOPY OF FRACTAL TiO_2 STRUCTURES FOR PHOTOVOLTAIC APPLICATIONS

Relatore: Prof. Giacomo Ghiringhelli

Correlatore: Dott. Pieter Glatzel

Tesi di Laurea di

Matteo BIANCHINI

Matr. N. 750616

Anno Accademico 2011-2012

Alla mia famiglia,
per aver sempre sostenuto le mie scelte
e incoraggiato il mio cammino,
e ai miei amici,
per averlo reso indimenticabile.

Sommario

Dalla sua prima osservazione nel 1947 al General Electric Research Laboratory di New York, la radiazione di sincrotrone è stata usata in maniera crescente dalla comunità scientifica, grazie allo sviluppo di strutture in grado di sfruttarla come strumento per studiare il mondo su scala nanometrica, ovvero il dominio di atomi e molecole. La terza generazione di sincrotroni, strutture in grado di generare raggi x in maniera intensa e altamente direzionale, ha reso possibili varie tipologie di applicazione grazie alla loro possibilità di raggiungere potenza e brillanza fino a livelli molto elevati, nonché di ottenere un'ottima risoluzione spaziale, temporale o di energia (e spesso molte di esse tutte assieme). Uno degli utilizzi più comuni della luce di sincrotrone riguarda la spettroscopia, ovvero in generale lo studio dell'assorbimento o dell'emissione di particelle (fotoni, elettroni, neutroni ecc) da parte di un determinato materiale, in funzione della loro energia. Ovviamente nel caso considerato la tecnica utilizza fotoni ad alta energia, ovvero raggi X, per studiare le proprietà dei materiali, i quali mostrano comportamenti differenti a seconda delle loro caratteristiche e della loro struttura elettronica. Una delle proprietà più importanti di tale spettroscopia è la possibilità di essere assolutamente selettivi sull'elemento chimico che si vuol andare ad osservare, studiando il comportamento suo e degli atomi in un suo intorno, grazie alla possibilità di selezionare con precisione l'energia sulla soglia di assorbimento di quel determinato elemento. Tra le molte tecniche spettroscopiche, in questa tesi si sono utilizzate la XANES (X-ray Absorption Near Edge Structure), con cui è possibile studiare i livelli energetici non occupati al di sopra dell'energia di Fermi e la XES (X-ray Emission Spectroscopy), che è in qualche modo complementare e con cui si possono osservare quelli occupati al di sotto dell'energia di Fermi, ottenendo così un quadro completo di tutta la struttura elettronica. Si è infine usata la tecnica RIXS (Resonant Inelastic X-ray Scattering), che è una tecnica più completa poiché permette di combinare i due processi in un processo del second'ordine photon-in photon-out che fornisce una mappa bidimensionale ricca di informazioni riguardo la struttura elettronica.

I primi due capitoli di questa tesi sono dedicati alla descrizione della radiazione di sincrotrone e delle sue proprietà, assieme alle strutture che sono necessarie alla sua generazione ed al suo sfruttamento, e ad una descrizione dettagliata delle tecniche spettroscopiche di cui sopra. Tra la grande varietà di materiali studiati al sincrotrone, un posto di rilievo è occupato da quelli con alto interesse tecnologico e grandi potenzialità di sfruttamento nell'industria. In questa tesi, in particolare, ci si è concentrati sull'ossido di titanio (TiO_2) che è un materiale semiconduttore molto studiato per le sue proprietà catalitiche e fotovoltaiche. La sua importanza è cresciuta soprattutto da quando, nel 1991, è stato utilizzato come fotoanodo in una nuova tipologia di cella fotovoltaica elettrochimica, detta dye sensitized solar cell (DSSC) o cella di Grätzel, dal nome del suo inventore. Questo particolare tipo di cella ibrida sfrutta l'assorbimento di radiazione visibile da parte di un colorante che, essendo deposto sulla superficie dell'ossido di titanio, gli trasferisce elettroni fotoeccitati. Questi possono così dar luogo ad una corrente tramite il dispositivo il cui circuito è chiuso da un elettrolita che rigenera il colorante. Le celle di Grätzel sono molto interessanti per il loro basso costo e la loro discreta efficienza, che tuttavia non è ancora comparabile con quella che si può ottenere dal silicio monocristallino. Per questo motivo molta ricerca è indirizzata verso l'ottimizzazione dei vari processi che prendono parte alla generazione di corrente nella cella. Il capitolo quattro della tesi è appunto dedicato alla descrizione della fisica che governa il funzionamento di tali celle, con particolare attenzione al fatto che esse possano essere migliorate tramite l'utilizzo di fotoanodi nanostrutturati che diano la possibilità di aumentare l'assorbimento di luce nella cella grazie al fatto che essi massimizzano il rapporto superficie-volume, così da aumentare l'efficienza nel trasferimento di elettroni all'interfaccia colorante/semiconduttore. In particolare qui si è voluto studiare, utilizzando le tecniche di spettroscopia con luce di sincrotrone di cui sopra, l'interazione del TiO_2 con il colorante e come questo ne modifichi la struttura elettronica, in campioni di ossido di titanio che non è normalmente nanostrutturato, bensì che è stato deposto con una particolare tecnica nota come PLD (pulsed laser deposition) che permette di strutturarne la morfologia così che le nanoparticelle di ossido si assemblino anisotropicamente dal basso verso l'alto, in modo che la struttura ricordi un albero e che tutto il fotoanodo ricordi una foresta.

In questo modo è possibile massimizzare il rapporto tra superficie libera e volume e dunque migliorare lo scambio di elettroni tra anodo e colorante.
Nell'ultimo capitolo sono mostrati i dati sperimentali ottenuti alla beamline ID26 della European Synchrotron Radiation Facility (ESRF) tramite XANES, XES e RIXS. In particolare, tali tecniche sono state usate alla soglia K del titanio su un campione di diossido di titanio nanostrutturato e su un analogo campione ricoperto da un monostrato del colorante noto in letteratura come "black dye". Si è poi svolta un'analisi dei dati per confrontare i due campioni, con attenzione specifica alla ricerca di eventuali modifiche nei levelli energetici a ridosso dell'energia di Fermi ad opera del colorante. Tali modifiche, che sono state osservate, non erano affatto scontate poiché la spettroscopia di raggi X, a differenza di quella di elettroni, è una tecnica più sensibile al bulk dei materiali che alla loro superficie, ad indicare la rilevanza della morfologia di quest'ultima nei suddetti campioni e una profonda interazione tra molecole di colorante ed atomi del semiconduttore.

Infine, è opportuno sottolineare che il terzo capitolo della tesi è invece dedicato ad un progetto differente, ovvero al software X-count, un codice matlab che è stato sviluppato ad ESRF come strumento di supporto per la spettroscopia photon-in photon-out. Questo significa che il programma simula tutto l'insieme dei processi di assorbimento di raggi x da parte di un atomo assorbitore posto all'interno di un campione più complesso e della sua emissione di fluorescenza, ovvero di ulteriori raggi x ad energia differente che vengono poi rivelati da un detector che può essere a stato solido oppure un normale APD posto all'interno di uno spettrometro. Tale software è utile perché permette di simulare un esperimento e di verificare se da esso sia possibile ottenere un sufficiente segnale in uscita o, in caso contrario, quali parametri sia opportuno ottimizzare per ottenerlo. Esso permette inoltre di simulare molti effetti secondari ma importanti che avvengono nei campioni reali, dove lo spessore o l'elevata concentrazione o la presenza di altre specie atomiche che possano assorbire la radiazione possono modificare significativamente il risultato di un esperimento. Queste possibilità svolgono un ruolo cruciale nel mondo del sincrotrone dove i tempi per fare misure, i cosiddetti beamtimes, sono ridotti e dunque la pianificazione dell'esperimento è un elemento chiave per poter ottenere misure utili e complete.

Contents

Introduction

From its first observation in 1947 at the General Electric Research Laboratory in New York, synchrotron radiation has been increasingly used by the scientific community thanks to the development of facilities able to exploit this sort of radiation as a tool to investigate the world down to the scale of nanometers and angstroms, i.e. the world of atoms and molecules. Third generation synchrotron facilities, structures able to generate very intense and directional x-rays, made many different applications possible thanks to the chance to exploit power and brilliance of radiation, together with that one to choose spatial, temporal and energetic resolution. In this thesis an important application of synchrotron radiation is discussed, namely x-ray spectroscopy. Such a technique studies the properties of materials by observing x-ray absorption and emission, which depends on the material itself and on its electronic structure. This needs the ability to govern x-rays' energy which can be achieved at synchrotrons. Moreover, this gives to spectroscopy its peculiar characteristic of being element selective, i.e. able to probe only the selected element and to observe how it behaves accordingly to its neighborhood.

The first two chapter of this thesis are dedicated to the description of synchrotron radiation and its properties, together with the facilities that support its generation and exploitation, and to an overview of spectroscopic techniques which are currently used. In fact, spectroscopy developed and improved and many techniques such as XANES (x-ray absorption near edge structure)[1], XES (x-ray emission spectroscopy)[2] and RIXS (resonant inelastic x-ray scattering)[3], became available to study the absorption and emission of x-rays from samples of every kind. XANES, in particular, probes the unoccupied levels above the Fermi energy and thus it is an interesting tool to study the electronic structure in this energy range. Somehow

complementary is XES, which probes the occupied levels below the Fermi energy (valence levels); for this reason the two techniques can give a full understanding of the whole electronic structure in the neighborhood of the considered element. RIXS is an even more complete technique, because it combines the two processes in a second order photon-in photon-out technique which provides a bidimensional map rich of informations about the electronic structure.

In this thesis the techniques above were exploited to study titanium dioxide (TiO_2), a semiconductor material of great interest in the fields of catalysis[4] and photovoltaic energy generation[5]. Indeed, this material is employed as a photoanode in Dye Sensitized Solar Cells (DSSCs) which are an interesting and promising alternative to silicon based solar cells, since they are hybrid cells with very low production cost. Together with such a photoanode, indeed, there is a dye which provides the light absorption and an electrolyte (a redox couple) which closes the circuit between it and the dye, since it makes the electron recombination possible. Particularly, the physics of these cells (also known as Grätzel cells[6]) is described in chapter four and special attention is given to the fact that they can be improved by the use of nanostructured TiO_2 photoanodes that give the possibility to increase the light absorption of the cell because they maximize the surface-to-volume ratio and give the highest efficiency of electron transfer at the dye/semiconductor interface. In the attempt to find an even better efficiency, photoanodes were deposited at Politecnico di Milano using Pulsed Laser Deposition (PLD), a technique that allows to confer to TiO_2 a peculiar morphology, resembling that one of a forest[7] where every tree contributes to obtain an extremely high surface. These structures with extreme porosity were proved to be useful to hamper electron recombination and improve electron transport[8]; thus their properties are studied for a possible use in industrial devices. For this reason, in the final part of this thesis a sample of nanostructured TiO_2 and a similar sample sensitized with "black dye"[9] were studied by means of XANES, XES and RIXS spectroscopies performed on the K edge of titanium in order to figure out the influence of such a dye on the semiconductor, since a better understanding of the physics that governs the electronic structure of these complex interfaces is necessary to obtain better efficiencies and therefore better photovoltaic devices. In particular, data

analysis was addressed to understand whether there were differences in the energetic levels close to the Fermi energy between the sample with and without dye. Such modifications were observed, although this was not clearly predictable from the beginning because x-ray spectroscopy (differently than electron spectroscopies) is more a bulk sensitive technique than a surface sensitive one. Thus this means that the interaction between the dye molecules and the semiconductor atoms is deeper than expected and that surface atoms have a dominant contribution in the sample.

Besides, chapter three of this thesis is a parenthesis that wants do describe X-count, a Matlab-based software that was developed at the European Synchrotron Radiation Facility to simulate the whole absorption and emission process, from the incident X-rays, via their interaction with the absorber atoms in the sample, to the fluorescent emission of another X-ray photon and its collection from a detector. This program mainly answers to the necessity to estimate the result of an experiment before performing it, since during beamtimes scientists have not much time and they must know whether an experiment is possible or not, i.e. if it gives an useful signal and which are the critical factors to improve it. Also, X-count gives the possibility to simulate and estimate many further effects, such as self absorption or emission of fluorescence from other atoms in the sample than the absorber atom. Thanks to these skills and to its utility, the program is currently used at the ESRF to support the planning of many experiments and this will hopefully bring to its further improvement.

Chapter 1

Theory of X-ray absorption and emission

The electromagnetic radiation spectrum covers a wide range of energies, ranging from radio waves up to gamma rays. About halfway in this huge interval there is visible light, which is the radiation we are most used to. Many different factors determine its behavior, like intensity, polarization and wavelength. They are all important because they establish how light interacts with matter but the last, particularly, is crucial to determine the size of the objects we can see. The wavelength of visible light spans between 300 and 800 nm, i.e. an order of magnitude of 10^{-6} to 10^{-7} meters. This is approximately the size of a bacterium, which is why we can see them (and all objects bigger than them) under a microscope.

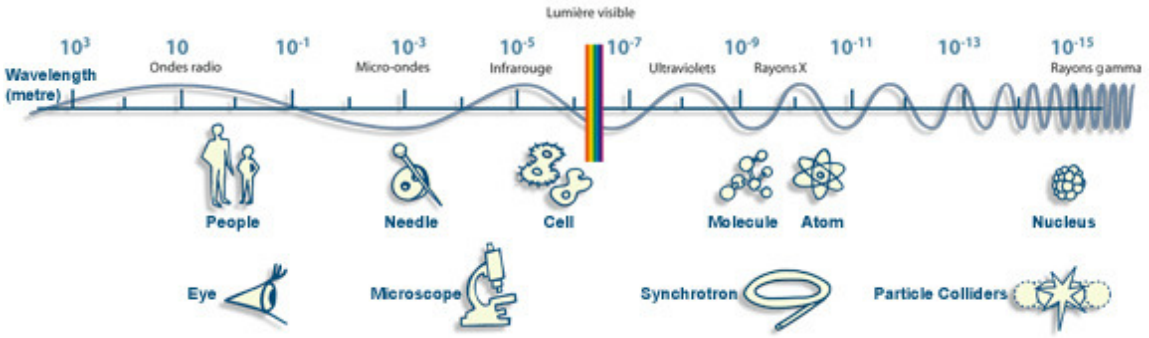

Figure 1.1: The electromagnetic spectrum of radiation, compared with the size of common objects[10].

Therefore, if we want to observe smaller objects like molecules or atoms we need

shorter wavelengths. As we can see in Figure 1.1, X-rays have wavelengths of about 10^{-10} m (1 Å), which coincide with the usual inter-atomic distance. For this reason, X-rays can be used to probe the atomic structure of matter. In the following it will be explained how X-rays interact with matter and a number of spectroscopic techniques will be shown, which can be used to extract electronic, structural or chemical informations from a variety of samples.

1.1 X-ray interaction with matter

X-rays were discovered by Wilhem C. Röntgen in 1895 when he used electrons to bombard inert gas in tubes and discovered that, nearby, photographic plates had been exposed by some sort of unknown, "X", radiation. He received the first Nobel Prize in Physics in 1901 for his discovery. He also noticed the great penetrating power of x-rays and used it to take pictures of human bones. Figure 1.2 shows one of the first pictures that Röntgen took, i.e. one of the first X-ray photographs. It takes advantage of the difference in X-ray transmission in tissue, mainly composed of water and organic molecules, and bones which contain a lot of calcium and therefore exhibit lower X-ray transmission. Various evidences came up later about reflection, refraction, diffraction and polarization of x-rays and scientists were able to prove them to be high-energy electromagnetic radiation. From a quantum mechanical point of view, x-rays are photons of high energy, given by $E = h\nu$, and momentum $p = \frac{h}{\lambda}$, where ν is the radiation frequency, h Planck's constant and λ the radiation wavelength ($\lambda = c/\nu$ with c speed of light). The relation between wavelength (in Å) and energy (in KeV) can be expressed as:

$$\lambda[\,\mathring{A}\,] = \frac{hc}{E} = \frac{12.398}{E[KeV]}. \tag{1.1}$$

Many different interactions can take place between x-ray photons and matter, depending mainly on the energy of the photons (indeed, a photon is considered in the x-ray range when it has energies from hundreds of eV to about a MeV). Usually this interaction is quantified by a cross section, defined as

$$\frac{\mathrm{d}\sigma}{\mathrm{d}\Omega} = \frac{I(\theta,\varphi)}{I_0} \tag{1.2}$$

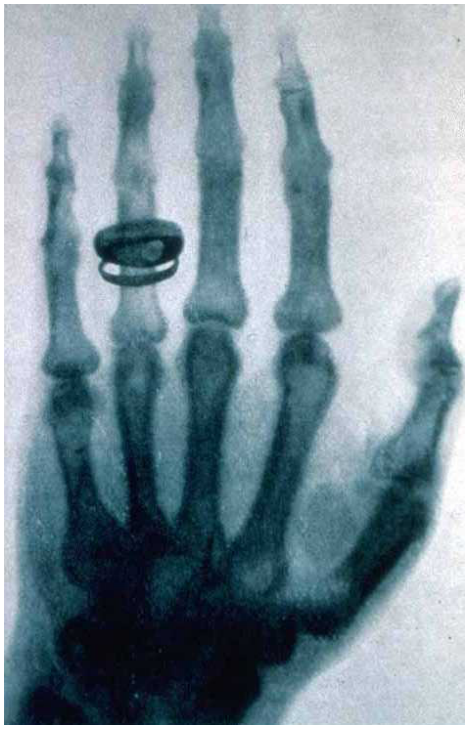

Figure 1.2: The hand of Röntgen's friend Alfred von Kölliker in one of the first x-ray photographs[11].

where I_0 is the incident flux of photons and $I(\theta, \varphi)$ is the number of events per second in the differential solid angle $\mathrm{d}\Omega = \sin\theta \mathrm{d}\theta \mathrm{d}\varphi$. The total cross section per atom σ is found by integrating the differential cross section over the whole solid angle.

As can be seen in Figure 1.3, depending on the photon energy different processes can dominate the interaction. In the range from hundreds to a few tens of thousands of eV (the range of energies that are usually produced in modern laboratories and synchrotron facilities) the most important interaction is the photoelectric one, even though coherent elastic scattering and incoherent inelastic Compton scattering also take place.

1.2 The photoelectric effect

Albert Einstein was the first to propose the idea of light formed by quanta, or discrete energy packages called photons. In 1905, he used this concept to explain the photoelectric effect and for this reason he received the Noble prize in 1921. His simple picture in terms of absorption of discrete quanta of light explained the features of

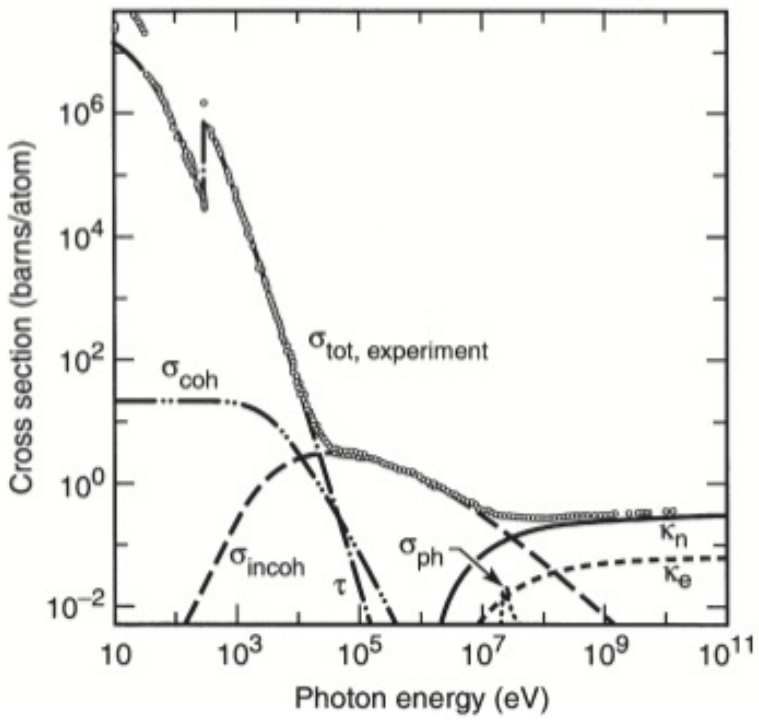

Figure 1.3: Total cross section of Carbon. The picture shows how such a cross section is given by the sum of the contributions coming from many different processes, namely coherent and incoherent scattering, photoelectric effect and pairs production[12].

the phenomenon and its characteristic frequency. Mostly, it could explain why this effect took place only when light with frequency higher than a certain minimum level was shaded on the sample, while it did not take place for frequencies lower than that, no matter how intense the light was. In fact, in the photoelectric effect a photon is absorbed by the material of interest and as a result an electron is excited to a higher energetic level and usually emitted from the sample, which is therefore ionized. The energy of the photon, expressed as $h\nu$, is related to the kinetic energy of the emitted electron E_{kin} via:

$$h\nu = h\nu_0 + E_{kin} + \phi_0 \tag{1.3}$$

where $h\nu_0$ is simply the binding energy, i.e. the energy needed to liberate the electron from the material and ϕ_0 is the work function which appears in solids because of the potential energy barrier that electrons find at the surface. In simple terms this means that the kinetic energy of the emitted electron is equal to the energy that the photon transferred to it, minus the energy needed to overcome the Fermi energy level. This

also means that, if the energy of the photon is lower than the binding energy, no photoelectric effect takes place.

Starting from this first step, quantum mechanics made enormous progresses in the description of photons' interaction with electrons present in matter. In the framework of time-dependent perturbation theory an important expression in derived, namely the Fermi golden rule[13, 14], that allows to estimate the transition probability $\Gamma_{i,f}$ from an initial state to a final one, described by the multi-electron wave functions $|i>$ and $|f>$, respectively, via a generic interaction Hamiltonian H_{int} :

$$\Gamma_{i,f} = \frac{2\pi}{\hbar^2}| < f|H_{int}|i > |^2 \delta(h\nu - E_i + E_f) \ . \tag{1.4}$$

When H_{int} represents the hamiltonian of the electromagnetic field, this equation governs every electronic transition within the atom and therefore it governs x-ray absorption and emission. Also, it determines the selection rules that shall be obeyed in order to observe a transition. Indeed, a closest look at the element in modulus squared in eq.1.4, called matrix element M, writing explicitely the Hamiltonian and considering a resonant transition, reveals

$$M \propto | \int \psi_f^*(\hat{\epsilon} \cdot \vec{r}) e^{i(\vec{k} \cdot \vec{r})} \psi_i \mathrm{d}^3 x|^2. \tag{1.5}$$

In the easiest case, H_{int} can be treated in the electric dipole approximation. This considers the wavelength of radiation bigger than the interaction length with the system, so that the field can be considered constant in it and the exponential term of the plane wave $\exp\left[i(\omega t - \vec{k} \cdot \vec{r})\right]$ can be approximated to 1. Thus, the interaction is reduced to $e\vec{\epsilon} \cdot \vec{r}$ where e is the electron charge, $\vec{\epsilon}$ is the polarization versor of the x-ray and $\vec{r}$ is the electron's position coordinate. In this approximation, when ψ refers to a hydrogen-like wavefunction, the selection rules coming from the integral in 1.4 are $\Delta l = \pm 1, \Delta m = 0, \pm 1$ and $\Delta S = 0$. Of course, many effects can modify these rules, like, e.g., spin-orbit coupling.

However, it should be noted that for x-rays the dipole approximation is often inappropriate, since their wavelength is short. For this reason it is often important to consider quadrupole transitions [15], where the space-dependent part of $\exp[i(\omega t - \vec{k} \cdot \vec{r})]$ is expanded to $1 - i\vec{k} \cdot \vec{r}$. The matrix element has then an additional term

$$M \propto | \int \psi_f^* \left[i(\hat{\epsilon} \cdot \vec{r})(\vec{k} \cdot \vec{r}) \right] \psi_i \mathrm{d}^3 x|^2. \tag{1.6}$$

This brings to different selection rules and allows to observe many further transition (quadrupole transitions obey $\Delta l = 0, \pm 2$ e.g. $1s - 3d$ transitions), although their probability is much smaller (for K-edges, quadrupole corrections are smaller than dipole ones by a quantity of order $(Z\alpha)^2$, where Z is the atomic number and $\alpha \approx 1/137$ is the fine structure constant). A schematic picture of x-ray absorption by an atom and consequent electron emission is shown in Figure 1.4.

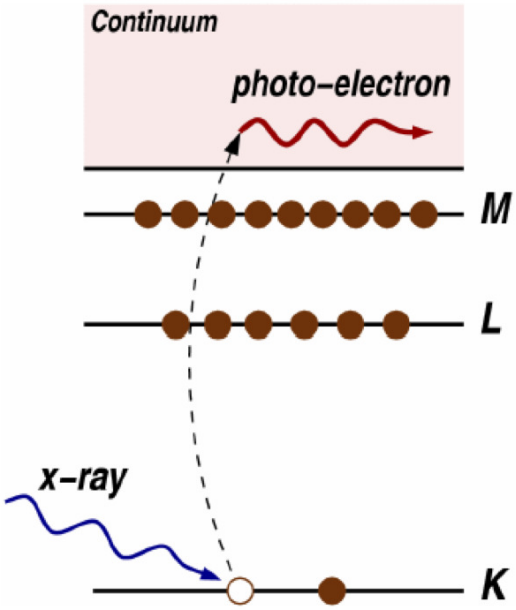

Figure 1.4: Core levels with their classic nomenclature of K, L and M. A transition from $1s$ level to the continuum above the Fermi level is also indicated[16].

The nomenclature for x-ray absorption features reflects the core orbital from which the absorption originates. In the figure above, the three innermost core orbitals are shown, namely the K, L and M shells and a characteristic transitions to the continuum states is indicated. For example, K edges refer to transitions from the innermost $n = 1$ electron orbital (thus the K edge involves $1s$ electrons), whereas L edges refer to the $n = 2$ absorbing electrons (L_1 to $2s$, L_2 to $2p_{1/2}$, and L_3 to $2p_{3/2}$ orbitals, shown in the figure as a unique line), to the corresponding higher-lying bound core shells and continuum states. The transitions happen from core levels to unoccupied states, i.e., to states above the Fermi energy E_f, leaving behind a core hole; nevertheless, absorption features may also appear just below the edge, which correspond to transitions to bound unoccupied levels just below the ionization

limit. Above such a limit, the excited electron is considered as a photoelectron, and depending on its kinetic energy, it can propagate more or less freely through the material. The photoelectron propagation can be approximated by a spherical wave with a kinetic energy E_{kin} given by eq.1.3.

1.3 X-ray absorption spectroscopy (XAS)

X-Ray Absorption Spectroscopy (XAS) is a technique that measures the probability that an x-ray photon incident upon a sample will be absorbed, as a function of the photon energy. Thus, a XAS experiment provides the absorption coefficient $\mu(E)$

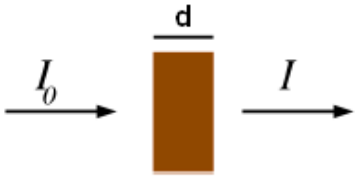

Figure 1.5: Basic geometry of an x-ray absorption experiment through a slab of thickness d. Adapted from [16].

for a given sample, which can be linked to the x-ray intensity attenuation through Lambert-Beer's law, which states, in the geometry of Figure 1.5:

$$I_f = I_0 e^{-\mu(E)d} \tag{1.7}$$

where I_0 and I_f are the initial and final x-ray intensity and d is the sample thickness (or, more precisely, the distance the photon covers inside the sample).

There are some features of $\mu(E)$ that are common to every material:

1. It decreases with increasing energy, approximately following the equation:

$$\mu(E) = \frac{\rho Z^4}{AE^3} \tag{1.8}$$

where ρ is the mass density, Z the atomic number, A the mass number and E the energy. This means that x-rays become more penetrating as energy increase and this is just a result of the well-known absorption of radiation by atoms [17].

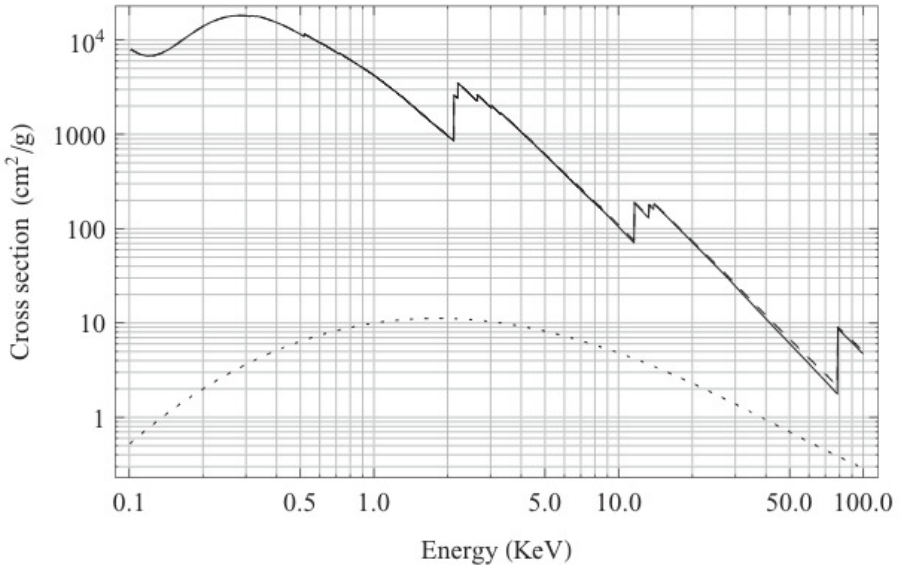

Figure 1.6: Absorption cross section of Platinum. The total cross section in this range of energy consists in the sum of coherent scattering and photoelectric effect. The M, L and K edges are easily noticed. Also, the coherent scattering contribution is showed (dotted line) [18].

2. It presents discontinuities, known as absorption edges (see Figure 1.6), at energies specific for every element. These occur exactly when the photon reaches enough energy to promote an electron from a deep core level above the Fermi threshold. The unique position of this edges gives to the XAS technique its typical element-selectivity.

3. For atoms in the gas phase the absorption coefficient has sharp discontinuity at the edge energy and after that, a smooth profile (Figure 1.7a). In case of solids or molecules, instead, if the experiment is conducted with sufficient energy resolution, $\mu(E)$ shows an oscillatory fine structure both above and below the energy of the edge (Figure 1.7b). This feature originates from the photoelectron, whose wave function scatters from the atoms around the absorbing one, creating interferences between outgoing and scattered parts of the photoelectron wavefunction itself. Therefore the oscillations are due to the fact that when the photon energy increases, so does the kinetic energy of the photoelectron and its associated wavelength decreases; maxima and minima correspond to low or high probability for the electron to scatter back from neighboring atoms and

fall back in the original position. For this reason the fine structure of $\mu(E)$ contains many valuable structural informations like inter-atomic distances and coordination number.

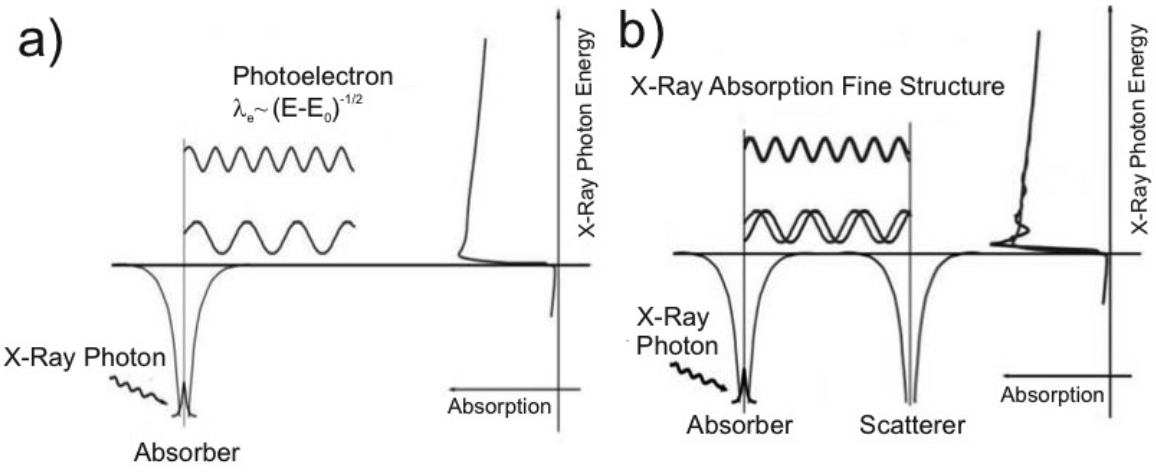

Figure 1.7: Photoelectron wavefunction and absorption profile in case of a single atom (a) and in case of two atoms, one creating the photoelectron and the second one scattering it (b). In this case interference is present and a fine structure rises. Adapted from [16].

All techniques where this fine structure is evidenced are known as XAFS (X-Ray Absorption Fine Structure [16, 19]). XAFS can be divided into two regions, namely the X-Ray Absorption Near Edge Structure (XANES) that comprehend pre-edge features as well and the Extended X-Ray Absorption Fine Structure (EXAFS). In Figure 1.8[20] it is possible to see an example of XAFS spectrum on K edge of Molybdenum, with the different regions highlighted. In the XANES region transitions may occur to unfilled bound states, nearly-bound states (resonances), or continuum states of the appropriate symmetry. Well above the absorption edge, instead (EXAFS region), transitions only occur to continuum states. However, "it has become clear in recent years that there is no fundamental distinction between the physics of these two processes; the distinction is only one of complexity of the spectra"[21]. In fact, in both cases when a transition to continuum states happens, the photoelectron is free to propagate into the material as a wave whose wavelength λ can be calculated via De Broglie's relation and eq.1.3:

$$\lambda_e = \frac{2\pi}{k} = \frac{h}{m_e v} = \frac{h}{\sqrt{2m_e(h\nu - E_{bind})}} \tag{1.9}$$

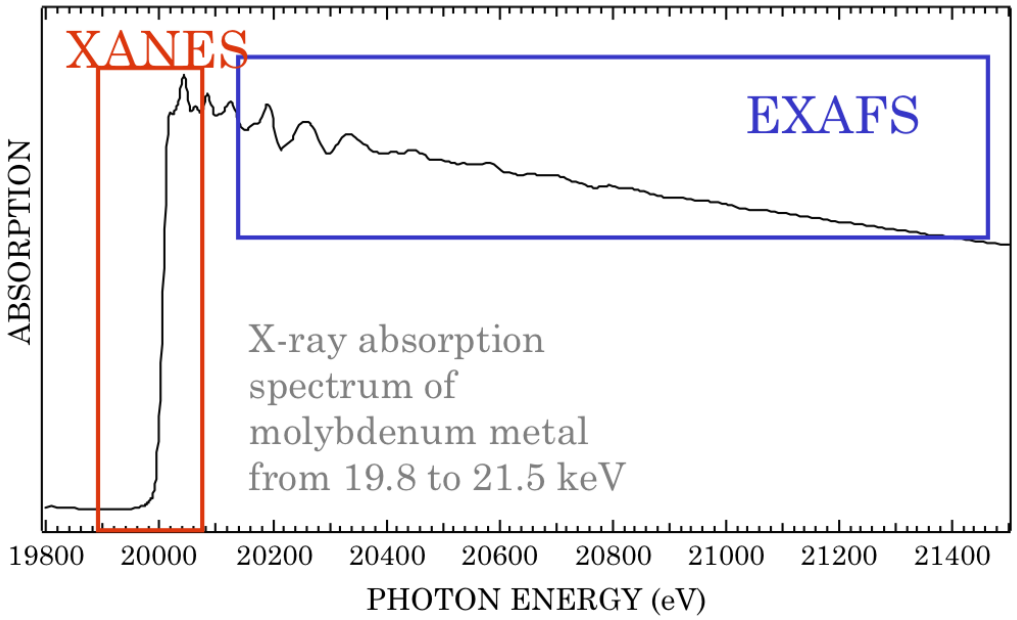

Figure 1.8: X-ray absorption spectroscopy on K edge of Molybdenum metal, with XANES and EXAFS regions evidenced[20].

The difference resides in the fact that in the EXAFS region $h\nu - E_{bind}$ is big and thus the wavelength is small and comparable to inter-atomic distances. For this reason the phenomenon can be explained as a single scattering one (Figure 1.9) and it can be treated in the framework of the well-known theory of diffraction. This also means that the technique will give informations about the spatial arrangement of the atom of interest and not about its electronic structure. In the XANES region, instead, photon energies become small and they rapidly increase above inter-atomic distances (typically, when the photon has an energy of 50 eV higher than the edge, the electron has $\lambda \approx 1.72$ Å, at 20 eV it already has $\lambda \approx 2.7$ Å etc), allowing multiple-scattering processes to become important. Furthermore, XANES involves pre-edge and edge regions, which are transitions to bound and quasi-bound states and thus it is rather sensitive to details in the electronic structure and chemical state of the sample. In the next section the two techniques will be described in more detail.

1.3.1 EXAFS

The EXAFS region covers the high-energy continuum above the ionization threshold and it is characterized by an oscillatory pattern on the XAS spectra, which can

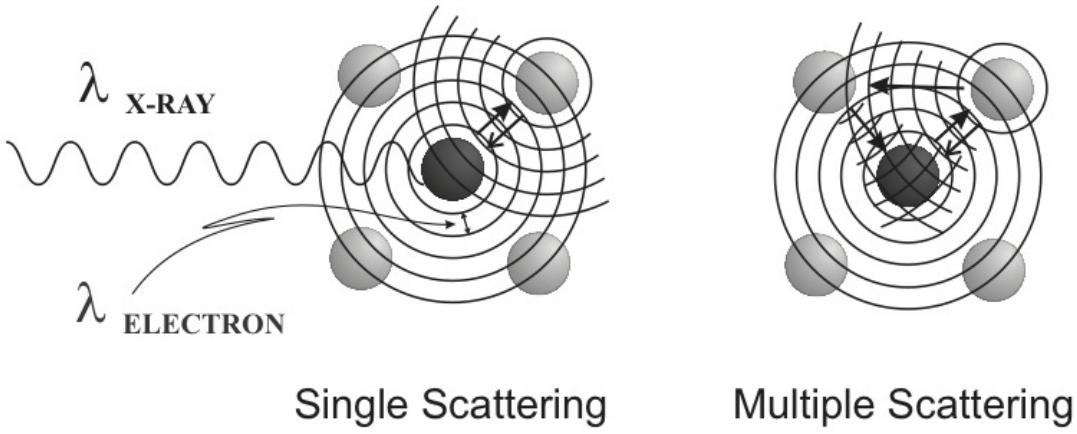

Figure 1.9: Schematic picture of single scattering regime (EXAFS) and multiple scattering regime (XANES)[22].

be related to a single scattering event of the outgoing electron wavefunction with a neighboring atom. For EXAFS interpretation, we are interested in oscillations well above the absorption edge and to study them it is convenient to define the EXAFS fine-structure function $\chi(E)$ as:

$$\chi(E) = \frac{\mu(E) - \mu_0(E)}{\Delta\mu_0(E)} \tag{1.10}$$

where $\mu_0(E)$ corresponds to a smooth background function representing the absorption of an isolated atom and $\Delta\mu_0(E)$ being the normalization factor corresponding to the absorption edge jump (a step-function-like sudden increase of the net absorption coefficient at the ionization threshold). This definition means that the total absorption coefficient $\mu(E)$ is expressed as the sum of the isolated atom absorption $\mu_0(E)$ plus a correction factor that modulates it. At this point, it is convenient to switch from energy space to photoelectron wavevector space ($k-space$), in order to describe the interference effects in electron scattering. This is straightforward using eq.1.9. Thus, many derivations are available in literature ([23, 1] and a simpler one in [16]) to lead to the well-known empirical equation to describe EXAFS:

$$\chi(k) = \sum_i S_0^2 N_i \frac{|f_i(k)|}{kR_i^2} \sin(2kR_i + \delta_c + \phi) \exp(-2\sigma_i^2 k^2) \exp(-\frac{2R_i}{\lambda(k)}) \tag{1.11}$$

Here, $|f_i(k)|$ and ϕ are the modulus and phase of the complex electron scattering amplitude for every atom, δ_c is the partial wave phase-shift of the central absorbing

atom, S^2 is a constant reductive factor due to loss of coherence and N is the number of neighboring atoms at distance R. Since many different kind of atoms can be close to the central one, the summation must be taken over all the groups of neighboring atoms, which are known as coordination shells. Each one of these has a well defined inter-atomic distance with the absorber atom and a well-defined scattering function (the fact that the scattering function depends on the Z of the neighboring atom makes EXAFS sensitive to this atomic specie). For the complete description of the physical process other important parameters are included into this equation: the term $\exp(-2\sigma^2 k^2)$, where $2\sigma^2$ is the Debye-Waller's factor (in harmonic approximation, it is the full width at half maximum of the gaussian distribution of interatomic distances) takes into account thermal disorder, while the $\exp(-2R/\lambda(k))$ uses the mean free path function $\lambda(k)$ to dampen the signal as a consequence of core-hole lifetime (photoelectron recombination) and photoelectron inelastic scattering. The most important features of EXAFS can be understood from this equation: the $\lambda(k)$ and R^{-2} terms show why it is a local probe of the structure surrounding the absorber atom, not able to see much farther than 5 Å from it; the sinusoidal function shows contributions of different frequencies for different inter-atomic distances, i.e. every coordination shell introduces a new frequency. This explains why the data analysis of EXAFS is done with Fourier transform-based techniques [24] that are in general able to extract useful structural informations (mainly N, R and σ^2) from the spectra. Finally, it is important to underline the approximation under which equation 1.11 is derived: the potential energy of the photoelectron through the solid is approximated as that of spherically symmetric atoms with a constant region between them (the "muffin-tin approximation"), only a single electron is directly excited, which interacts with the electron gas in the solid; only back-scattering (elastic) from each neighboring atom is included, i.e. multiple scattering is neglected (nevertheless, multiple scattering effects can be important in the EXAFS region as well and theoretical approaches are available to treat these effects [25, 26]).

1.3.2 XANES

The XANES part of the XAS spectrum is usually about 10-50 eV above the edge, even though this is somehow arbitrary. In this region, the signal is usually much higher than EXAFS signal, which means that the experiment can be performed on samples that are either more diluted or richer of defects. On the other hand, we are in the low k limit and EXAFS equation is not valid because the single scattering approximation does not hold anymore. This complicates a lot XANES interpretation because, although it is possible to write a full hamiltonian to describe the process, it is very difficult to solve the related equations and integrals coming form the Fermi golden rule, since the initial and final state wavefunctions are not usually known in details for real systems. For this reason, approximations must be made and implemented in numerical calculations. If one is able to do so in a satisfactory manner, XANES interpretation in useful because it contains both electronic and structural information about the system under study.

The first absorption features which appear when energy exceeds the Fermi level (about the first 5-10 eV above it) namely the pre-edge region have a physical origin, which is different for different classes of materials: bound valence states, core excitons in ionic crystals, unoccupied local electronic states in metals and insulators, etc. Above the Fermi energy and just below the ionization threshold one finds the so-called "white line", which is a strong absorption peak. The name comes from experiments in the past, when these peaks were "white" because they were often saturating detectors. The physical origin of such a peak is the transition to empty states which are spatially localized close to the nucleus, hence giving a high overlap between initial and final state wave functions. Finally, the region after the white line is governed by multiple scattering events, determined by the geometrical arrangements of the atoms in a local cluster around the x-ray absorbing atom. Indeed, XANES can be described qualitatively in terms of:

- coordination chemistry of the absorber atom neighborhood.
- molecular orbital structure (crystal field splitting, d-d interaction, p-d hybridization etc.).

- band structure (density of states).
- multiple scattering of the photoelectron.

In addition, since XANES transitions are subject to dipole-quadrupole selection rules and since these rules look different depending on the local symmetry around the absorbing atom, information about the local geometrical arrangement can be obtained when forbidden transitions show up in XANES spectra.

For the reasons listed above, XANES interpretation is based mainly on theoretical calculation. Fortunately, nowadays we are living a great improvement in the computational capabilities, which allow faster calculations, and in the development of more accurate theoretical approaches. The methods used to calculate the ground and final state wave functions as well as the photo-induced electronic transitions are various [27]. Each of them has its strengths to describe certain aspects and properties of the XANES spectrum, but this will not be treated in this thesis.

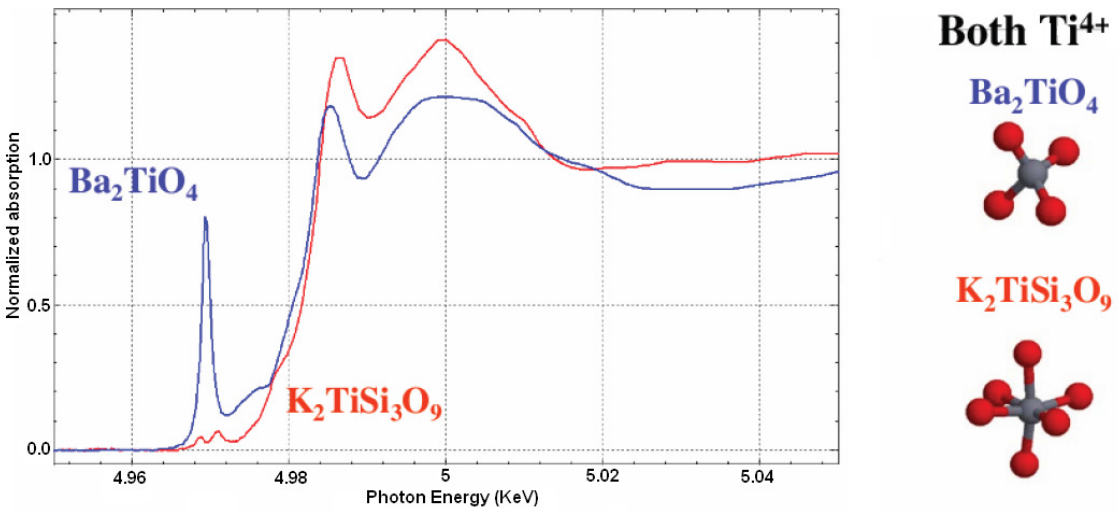

Figure 1.10: XANES spectra of titanium K edge, showing strong dependence on the atomic coordination. On the right, coordination of Ti[20].

In order to show some examples of how a XANES spectrum can provide useful information, in the following some examples are shown about the K edge of titanium, where it is evident how it is influenced by the valence state, ligand type and coordination environment of the absorber atom. A first example is given in Figure 1.10.

There, two spectra are shown for Ba_2TiO_4, a rare example of tetrahedral coordination for Ti, and $K_2TiSi_3O_9$, a zeolitic structure with octahedral coordination. In both cases the oxidation state of Ti is 4+, but they differ for the coordination of the central titanium atom. Differences are really strong and show up both in the pre-edge feature and in the edge position and intensity. The biggest change is noted in the pre-edge peak which is very strong in case of tetrahedral coordination and completely disappears for the octahedral one. This is due to the fact that a different symmetry

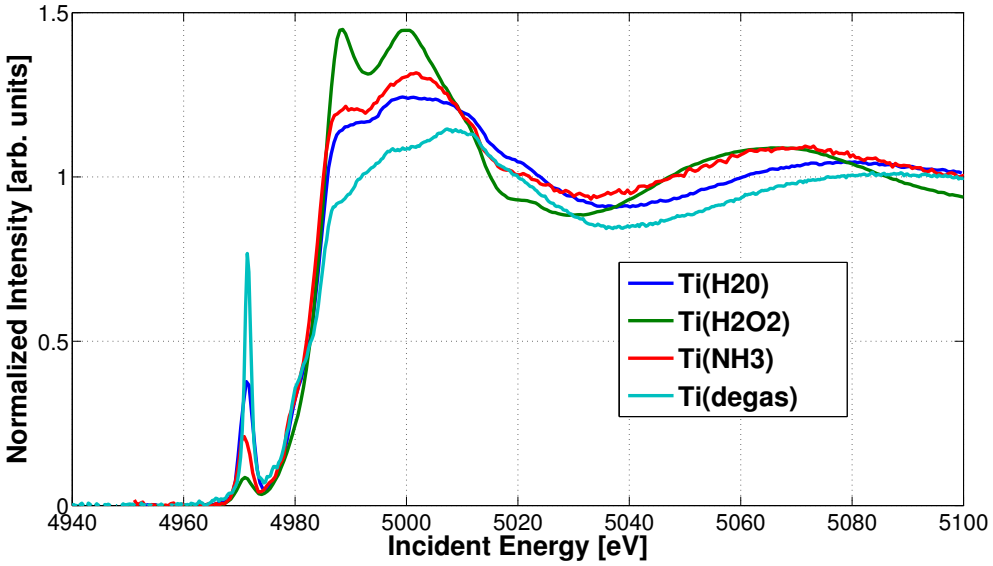

Figure 1.11: XANES spectra of TS-1. Titanium K edge shows strong dependence on the coordination sphere of titanium. Data taken from authors of [28].

of the central atom can lead to different hybridizations of the outer orbitals, leading to different relaxation of the selection rules. In particular, octahedral coordination is centro-symmetric (O_h symmetry): no p-d orbitals mixing is allowed and only weak quadrupolar transitions can possibly show in the pre-edge (anyway, in case of metal complexes, for example, 3d levels suffer crystal field splitting into t_{2g} and e_g levels, so small pre-edge transitions to these levels are present, even if they are rather weak). When the octahedral coordination starts to relax, resulting in a distorted structure, the p-d mixing also becomes possible and dipolar transitions in the pre-edge have an increasing intensity. Finally, in case of tetrahedral coordination the orbitals are completely mixed. In fact, in this case the T_d symmetry leads to possible $1s-3d$ tran-

sitions below the Fermi energy, which for titanium are particularly intense because of its many empty d orbitals. Another similar example is shown in Figure 1.11, where the edge is again the K of titanium. Although this time, the spectra are taken from a zeo-type material called TS-1[28], which was measured in an environment of water, ammonia, oxygenated water and de-gassed. Theoretical calculations show that the coordination sphere of titanium, which is tetrahedral in the de-gassed system, gets more and more distorted by the presence of water, ammonia and oxygenated water, respectively. Again, differences are noted both in the edge features and in the smoothening of the pre-edge peak.

Finally, XANES can be used to distinguish the oxidation state of a given transition metal in a molecule. Titanium, for example, is usually found in the ionized state of Ti(III) or Ti(IV). As an example, Figure 1.12 shows titanium bond to chlorine in fluorhydrate systems in both the oxidation states.

1.4 X-ray emission spectroscopy (XES)

X-ray emission is a second-order process that follows the creation of a core hole. Indeed, instead of recording a spectrum of the absorption coefficient as a function of a variable incident energy, like in XAS, XES records the emission of fluorescence of a sample after its excitation with, e.g., an high energy incident photon. This means that the sample is first excited with x-rays of proper fixed energy (above an edge of interest), creating a core hole. After that the system will spontaneously decay in a lower energy configuration via transition of an electron from higher shells to the core hole, which will be filled. The energy that this secondary electron loses must be conserved and this happens either by the emission of an electron (Auger emission) or by the emission of an x-ray photon with energy equal to the difference between initial and final state (Figure 1.13).

XES deals with the detection of such x-ray photons, i.e. a spectrum of the emission of the sample is recorded while scanning through a certain energy range. Obviously, since these photons come from the recombination of a filled shell electron towards a core hole, the output signal will reflect the valence electron of the sample or its

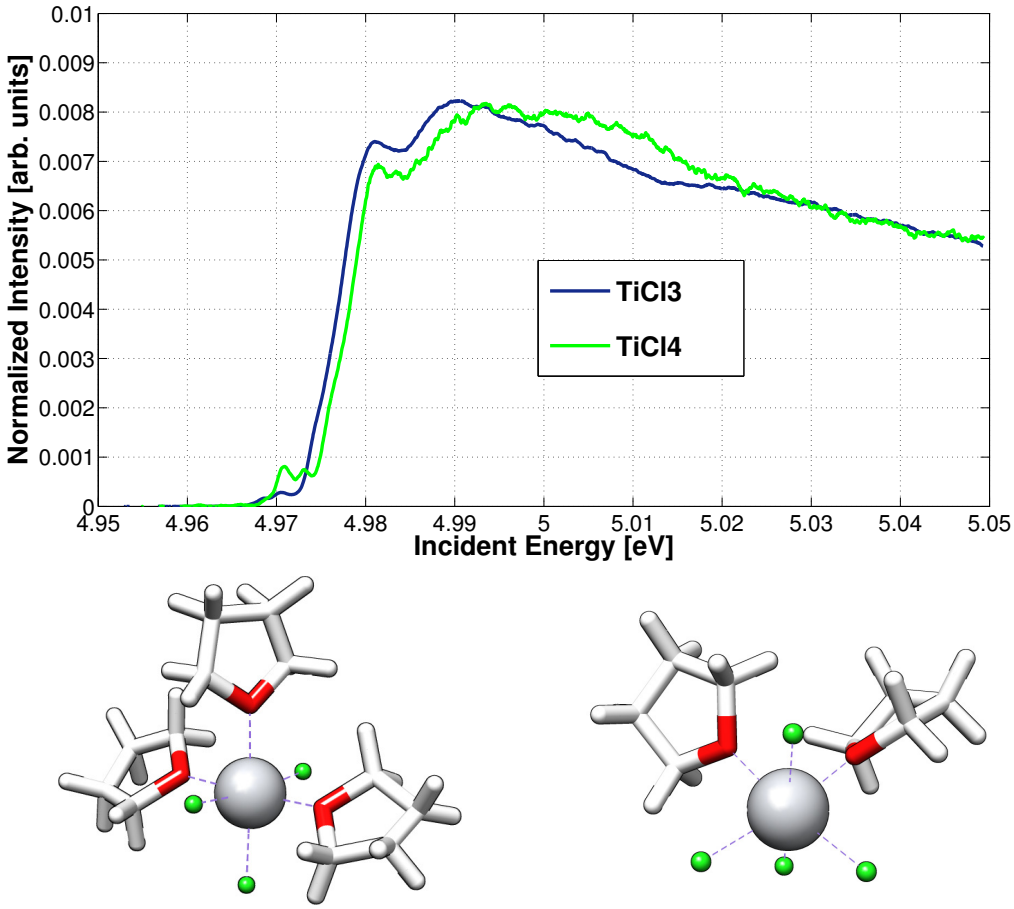

Figure 1.12: Top: $TiCl_3$ and $TiCl_4$ XANES spectra show how $Ti(III)$ and $Ti(IV)$ give rise to differences in their spectral features. Bottom: Actual shape of the whole molecule ($TiCl_3$ on the left and $TiCl_4$ on the right), with a big central titanium atom, green smaller balls as chlorine atoms and fluorhydrate groups to complete the geometry[29].

occupied states below the Fermi energy. For this reason the XES spectrum lays on the other side, with respect to the Fermi energy, of the XAS absorption spectrum (Figure 1.15), whose signal comes from the unoccupied states above the Fermi energy. When detecting a fluorescence signal, it is not present only the emission line of interest; instead, many lines can give a contribution, each one of them with a different relative probability, which depends on the element considered. The totality of existing lines is showed in Figure 1.14.

When all emission lines are detected, the measure is referred to as total fluorescence yield detection, and it can easily be performed with a common photodiode, which does not have energy resolution. However, the energy resolution can be given

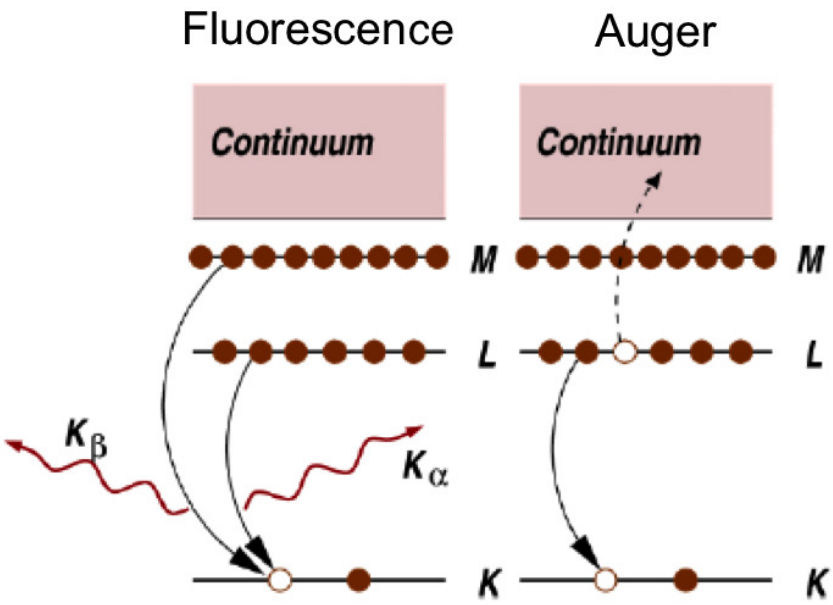

Figure 1.13: As a consequence of the creation of a core hole, a fluorescence photon can be emitted, here with energy of K_α or K_β emission line (left), or an Auger electron can be created (right)[16].

either by a solid state detector (typically, a Germanium detector) or by a spectrometer that selects only the required energy by means of Bragg reflections on its mirrors (in this case the energy resolution can be strongly improved, as will be described in the next chapter). This way it is possible to detect the different emission lines singularly and thus to observe precisely the intensity and position of the emission peaks. The analysis of emission peaks is much easier than XANES spectra because of the simpler spectral shape; they are usually simply fitted with a Voigt function (e.g. the convolution between a Lorentzian and a Gaussian function) to find precisely intensities and positions and describe the occupied states of the system. Examples of use of XES K_α and K_β main fluorescence lines to infer useful information about, e.g., the chemical state of a sample are given in ref.[2].

1.5 XAFS detection techniques

The most direct way to measure a XAFS spectrum is in transmission mode, since this comes straight from its definition. This means that the X-ray is incident on the sample and the detector, which is located right after it, collects all the X-rays that

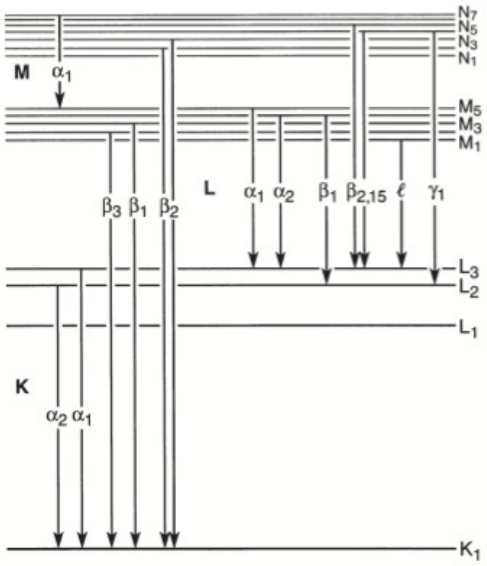

Figure 1.14: Emission lines scheme [12]. Only dipole-allowed transitions are showed.

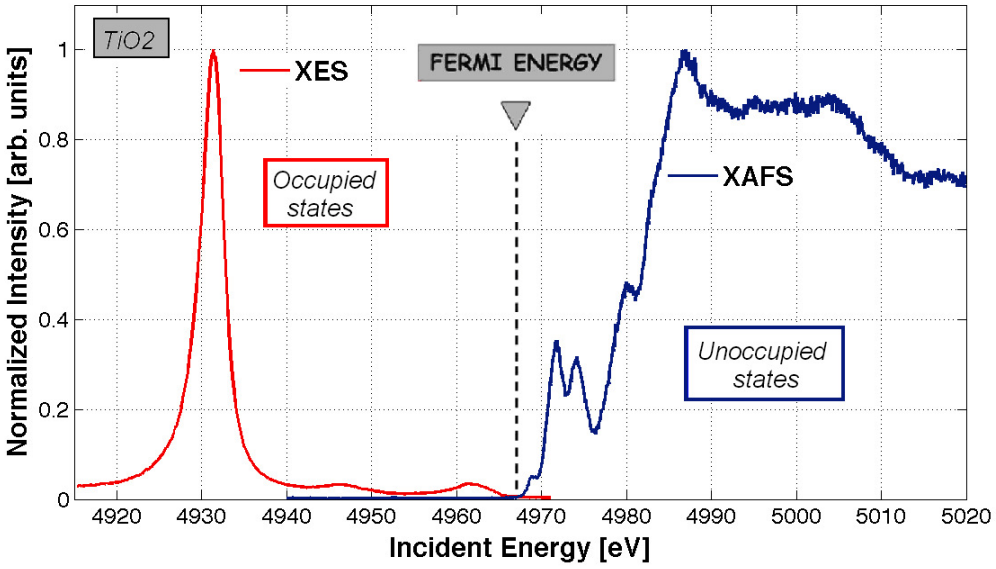

Figure 1.15: XES and XAS spectra of TiO_2 with respect to the Fermi Energy. XES reflects the occupied states below this energy and one can see 3p-1s and valence states-1s transitions here. XAS, instead, reflects the empty states above it, i.e. transitions from 1s to conduction band states coming from 3d and 4p levels of titanium mixed with oxygen orbitals.

are not absorbed. The measured quantity is then exactly I_f from Lambert-Beer's law (eq.1.5) from which the absorption coefficient can be directly calculated as:

$$\mu(E) = \frac{1}{y}\ln(\frac{I_0}{I_f}) = \frac{\sin\theta}{d}\ln(\frac{I_0}{I_f}) \tag{1.12}$$

A simple picture of XAFS transmission detection is shown below (Figure 1.16a).

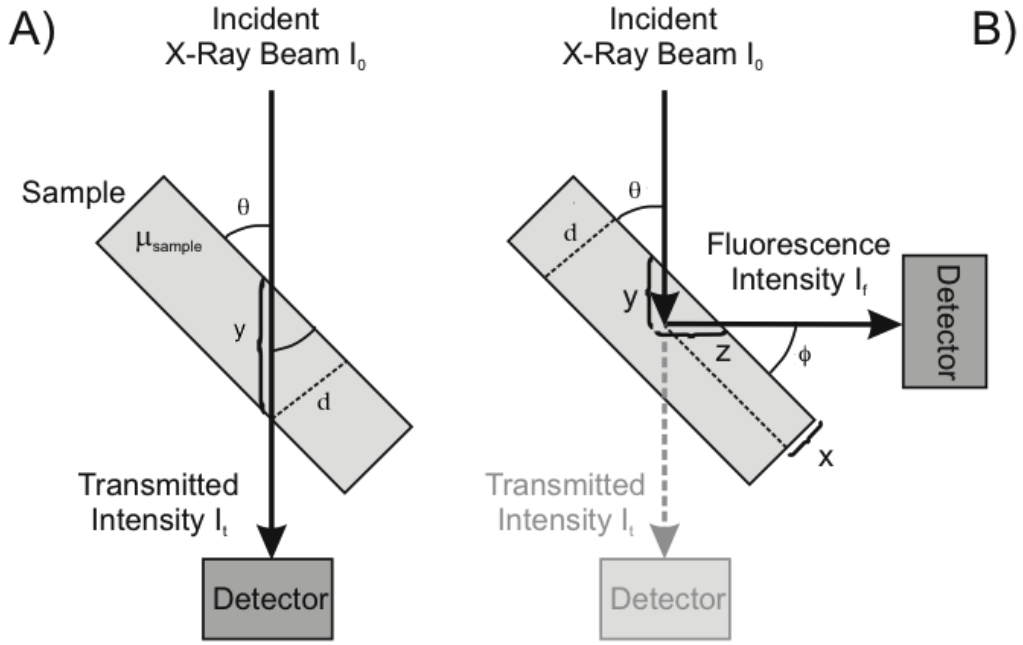

Figure 1.16: A) Scheme of the setup to measure XAS in transmission. B) Scheme for the same measurement performed in fluorescence mode[30].

Transmission measurements are most commonly implemented in XAFS experiments because of their relative simplicity. To perform the experiment one needs an accordable source of X-rays (which are normally synchrotron sources), whose wavelength is usually selected via a monochromator. This is also used to scan the photon energy through the range of interest, while the incident photon flux I_0 and the transmitted one I_f are measured simultaneously (e.g. with ionization chambers or other similar detectors). This way an entire spectrum can be recorded.
However, this technique has some strong limitations to its use. Mainly, both the absorption coefficient (and thus the concentration) and the sample thickness do not have to be too high, otherwise the term $\mu(E)d$ in the exponent of eq.1.5 becomes too big and the transmitted intensity goes to zero, i.e. no signal is detected. This limits the use of transmission detection to thin samples (where "thin" depends on the concentration, i.e. it means microns for concentrated samples, but it can reach the millimeters range for diluted ones). Also, it should be noted that, in principle, $\mu(E) = \mu_{abs}(E) + \mu_{else}(E)$ i.e. it refers to the total absorption coefficient of the sam-

ple, which includes not only the absorber atom (the selected atom whose absorption one wants to measure) but all other atoms as well, which may come for example from the solvent molecule or from other atoms present in a crystal lattice in which the absorber is embedded. For this reason it is very important for the sample to be homogeneous, so that the contribution from other atoms is always the same. This way, once one knows where this further absorption come from and the relative concentration of the components, it is easily possible to cancel it from the spectrum to extract $\mu_{abs}(E)$.

In some cases, however, it can be advantageous to measure $\mu(E)$ indirectly by monitoring a process that is proportional to the absorption coefficient. X-ray fluorescence is one of these methods, together with Auger electron emission, though this last one is not treated in this thesis. The typical setup of a fluorescence measurement is shown in Figure 1.16b. In a fluorescence XAFS measurement, the X-ray energy is usually scanned through an edge of interest, while the fluorescence emitted is simultaneously detected at the energy typical of an emission line, e.g. K_α or K_β. This means that the XES signal will be proportional to the absorption coefficient, which can be reconstructed from it. To fully understand this, it is useful to go through the equations that govern the whole process. The probability that a photon incident on the sample is absorbed and as a consequence a fluorescence photon is emitted and collected by the detector is a joint probability, i.e. the product, of many independent terms[31]:

- $$\exp(-\frac{\mu(E)x}{\sin\theta}), \tag{1.13}$$

  the probability that the photon, incident with angle θ on the sample, penetrates for a distance x (Note again that $\mu(E)$ is the total absorption coefficient of the sample and not only the absorber one. These two quantities are related by $\mu(E) = \mu_{abs}(E) + \mu_{else}(E)$).

- $$\frac{\mu_{abs}(E)\mathrm{d}x}{\sin\theta}, \tag{1.14}$$

the probability that this photon is absorbed by the absorber element in an infinitesimal layer of thickness dx.

- ϵ, the fluorescence yield, e.g. the probability to have a radiative process (an emitted photon with energy E_f) instead of a non-radiative (Auger) one.

- $$\frac{\Omega}{4\pi}\exp(-\frac{\mu(E_f)x}{\sin\phi}), \tag{1.15}$$
  the probability that the emitted photon travels through the sample without being re-absorbed and reaches the detector subtended by a solid angle Ω.

- All this have to be integrated over the whole length of the sample, d.

Finally, these terms give:

$$\frac{\Omega}{4\pi}\epsilon\frac{\mu_{abs}(E)}{\sin\theta}\int_0^d e^{(-\frac{\mu(E)x}{\sin\theta})}e^{(-\frac{\mu(E_f)x}{\sin\phi})}\mathrm{d}x = \frac{\Omega}{4\pi}\epsilon\frac{\mu_{abs}(E)}{\sin\theta}\frac{1-e^{-\left[d(\frac{\mu(E)}{\sin\theta}+\frac{\mu(E_f)}{\sin\phi})\right]}}{\frac{\mu(E)}{\sin\theta}+\frac{\mu(E_f)}{\sin\phi}} \tag{1.16}$$

which is proportional to the absorption coefficient of the absorber element in the sample, i.e. the goal of the measurement. In chapter 3 limitations of fluorescence detection will be shown, since one could observe that $\mu_{abs}(E)$ appears also in the denominator and in the exponential function, determining a distortion effect in the spectrum known as self-absorption. Anyway these limitations can be often overcome and this will be shown in the following.

Further important considerations regarding good fluorescence XAFS measurements can be made about solid angle and energy resolution. The need for solid angle is easy to understand. The fluorescence is emitted isotropically and one would like to collect as much of the available signal as possible. The scatter is actually not emitted isotropically because the x-rays from a synchrotron are mainly polarized in the plane of the synchrotron (see chapter 2). This means that elastic scatter is greatly suppressed at 90 ° to the incident beam, in the horizontal plane. Therefore, fluorescence detectors are normally placed at a convenient angle to the incident beam, taking care of these considerations. Energy discrimination is important because it can potentially allow to completely eliminate the scatter peak and other fluorescence lines and collect only the intensity of the fluorescence lines of interest. This would

greatly suppress the background intensity and increase the signal-to-noise level. Energy discrimination can be accomplished either physically, by filtering out unwanted emission before it gets to the detector, or electronically after it is detected. The first option is the most implemented one and in chapter 2 a solution that selects the required emission line using a Rowland geometry spectrometer is described, together with the high resolution results that can be obtained with it. In such a case the technique is referred to as High Energy Resolution Fluorescence Detected (HERFD) XAS. This has the great advantage that one can choose the detector freely, since the energy is selected by means of Bragg optics (which also ensure a great reduction of unwanted background radiation). Besides, this technique offers a very high signal-to-background ratio because its energy resolution is of the order of the core hole lifetime broadening, which is now smaller than for conventional XAS. For these reason, this proved to be a good instrument to reveal fine structures in XAS, as showed in many reviews on the topic[32, 33].

1.6 RIXS

Resonant Inelastic X-ray Scattering (RIXS), also called Resonant X-ray Emission Spectroscopy (RXES) is an experimental technique whose application is exploited more and more to study a wide range of materials such as transition metal compounds [34, 35] or rare-earth systems [3], semiconductors and insulators[36], oxides [37] and materials of current interest such as high temperature superconductors[38] or catalysts [39]; also, it allows to study elementary excitations in this whole range of materials, as described in ref.[40, 41].

RIXS is based on a second-order process: first an electron is excited creating a core hole with a given lifetime broadening (which is the parameter that normally determines the width of XAS spectra); after that, the core hole is filled via a radiative transition, which is what usually happens in standard XES measurements. Combining the two events we obtain RIXS, i.e. a process during which the fluorescence energy emitted after the filling of the core hole becomes a function of the incident energy. Therefore, a RIXS plane is obtained when the incident energy is tuned across

an absorption edge, the electronic states are resonantly excited and decay, and the fluorescence is detected resolving its energy (e.g. in a wavelength dispersive spectrometer, as showed in chapter 2).

The second order process transition ratio can be described via the Kramers-Heisenberg relation[42, 15]:

$$F(\Omega,\omega) = \sum_f |\sum_i \frac{< f|T_2|i >< i|T_1|g >}{E_g - E_i + \Omega - i\Gamma_i/2}|^2 \times \frac{\Gamma_f/2\pi}{(E_g - E_f + \Omega - \omega)^2 + \Gamma_f^2/4}. \quad (1.17)$$

Here, Ω and ω indicates respectively the incident and emitted photon energies while

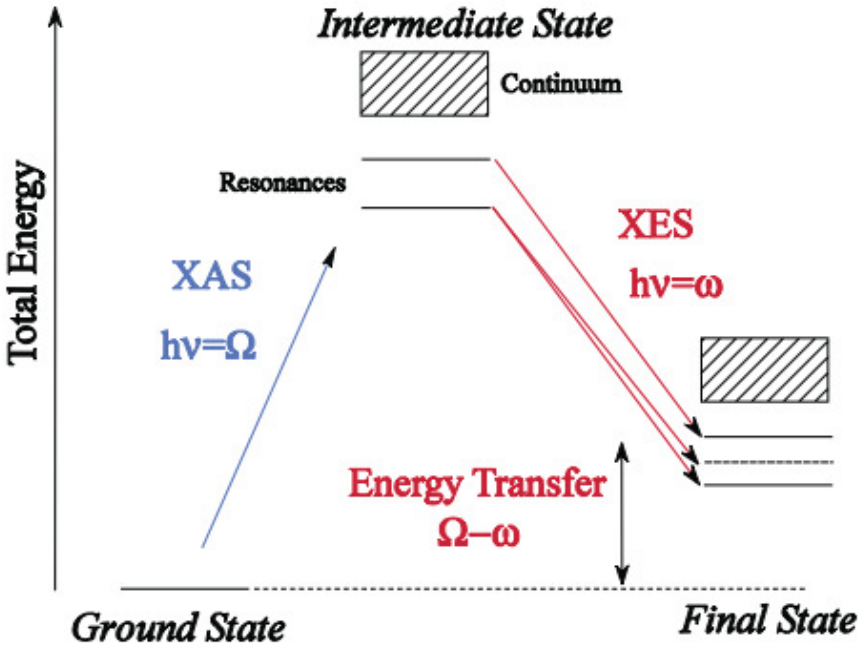

Figure 1.17: Scheme model for RIXS process. Energy levels are shown as a function of the total energy of the system[34].

$|g>$, $|i>$, $|f>$ indicates the ground, intermediate and final state wavefunctions with correspondent energies E_g, E_i and E_f. The intermediate state $|i>$ is reached via a transition operator T_1 from the ground state $|g>$ and the final state is reached via the dipole operator T_2, from $2p$ or $3p$ to $1s$ transition. The intermediate states $|i>$ in RXES spectroscopy are the final states in conventional K-edge absorption spectroscopy. Γ_i and Γ_f take into account, respectively, the intermediate and final state lifetime broadening.

A model scheme for RIXS is showed in Figure 1.17, where the Energy Transfer, i.e. the difference between the incident and emitted energy, is evidenced. This is useful in order to relate the energies of all intermediate and final states to the same reference energy, i.e. the ground state energy E_g. The RIXS process, as described now and depicted in Figure 1.17, appears to be a two-step process separated into a resonant excitation to an intermediate state and a subsequent decay into a final state. However, a careful look at eq.1.17 tells that this is not entirely correct. In fact the summation over all intermediate states should be performed before the square, so that interference effects are possible between intermediate states. This means that the complete RIXS process must contain all scattering paths with the same final but different intermediate states, which can therefore interfere with each other. Such effects are often important in broad band solids, but when electron-electron interactions are less important they can be neglected to rewrite eq.1.17 in a more straightforward form:

$$F(\Omega,\omega) = \sum_f \sum_i \frac{< f|T_2|i >^2 < i|T_1|g >^2}{(E_g - E_i + \Omega)^2 + \Gamma_i^2/4} \times \frac{\Gamma_f/2\pi}{(E_g - E_f + \Omega - \omega)^2 + \Gamma_f^2/4}. \quad (1.18)$$

Equation 1.18 simply weights the emission by the absorption matrix elements and broadens the spectra by Γ_i along the incident energy Ω and by Γ_f along the energy transfer $\Omega - \omega$. In order to understand the role played by these broadenings, it is useful to show a schematic RIXS plane for the energy scheme of Figure 1.17. In a RIXS plane like this (Figure 1.18a), the incident energy is plotted versus energy transfer and the intensity is shown as a contour plot.

Here, the final state broadening appears along the energy transfer direction, while the broader intermediate state broadening stretches along the incident energy one. This has some important consequences when the experimenter wants to recover line plots informations from the RIXS map. Indeed, a XAS spectrum can be extracted from the RIXS map, since it is the integral of the RIXS signal on all the deexcitation channels, i.e. the final state energies. In this case, however, the spectrum does not have features broadened by the core-hole lifetime and more details can be resolved with respect to a standard XAS spectrum, as depicted in Figure 1.18b. It should be noted that other factors influence the shape of the contour plot in a RIXS map,

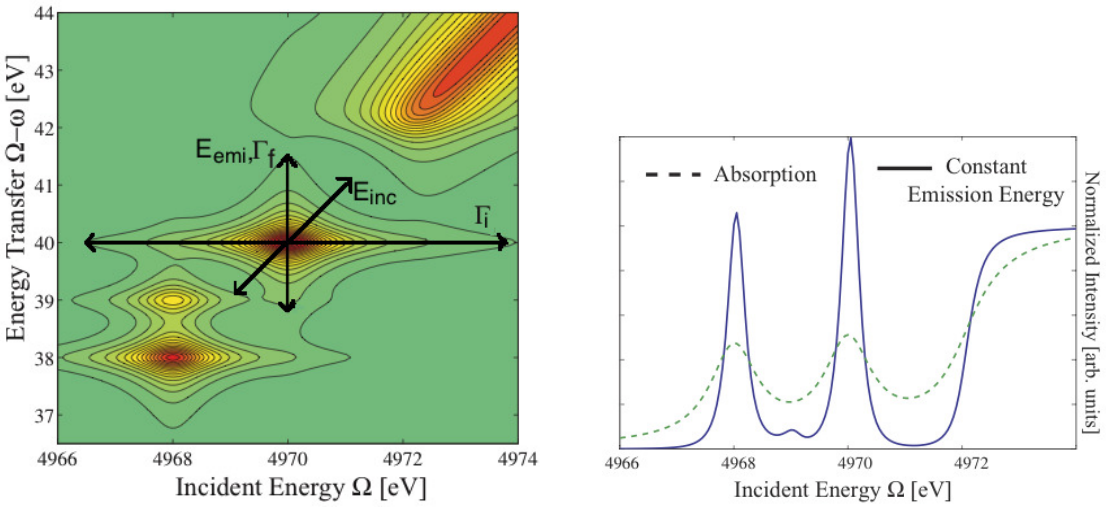

Figure 1.18: Left: RIXS map of the energy scheme of Figure 1.17, where the intermediate and final state broadening are shown, together with the incident and emission energy contributions. Right: map integrated over all possible energy transfers. It represents a XAFS spectrum compared with an actual XAS spectrum. The enhancement in resolution is significant. Adapted from [34].

namely the incident energy resolution (usually determined by the resolving power of a monochromator) and the emitted energy resolution (given by, e.g., a spectrometer). Their contribution is shown in Figure 1.18a.

As an example of a real RIXS measurements Figure 1.19 is reported below. It shows an $1s - 3d$ map of TiO_2 in two different crystalline phases, namely anatase and rutile.

1.7 Conclusions

This chapter was dedicated to treat the basics of matter interaction with radiation, particularly for its short wavelength regions. After that, a number of spectroscopic techniques which exploit x-rays was described in detail, together with the informations regarding the electronic structure of an atom, its chemical behavior and the geometry in its neighborhood which can be extracted from them. Mainly, x-ray absorption spectroscopy (XAS) techniques were described in the XANES and EXAFS energy region, with some detail for High Energy Resolution Fluorescence Detected XAS which has been applied to all the experiments in this thesis. Furthermore, X-ray Emission Spectroscopy (XES) was treated as a complementary technique and finally

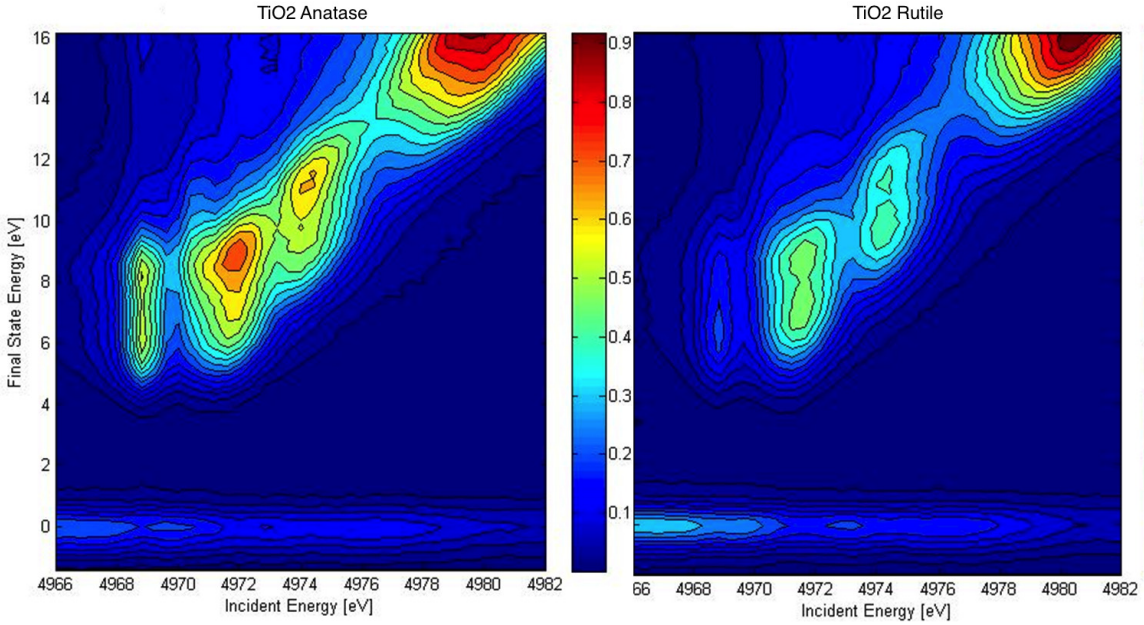

Figure 1.19: RIXS $1s - 3d$ of Anatase (left) and Rutile (right) phases of titanium dioxide. Data taken at ID26 and unpublished.

Resonant Inelastic X-ray Scattering (RIXS, or Resonant X-ray Emission Spectroscopy RXES) was discussed as a complete technique that connects and completes XAS and XES in a unique tool able to represent both absorption and emission features on the same diagram, with high resolution.

Chapter 2

Experimental techniques

This chapter describes the basic principles that govern the functioning of a synchrotron, from the physics of the radiation emission to more technical and engineering aspects. It gives an idea of the the range of energy, power, pulse length (spatial and temporal) and other properties which can be achieved in such a structure. In the second part, beamline ID26 of ESRF is described; it is addressed to x-ray spectroscopy and thanks to its ability to tune the incident energy of x-rays with a monochromator and the emitted energy from a sample with a spectrometer is the ideal place to exploit both XAS and XES techniques (and therefore RIXS too).

2.1 Synchrotron radiation

Synchrotron radiation (SR) is the name given to electromagnetic radiation emitted by an accelerated charge within a synchrotron. The first observation of synchrotron radiation took place in 1947 at the General Electric Research Laboratory in New York. In the following years it was realized by the scientific community that this was the most intense and versatile source of X-rays; for this reason storage rings stopped to be dedicated only to high energy nuclear physics experiments and the development of first generation synchrotron facilities began with Tantalus I, where the first spectrum was measured in 1968. However, the design and work conditions of these facilities were not optimized for X-ray experiments, limiting the output of synchrotron radiation. The first facility conceived as a synchrotron radiation source

was in operating mode in 1981; it was the 2GeV SRS (Synchrotron Radiation Source) in UK, followed by many other synchrotron radiation facilities like NSLS, BESSY or LURE. This history has culminated in the 3rd generation synchrotron sources like the European Synchrotron Radiation Facility (ESRF, Figure 2.1), with a factor of 10^{12} times brighter than the early lab based sources.

Figure 2.1: Aerial view of the European Synchrotron Radiation Facility[10].

2.1.1 Emission of radiation from accelerated charges

The emission of radiation from accelerated charges was already well-known before the advent of relativity and quantum mechanics. Indeed, via Maxwell's equation, it is possible to easily derive Larmor's formula as the power emitted from an oscillating dipole with charge equal to electron's charge and acceleration $\vec{a}$. This is expressed by:

$$P = \frac{e^2\vec{a}^2}{6\pi\epsilon_0 c^3}. \tag{2.1}$$

Although eq.2.1 can be valid for an accelerated non-relativistic electron which radiates isotropically in space, it is not valid for a synchrotron, where electrons are accelerated to a speed very close to the speed of light. A relativistic generalization

can be derived using the Lienard-Wiechert fields (these are relativistic solutions of Maxwell's equations with source terms Q and J of a single charged moving particle [43]) and calculating the resulting flux of the Poynting vector, leading to an emitted power:

$$P = \frac{e^2}{6\pi\epsilon_0 c^3}\gamma^6 \left[\dot{\vec{v}}^2 - \frac{(\vec{v}\times\dot{\vec{v}})^2}{c^2}\right] \tag{2.2}$$

which does not show any angular contribution because it is integrated over the whole solid angle. Here, $\gamma = \frac{1}{\sqrt{1-\beta^2}} = \frac{E_0}{m_e c^2}$ (i.e. it is the particle energy in units of its rest energy) and β is the Lorentz factor v/c. Furthermore, the emitted power strongly depends on many parameters that are peculiar of the considered synchrotron, like magnetic fields and radius of curvature. In these devices, in fact, the momentum $\vec{p}$ changes rapidly in direction as the particle rotates, but the change in energy per revolution is small. Also, the direction of acceleration is always perpendicular to the direction of motion. The most important result, valid for a relativistic particle with high energy traveling on a circular orbit of radius R, is equation 2.3 (again this is integrated over the whole solid angle):

$$P = \frac{e^2}{6\pi\epsilon_0 c^3}\gamma^4 |\dot{\vec{v}}|^2 \tag{2.3}$$

which can also be rewritten for the case of a synchrotron, i.e assuming that the curvature on the electron orbit is obtained by means of a perpendicular magnetic field. In this case R can be found setting equal the expression for the Lorentz force and the centripetal force. Hence

$$R = \frac{m_0^2 c^3 \gamma^2}{eEB} \tag{2.4}$$

and

$$P = \frac{e^4}{6\pi\epsilon_0 m_0^4 c^5} E^2 B^2. \tag{2.5}$$

Eq. 2.3 and 2.5 show that the emitted power has a strong dependence on $1/m^4$ (that explains why only electrons (and positrons) could be used to generate synchrotron radiation, thanks to their small rest mass), a dependence on $1/R^2$ and a quadratic dependence on the magnetic field strength. From this equations it is easy to calculate how much energy the electron loses every round trip in the ring:

$$\Delta E = \frac{2\pi R}{v} P = \frac{e^2 v^3 \gamma^4}{3\epsilon_0 c^3 R}. \tag{2.6}$$

For highly relativistic electrons, $v \sim c$ and this can be conveniently rewritten as

$$\Delta E(MeV) = 8.85 \cdot 10^{-2} \frac{[E(GeV)]^4}{R(m)}. \tag{2.7}$$

Also, the lost energy goes as the fourth power of the particle energy, which means that it loses a lot of it every round trip and this lost energy must be restored somehow. In synchrotrons, in particular, this is done via a radio-frequency (RF) oscillating electric field(see the next section).

2.1.2 Synchrotron structure

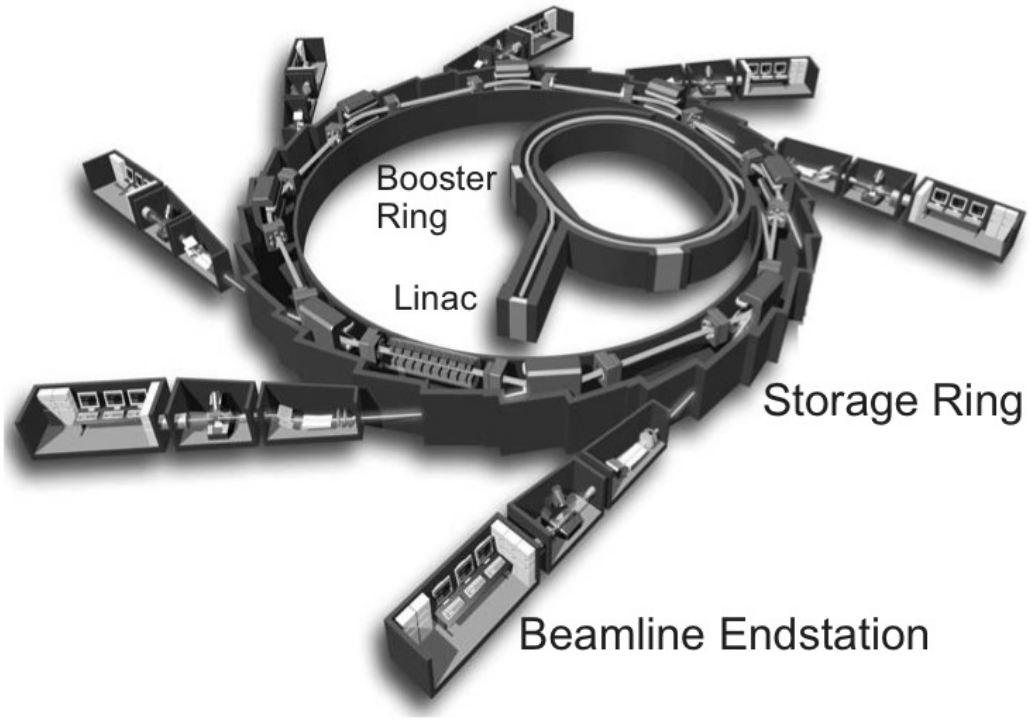

Figure 2.2: Typical schematic picture of a modern storage ring[44].

Figure 2.2 shows a typical synchrotron radiation facility of third generation like, e.g., ESRF. In these facilities, the electrons are produced by an electron gun and accelerated by a linear accelerator, so-called linac, which is located inside the actual storage ring. These electrons, that have now an energy around 200 MeV, enter the booster ring, where they are further accelerated up to a final value of 6 GeV via magnetic force. This part of the synchrotron is the reason for naming it this way,

derived historically from "cyclotron synchrotron", because the magnetic fields need to be simultaneously increased with increasing electron beam energy, due to the relativistic mass increase. Subsequently, electrons are inserted in the storage ring, where they will circulate for many hours doing 350000 rounds per second. To allow electrons to circulate on the desired trajectories, it is necessary to reach an ultra high vacuum level (10^{-9} to 10^{-11} mbar). This way they can have an average life up to 100 hours, during which they emit the desired SR, simultaneously used at several beam-line end-stations.

To summarize, the most important components of a modern storage ring are:

- The injection system, composed by linac and booster ring, which has already been described.

- The ultra high vacuum system (UHV), necessary to assure a long lifetime of electrons, obtained with a number of pumps distributed all over the ring.

- A radio frequency (RF) system: this is a radio frequency oscillating (352.2 MHz at the ESRF) electric field used in the storage ring to supply electrons with the energy they lose as a consequence of their acceleration. Also, the RF determines the so-called filling mode of the ring. In fact, a storage ring is never uniformly filled of electrons, but they are grouped in packages called bunches, which may contain a variable number of them. Fast timing techniques allow putting a bunch or a group of bunches in any buckets of the storage ring, as can be seen in Figure 2.3. Due to the RF voltage and phase stability conditions each bucket in the accelerator is equally distributed around the machine and the length between two bunches is therefore equal to the Radio Frequency wavelength. Then, the maximum number of bunches present in the ring is given by the ratio between the ring length and the RF wavelength (uniform filling). However, it is possible to reduce the number of bunches to increase the number of electron in every bunch, since this will increase the power of each emitted pulse.

- Magnets: The electron beam circulates inside the storage ring on a well-defined closed orbit, which is maintained by magnetic field forces. These forces are provided by a complex magnetic lattice around the storage ring, which also

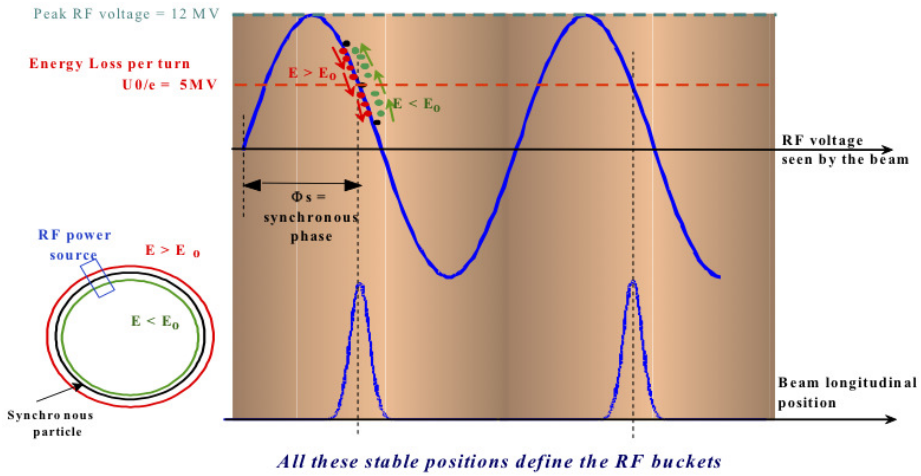

Figure 2.3: RF oscillating field and its use to restore the energy lost by electrons. The lowest part shows that a bucket is created in a certain position in space and this happens when the energy that the field carries equals the energy loss (from [45]).

ensures a well focused electron beam, especially within the insertion devices. The different kind of magnets and the property of the SR they produce will be described in the next section.

2.1.3 Magnets

The storage ring is provided with many kind of different magnets with the purpose of maintaining the desired circular orbit and of producing the SR.

BENDING MAGNETS (BM, Figure 2.4a) or dipole magnets are used both to curve the beam and to produce radiation tangential to the electrons orbit. They are conveniently placed in the ring to define the closed path that characterizes the accumulation ring; in fact, the storage ring is not actually circular, but formed by alternated straight and curved sections.

Concerning the SR emission, relativistic electrons circulating on a closed orbit within the storage ring and experiencing the transverse acceleration will emit the electromagnetic field (Figure 2.4b), which will appear to the observer in the laboratory frame as if all emitted in the general direction of motion. This forward collimation is particularly pronounced for charged particles traveling with a speed close to the speed of light. In this case, most of the electromagnetic field will be confined within

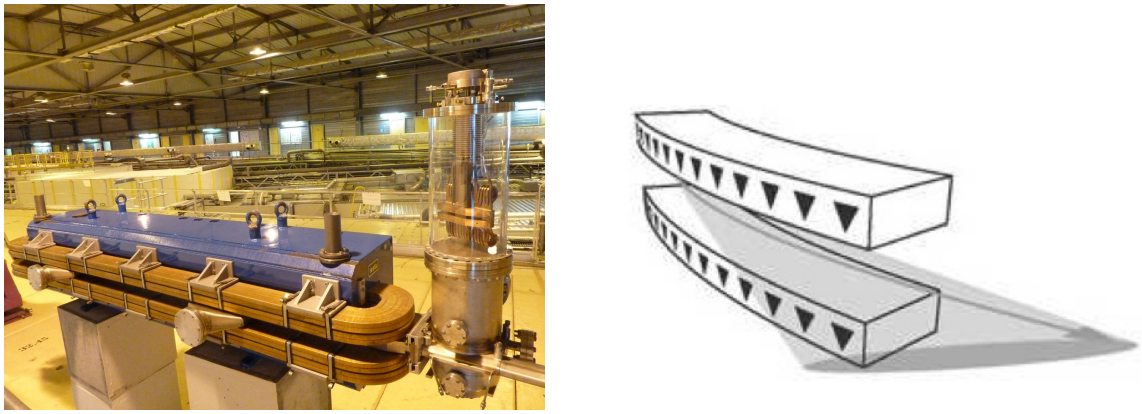

Figure 2.4: Left: Bending magnet at the ESRF. Right: schematic picture of radiation emission from a BM.

a small cone defined by an angle

$$\theta \sim \frac{1}{\gamma} \tag{2.8}$$

known as natural opening angle of the radiation, typically between 0.1-1 mrad (Figure 2.5) [46, 43].

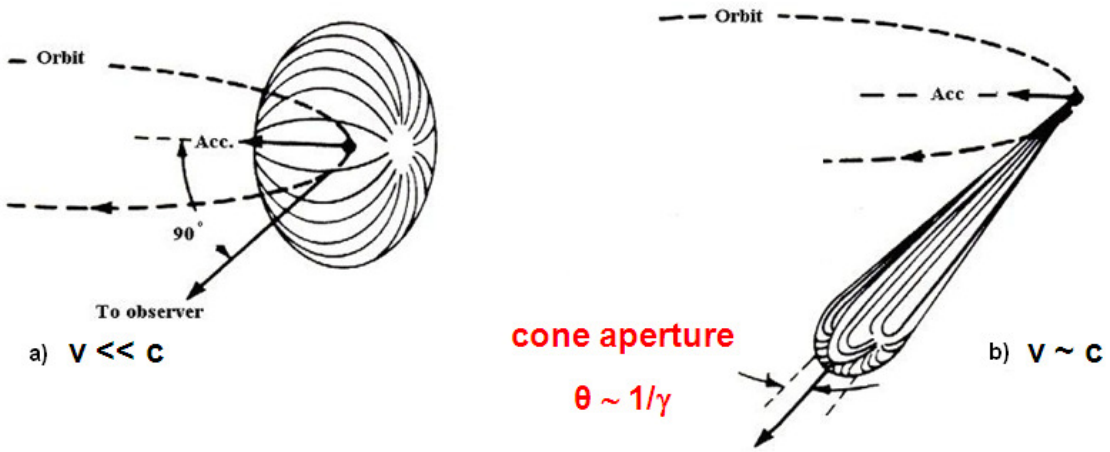

Figure 2.5: Emission of radiation from an accelerated electron as a function of its velocity. It is evident how the front lobe is favored as the speed approaches the speed of light. In b) the natural opening of radiation emission is evidenced[29].

The typical frequency emitted by a bending magnet can be estimated with general arguments, starting from the length of the radiation pulse seen by the observer in the laboratory frame. Such a length Δt is just the difference in travel time between the

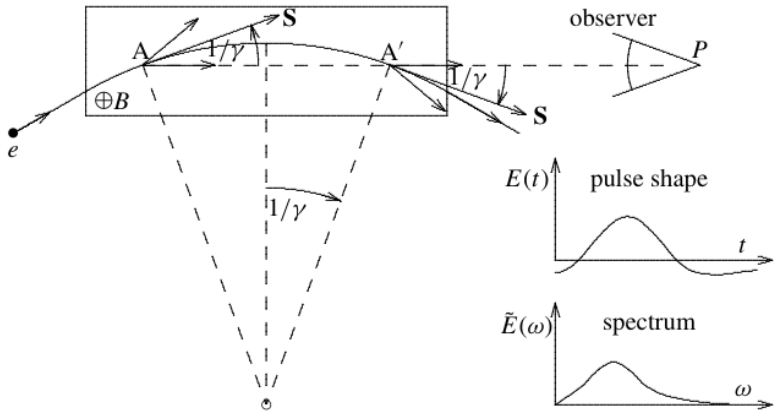

Figure 2.6: Trajectory of an electron in a BM. The observer sees radiation emitted from the electron starting when it is in A and ending when it is in A'[43].

charge and the radiation while going from point A to A' in Figure 2.6:

$$\Delta t = t_{el} - t_{ph} = \frac{AA'}{v} - \frac{\overline{AA'}}{c} = \frac{2\theta R}{\beta c} - \frac{2R\sin\theta}{c} = \frac{2R}{c}(\frac{1}{\beta\gamma} - \sin(\frac{1}{\gamma})) \tag{2.9}$$

where it was used that $\theta \sim 1/\gamma$. The sin function in the equation above can be expanded, for ultra-relativistic electrons, leading (thanks to $1 - \beta \simeq 1/2\gamma^2$) to

$$\Delta t \sim \frac{2R}{c\gamma\beta}(1 - \beta + \frac{\beta}{6\gamma^2}) \sim \frac{R}{c\gamma\beta}(\frac{1}{\gamma^2} + \frac{\beta}{3\gamma^2}) \sim \frac{4R}{3c\gamma^3}. \tag{2.10}$$

From this length Δt of the pulse we get the typical frequency of the spectrum ω_{typ} thanks to Heisenberg's principle:

$$\omega_{typ} \sim \frac{3c\gamma^3}{4R}. \tag{2.11}$$

A more quantitative and complete treatment can be done to derive the actual spectrum of a typical bending magnet, involving Bessel function dependences[43, 46]. The result is a very broad and continuous spectral intensity which varies little over an extended wavelength range, while it drops off exponentially at photon energies higher than the so called *critical photon energy* E_c given by:

$$E_c = \hbar\omega_c = \frac{3e\hbar B\gamma^2}{2m_0} \tag{2.12}$$

where B denotes the magnetic field strength. This energy is the energy for which half of the radiated energy is in higher energy photons and half is in lower energy photons (Figure 2.7).

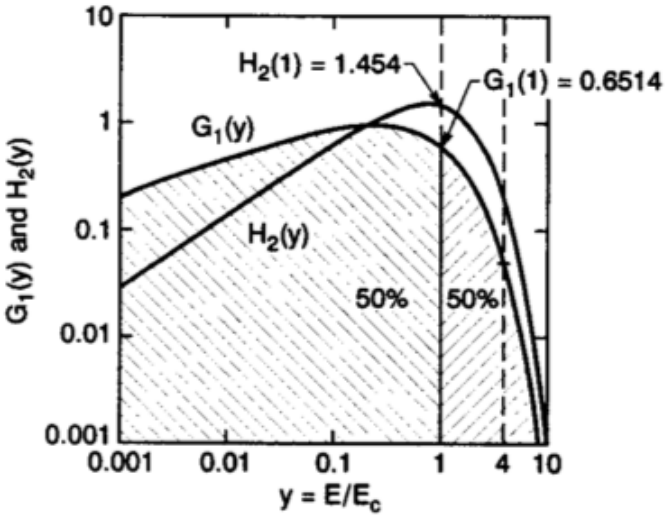

Figure 2.7: The function $H_2(y)$, representing the on-axis photon flux from a bending magnet and $G_1(y)$, representing the vertically integrated photon flux, as functions of photon energy normalized to the critical photon energy[46].

Concerning the total emitted power, it was already derived in equation 2.5. A problem of the radiation achieved with bending magnets is that they also define the storage ring geometry; therefore it is impossible to change the magnetic field strength easily and the critical photon energy remains fixed for a given geometry, and the same does the emitted power. For completeness, it should be noted that from eq.2.12, a critical angle can be defined in an analogous way as the critical energy, giving

$$\theta_c = \frac{1}{\gamma}(\frac{\omega_c}{\omega})^{1/3} \tag{2.13}$$

which justify the assumption that the angle of emission could be approximated as $1/\gamma$.

Finally, radiation from a bending magnet is linearly polarized when observed in the bending plane. Out of this plane, the polarization is elliptical and can be decomposed into its horizontal and vertical components[12].

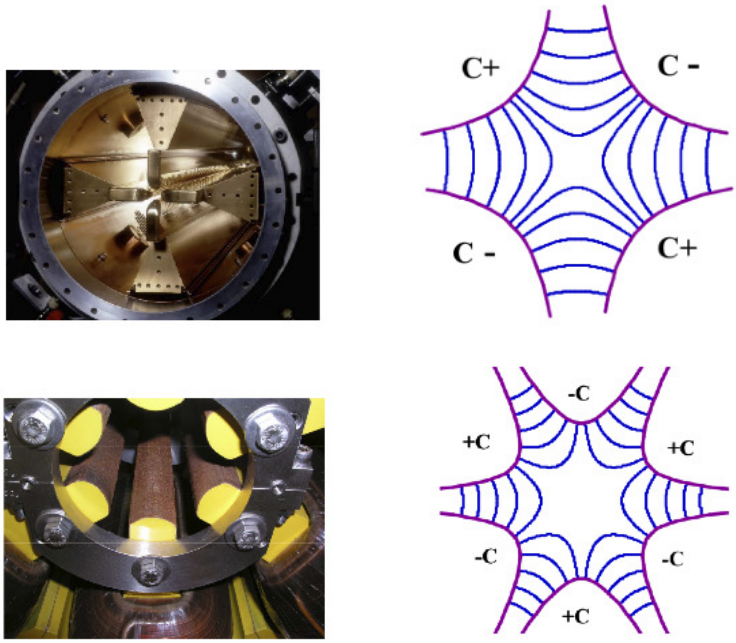

Figure 2.8: Left: Picture of quadrupole(top) and sestupole(bottom) magnets. Right: force lines of the magnetic field[29].

QUADRUPOLE and SESTUPOLE MAGNETS (Figure 2.8) are usually placed in the straight sections of the ring. They mainly provide two distinct functions: the first one tend to focus the beam such that it maintains its ideal orbit on the circular trajectory, while the second one corrects chromatic aberrations of the beam due to errors in the focusing of electrons with slightly different energy than the desired one.

INSERTION DEVICES (ID), whose name comes from the fact that they are inserted in a straight section of the ring, are magnetic complex structures used to produce SR with higher brilliance, directionality and monochromaticity. The term groups two kind of devices: *wigglers* and *undulators*, which have similar structure (Figure 2.9) but different properties. They consist of a periodic structure of length $L = N\lambda_u$, where N is the number of magnetic poles and λ_u is their characteristic wavelength and where the vertical magnetic field B varies sinusoidally along the undulator axis. The electrons passing through such a field will also undergo sinusoidal motion in the horizontal plane of the insertion device. An important parameter describing the electron motion within a periodic magnetic field of an insertion device

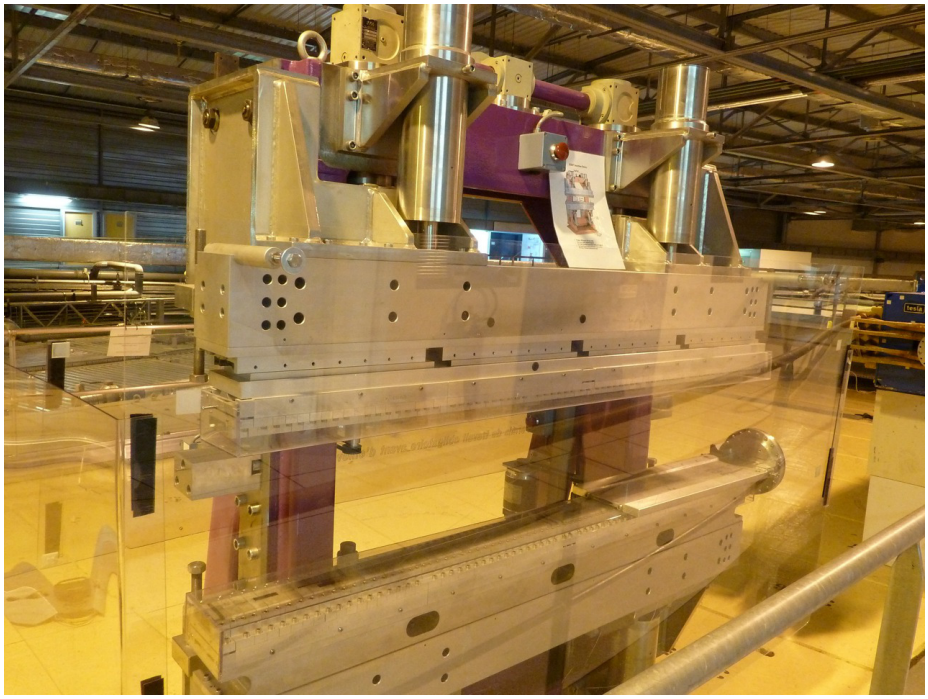

Figure 2.9: Insertion device at ESRF.

is called the deflection parameter K given by [47, 46]:

$$K = \frac{eB\lambda_u}{2\pi m_0 c} = 0.9337 \times \lambda_u\,[cm] \times B\,[T]\,. \tag{2.14}$$

The maximum angular deflection of electron motion, in terms of K, is equal to $\delta = K/\gamma$ and therefore we can distinguish two types of insertion devices depending on the deflection parameter strength. For $K \leq 1$ (weak field), the radiation from adjacent periods will interfere coherently, because the angular deflection of the electrons lies within the nominal $1/\gamma$ radiation cone and the magnetic structure is called an *undulator* (Figure 2.10a). The resulting spectrum consists of sharp peaks at harmonics of the fundamental wavelength ($n = 1$) and it is given by the so-called undulator equation:

$$E_n\,[KeV] = 0.9496 \times \frac{nE_e^2\,[GeV]}{\lambda_u\,[cm] \times (1 + \frac{K^2}{2} + \gamma^2\theta^2)}. \tag{2.15}$$

A consequence of this expression is that the fundamental wavelength (and its harmonics) can be shifted in energy by varying the magnetic field of the insertion device (by changing the gap between the magnetic poles) thus providing a fully tunable source over an extended spectral range. However, it should be noted that even harmonics radiate off-axis; therefore, their contribution is very small and the useful

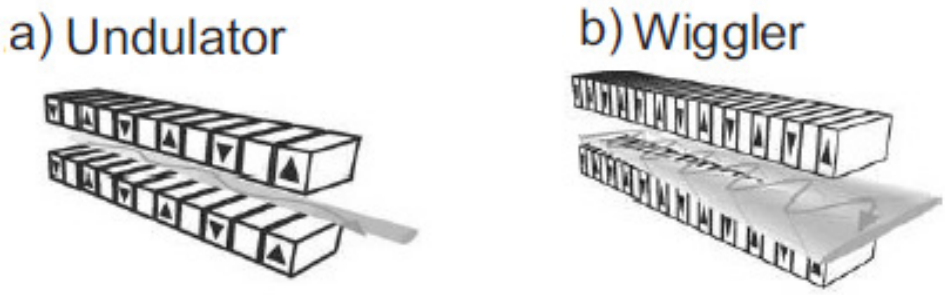

Figure 2.10: Scheme of an undulator (a) and a wiggler (b) with relative amplitude of electron oscillations. Adapted from [30].

intensity comes mainly from odd harmonics. Anyway, the relative bandwidth at the nth harmonic can be approximately expressed as

$$\frac{\Delta\lambda}{\lambda} = \frac{\Delta\omega}{\omega} = \frac{1}{nN} \qquad (n = 1, 2, 3 \dots). \tag{2.16}$$

On the other hand, in the strong field case ($K \gg 1$), the interference effects are less important because the radiation from various segments of an oscillation are widely separated in angle and therefore, after a short propagation distance, they do not overlap anymore in space. Also, the periodic undulator motion becomes distorted due to increased relativistic effects generating many higher harmonics of the single wavelength undulator radiation (Figure 2.11). The radiation from different parts of the electron trajectory adds up incoherently and the resulting spectrum merges all produced harmonics of the fundamental wavelength into a broad and continuous distribution similar to a bend magnet spectrum (the expression of the emitted spectrum is in fact the same). However, now the intensity is 2N-fold increased (as compared to the bend magnet radiated intensity). This kind of magnetic structure is referred to as a *wiggler* (Figure 2.10b).

Both wiggler and undulator radiation can be rationalized using the same physical phenomenon. Once the electron beam enters the periodic series of magnets within either of these devices, the electrons are forced to wiggle around the straight path as they feel the periodic magnetic field inside of it. As a result, a very high flux of x-rays can be achieved along either the wiggler or undulator beamline. The only difference is the deflection parameter K. In case of the undulator, the electron "wiggling" is much

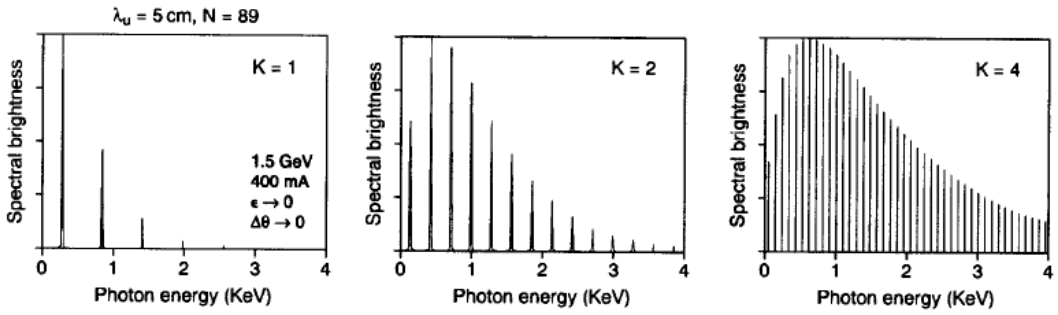

Figure 2.11: Transition from an insertion device in the undulator ($K \leq 1$) limit to one in the wiggler limit ($K \gg 1$) in shown, where is evident the increasing number of harmonics present in the spectrum. The wiggler spectrum eventually merges in a continuum spectrum as a consequence of other non-ideality effects, as finite emittance or big acceptance angle [46].

weaker and the synchrotron light continues to illuminate the undulator beamline continuously. The result is a longer pulse of light rather than a series of short bursts (wiggler). Given the absence of short burst of light, the resulting radiation bandwidth is smaller, thus the undulator emission is not spread in a broad band, like in case of a wiggler, but concentrated into harmonics, producing high levels of flux and brightness. The total power radiated by an undulator or wiggler is

$$P_T = \frac{N}{6} Z_0 I e \frac{2\pi c}{\lambda_u} \gamma^2 K^2 \tag{2.17}$$

where $Z_0 = 377$ Ohms or, in practical units,

$$P_T\,[KW] = 0.633 \times E^2\,[GeV]\, B^2\,[T]\, L\,[m]\, I\,[A]\,. \tag{2.18}$$

Finally, insertion devices usually produce linearly polarized radiation. Nevertheless, structures called helical undulators exist, with geometry modified in such a way that electrons have a spiral motion instead of a sinusoidal one. As a result, they have a significant vertical component of acceleration, which leads to a circular polarization [12]. This can be very useful for the study of samples with polarization dependent properties, such as magnetic materials.

2.2 Experimental setup at ID26

2.2.1 Beamline description

All spectra of this thesis have been recorded at the beamline ID26 of the ESRF, illustrated schematically in Figure 2.12. ID26 is an insertion device beamline, i.e. the X-ray source consists of three undulators inserted in a straight section of the ring, providing a very high photon flux (up to 10^{13} photons per second). The energy of the fundamental undulator harmonic is 2.35 KeV, which is thus the lowest achievable x-ray energy in the beamline. Higher energies can be obtained exploiting higher harmonics and the covered range extends up to 30 KeV.

The first component of the beamline is a set of vertical and horizontal primary slits, used to define the undulator emission axes and to reduce the power of the white beam received by a Horizontal Deflecting Mirror (HDM1). HDM1 is a flat silicon mirror that deflects laterally the beam away from the storage ring bremsstrahlung emission cone. This way, it damps the thermal power of the x-ray source down and protects the other optical components. The most important element is the monochromator, which selects the required wavelength and provides a monochromatic beam. It is placed right after the HDM1. The ID26 beamline uses a cryogenically cooled monochromator with two sets of Si crystals in (311) and (111) reflections. The theoretical resolution of the Si(111) ID26 monochromator is around 0.7 eV at the titanium K-edge energy (4966 eV). The direction of the exit beam is kept unchanged during energy scans. Beam focusing is achieved with two mirrors, placed after the monochromator, in a Kirkpatrick-Baez configuration, allowing independent variation of the horizontal or vertical beam-width at the sample by bending the mirrors with high voltage. The typical focal spot size at the sample location is around 600 μm (horizontal) x 100 μm (vertical).The incoming flux of photon is monitored by the scattering from a 1 μm-thick Silicon Nitride foil. Finally, fast shutters and slits are present to regulate the incoming power on the sample [49].

XANES, XES and RIXS measurements were all performed exploiting the wavelength dispersive x-ray spectrometer installed in the experimental hutch of the beamline. Its setup will be described in the next section. Besides, all measurements were

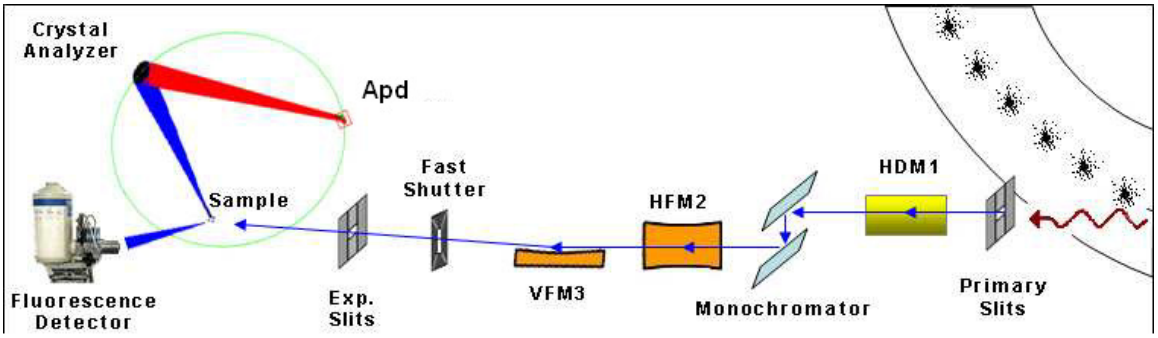

Figure 2.12: Experimental setup at ID26. HDM1 = horizontal deflecting mirror, HFM2 = horizontal focusing mirror, VFM3 = vertical focusing mirror, APD = avalanche photodiode[48]. The total size of the experimental setup, divided in three separate hutches, is about 20 meters.

taken in fluorescence detection (for XES this is obvious and for RIXS as well, since this is a second order process. XANES spectra, instead, were recorded in fluorescence with a variable incident energy and a fixed position of the spectrometer, i.e it was HERFD XAS) and the scans were done in a continuous mode, acquiring the data while the motors were driven; this reduces the dead time and the possible radiation damage effects on the sample. Furthermore, a beam shutter blocks the beam when no data are acquired to reduce the radiation exposure time of the sample. The detector used to acquire data was mainly an avalanche photodiode (APD) which is integrated in the spectrometer setup. Such a detector in very fast and allows to have a high count rate (up to 10^7 counts per second) with low dark counts (< 0.1 cps) while covering the entire spectral range used at the beamline. His bias was set in such a way that only the event of a single incoming photon is counted, while multiple events are rejected (no pile up effect) [50]. Occasionally, a normal photodiode was used to acquire total fluorescence yield's signal; in this case, obviously, the spectrometer was not necessary and the detector was simply placed close to the sample.

2.2.2 Wavelength dispersive spectrometer

The spectrometer installed at ID26 (Figure 2.13) is a wavelength dispersive spectrometer working in Rowland geometry, which consists of a bent Bragg crystal arranged with sample and detector in a circle, called Rowland circle. In this configuration the fluorescence from the sample is reflected by the crystal while both crystal and

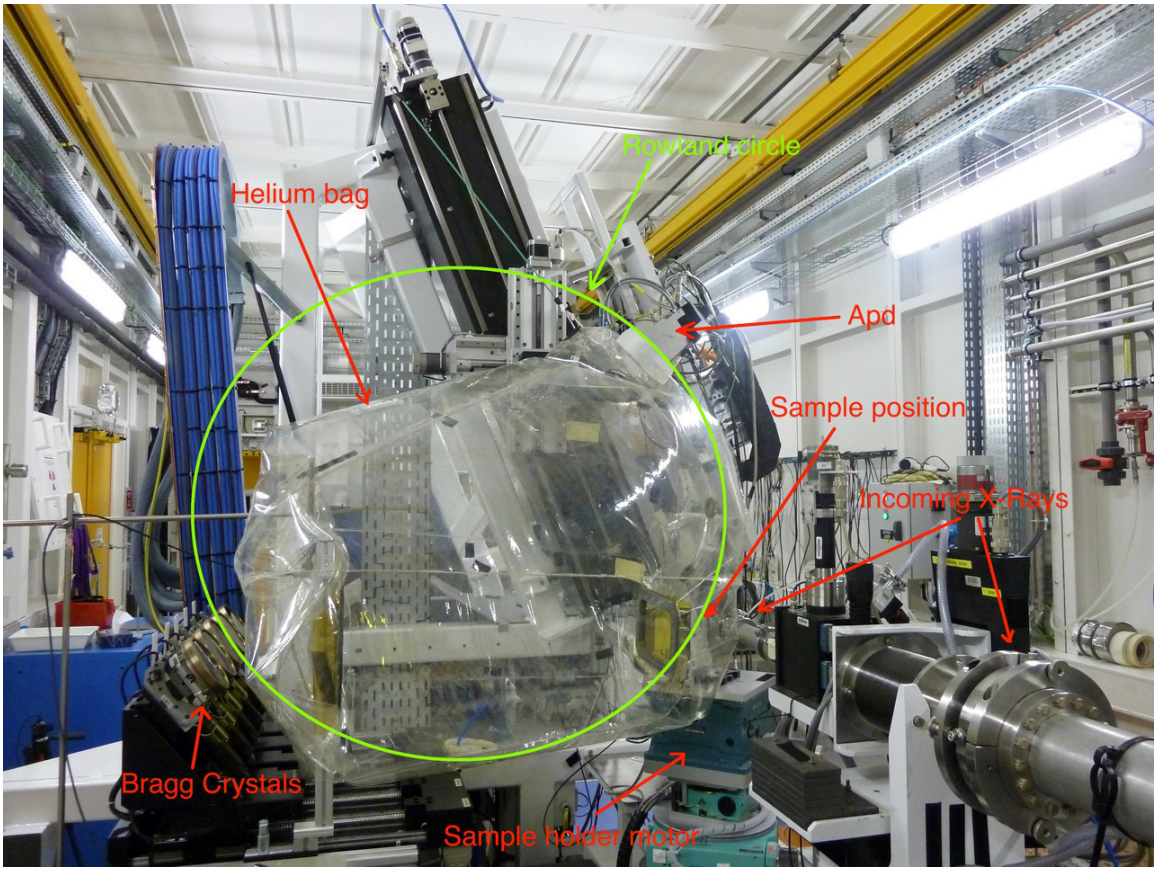

Figure 2.13: Wavelength dispersive spectrometer installed at ID26.

detector move along the circle.

The wavelength of the reflected radiation from the crystal, λ, can be obtained, assuming a unity refraction index, from Bragg's law [51]:

$$2d \sin\theta = n\lambda \tag{2.19}$$

with

$$d = \frac{a}{\sqrt{h^2 + k^2 + l^2}} \tag{2.20}$$

where a is the lattice parameter, h, k, l the Miller indices and θ the Bragg angle. Therefore the reflected energy is selected by a change in the angle formed by the normal to the crystal surface and the sample. Moreover, the fact that the crystal is bent combines its diffracting effect to a re-focalizing effect typical of curved mirrors.

There are two types of crystal analyzers useful to work in Rowland geometry (Figure 2.14). The first type, Johann crystal [52], is bent to a radius 2R (diameter of Rowland circle), such that the crystal planes are parallel to the crystal surface. This

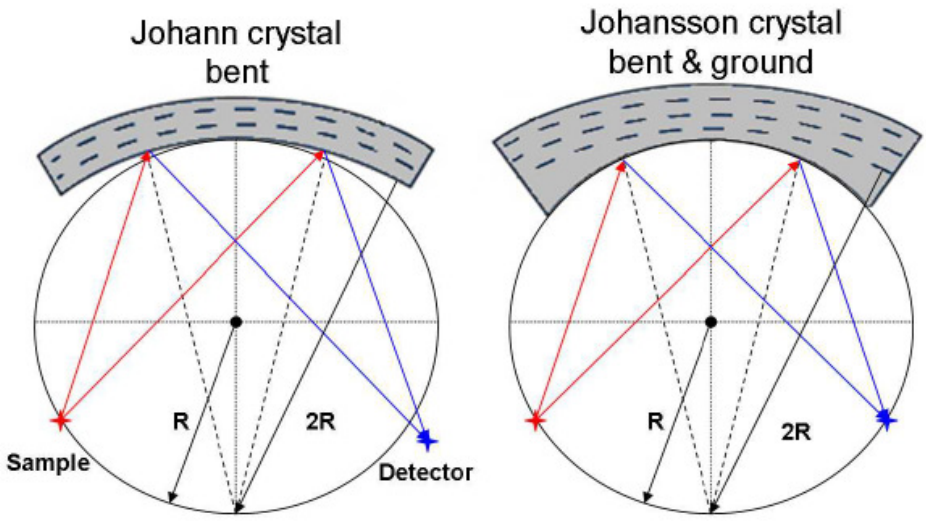

Figure 2.14: Johann and Johansson Bragg crystals in a Rowland circle[48].

geometry results in some broadening and asymmetry of the focusing point, because only the central point of the crystal is actually on the Rowland circle. This problem can be solved by grounding the surface to a radius R after the crystal is bent to the radius 2R, so that lattice planes are no longer parallel to the crystal surface, and all points of reflection in the scattering plane direction are focalized on the Rowland circle. This kind of crystal, which improves the resolution of the spectrometer, is called Johansson crystal [53]. By using Johansson crystals it is possible to eliminate one contribution to the final energy broadening, but it is important to remember that many other contributions are present, namely axial aberration (since the crystal extends out of the Rowland circle in the perpendicular direction to the scattering plane), finite size of the sample (not a point-like source), defectiveness of the crystal as a consequence of its bending and Darwin width of a perfect crystal (intrinsic broadening calculable with the dynamic theory of diffraction [54]). Best achievable result with the current setup is around 0.4 eV of energy resolution, but this strongly depends on the chosen crystal analyzer and relative Miller indices.

2.3 Conclusions

After describing how accelerated charges can lead to synchrotron radiation emission, the structure of a synchrotron facility was shown together with many technical aspects necessary to exploit this high energy radiation. Particular attention was given to bending magnets and insertion devices, which are the tool that allows to obtain very high radiation brilliance and short pulse length, which are often the most important aspects for modern experiments at third generation synchrotron facilities. Subsequently, beamline ID26 was described, since it is the place were all experiments of this thesis were conducted. As previously said, it is a beamline for x-ray spectroscopies equipped with a high resolution wavelength dispersive spectrometer, which allows XAS, XES and RIXS measurements to be made in a fully automated fashion.

Chapter 3

X-count

This chapter describes a *Matlab*® program developed at ID26 during my stay at ESRF. It is called X-count and it is an useful tool to describe photon-in photon-out experiments since it calculates the probability that a photon incident on a sample is absorbed and emitted again as a fluorescence photon that reaches the detector. Starting from this basics, many additional features were added to comprehend a wide range of physical effects. It is important to underline, as explained in the following, that the software is not thought to be a quantitatively exact instrument. It is, instead, a qualitatively useful tool to describe the order of magnitude of the output signal. Moreover, it simulates other physical effects that may follow the absorption of x-ray photons from complex samples, which contain different chemical elements, or self absorption effects. This way one can optimize the parameters of the experiment. Also, it can be used quantitatively in a comparative way, namely one has to measure a well known reference sample (which gives a strong signal) and use it to set the most critical parameters and subsequently one can use it to estimate the signal coming from more dilute or thin samples, which are the most critical because one does not know a priori whether it is possible to obtain signal enough or not.

3.1 Software Basics

Every experiment, before being performed, requires a serious planning to understand its feasibility and, if so, the best way to do it. For this reason, it can be useful a

software that allows to estimate the counts (in this thesis it is referred to a count as the result of a photon reaching a detector such as, e.g., an APD that operates in single photon counting regime) expected from a photon-in photon-out experiment, such as XES or High Energy Resolution Fluorescence Detected (HERFD) XAS.
X-count was developed to answer this necessity. It simulates the whole absorption and emission process, from the incident X-rays, via their interaction with the absorber atoms in the sample, to the fluorescent emission of another X-ray photon and its collection from a detector (which can be a solid state one, providing the energy resolution, or a generic one without energy resolution but placed in a spectrometer with Rowland geometry). It works in the hard x-rays region (energies from 1 KeV to 1 MeV, since this was the span of the available cross sections) where resonances are smaller and the x-rays penetration length is long, but in principle it could be expanded to lower energy regions too. This software was developed in a $Matlab^{®}$ environment and its main structure can be schematized as follows:

- Parameters input through the graphical user input (GUI) interface of Figure 3.1. All the parameters will be described in details in the next section.
- Calculation of the number of atoms for every element present in the sample.
- Cross sections loading; indeed, the program needs many values that are not usually known by the user to perform its calculation, such as photoelectric cross sections or fluorescence yields; thus, it loads cross sections and data tables from the Dabax Library[55].
- Calculation of absorption coefficients and of all necessary spectrometer parameters.
- Use of these values to compute the expected counts through 1.16, whose expression is reported here:

$$\frac{\Omega}{4\pi}\epsilon\frac{\mu_{abs}(E)}{\sin\theta}\frac{1-e^{-\left[d(\frac{\mu(E)}{\sin\theta}+\frac{\mu(E_f)}{\sin\phi})\right]}}{\frac{\mu(E)}{\sin\theta}+\frac{\mu(E_f)}{\sin\phi}} \tag{3.1}$$

- Graphic output and plots.

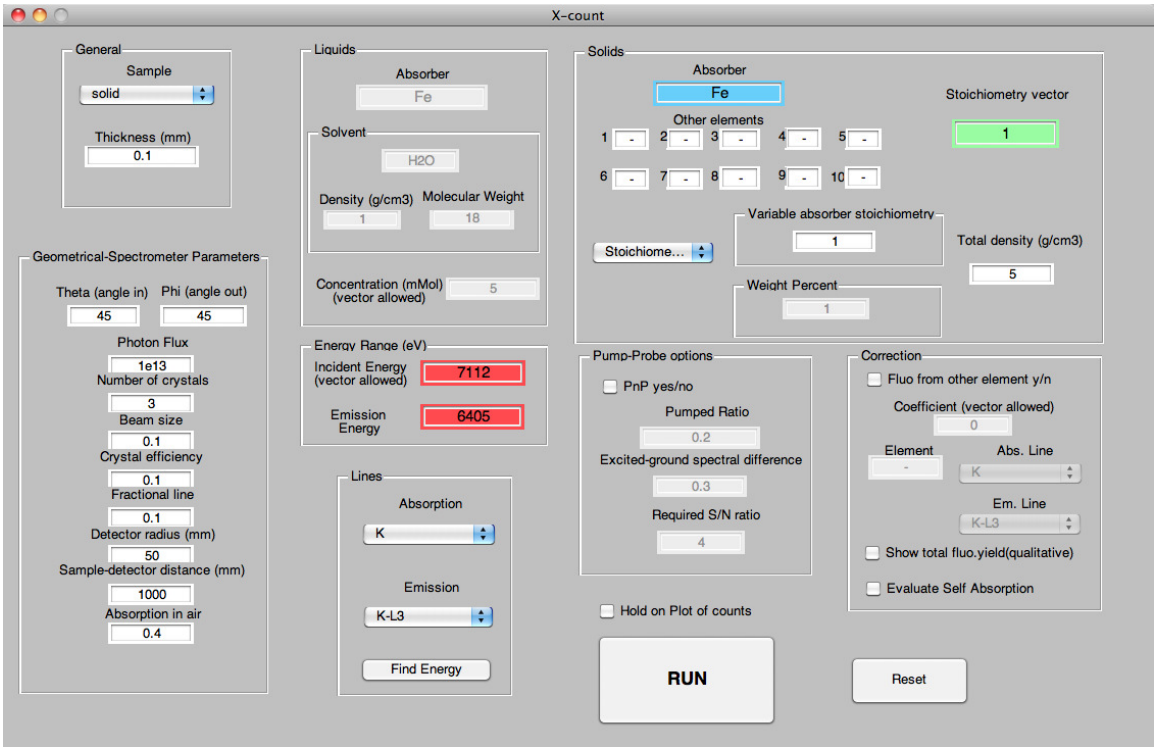

Figure 3.1: X-count Graphical User Interface (GUI).

3.2 Input and GUI

Figure 3.1 shows X-count's GUI. In the following the role of every parameter is described:

General

- Typology of sample, either solid or liquid.
- Thickness (in mm, it can be a variable).

Liquids

- Absorber element (it is important to remember that text is always case sensitive).
- Solvent (only water is available at the moment).
- Solvent density.
- Solvent molecular weight.

- Solvent concentration (mMol); it can be constant or variable (in this second case a vector should be typed).

Solids

- Absorber element.
- Other elements in the sample.
- Total stoichiometry vector (it is typed as a vector with the same order of the elements; absorber must be in the first position).
- Stoichiometry/Weight Percent: the concentration of the absorber element in the sample can be expressed in the most convenient way either by its stoichiometry (e.g. the sample is TiO_2 and the absorber is titanium, so that the stoichiometry is well known) or by its weight percent (e.g. the sample is Alumina (Al_2O_3) with a few ppm of titanium impurities, so that the stoichiometry of the absorber, titanium, is not known). These parameters can be constant or, whenever the user want to simulate an experiment while leaving the absorber concentration as a free parameter, he/she can select either a variable stoichiometry or a variable weight percent concentration via the following two options:
- Variable absorber stoichiometry: in this case the user has to type a vector for the variation of the absorber stoichiometry. This vector will multiply the first element of the total stoichiometry that had already been typed (e.g. Figure 3.2: Stoichiometry = [1 2 3] and variable stoichiometry = $[1 : 0.5 : 10]$ means that the absorber stoichiometry will vary from $1 \cdot 1$ to $1 \cdot 10$ in steps of 0.5). For this reason, the default value is 1, i.e. no change is applied by default.
- Weight percent: in this case the user has to type a number or a vector for the variable weight percent of absorber present in the sample (e.g. $[0.1 : 0.1 : 10]$ %). Thus, the stoichiometry of the absorber must be put to 1. (e.g. of Figure 3.3: from 1 to 10 % in weight of titanium in Al_2O_3. In this case, the stoichiometry must be [1 2 3] and the weight percent $[1 : 10]$).

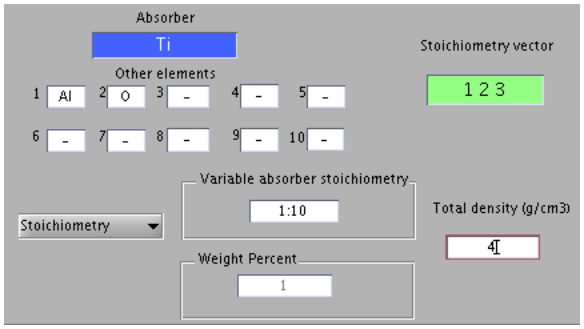

Figure 3.2: Input for variable absorber stoichiometry.

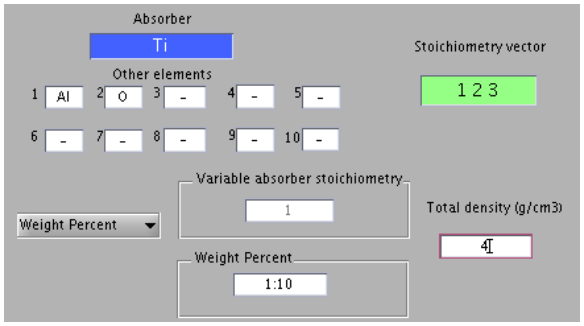

Figure 3.3: Input for variable weight percent.

- Total density of the sample (g/cm^3).

Geometrical - Spectrometer parameters

- Theta and Phi: incident and emission angles between photon direction and surface (Figure 1.16).
- Photon flux: photons/s that hit the sample.
- Beam size (mm^2, it is only used to estimate the flux density but it does not modify the counts).
- Crystal-detector efficiency: usually estimated as 0.1, it simulates the losses due to crystal's surface imperfections. Being just a reductive multiplicative factor, it could also represent detector's non-idealities. For this reason X-count can be also used for solid state detectors and not only for an experimental setup with a spectrometer.
- Fraction of emission line captured. It is the bandwidth of the detector, estimated as about 0.1. It simulates the fact that we do not measure

the entire emission line but only a fraction when measuring on the peak maximum, because the fluorescence yield refers to the entire spectral area.

- Detector radius (mm) used to calculate the solid angle.
- Number of Bragg diffracting crystals present in an evenctual spectrometer.
- Sample-detector distance (mm) used to calculate the solid angle.
- Absorption of X-rays by air and windows: number between 0 and 1, it represents the % of x-ray absorption during the path in air (path from x-ray emitter to sample) or by windows possibly present on it.

Energy range

- Incident X-ray energy (if concentration of absorber is constant, it can be a vector).
- Emitted fluorescence photon energy.

Absorption and emission lines

- Absorption line: it represents the absorption edge (if incident energy is a vector, it must contain this edge).
- Emission line: choice of the emission line (12 different lines are available; notation is $K - L_3$, $L_2 - M_4$ etc.).
- Find Energy: uploads tabulated values for incident and emitted energies corresponding to the selected edge and emission line.

With the parameters typed at this moment, the calculation can already be performed and the counts estimated. A few examples of the program's output can be found in Figure 3.4, Figure 3.5 and Figure 3.6.

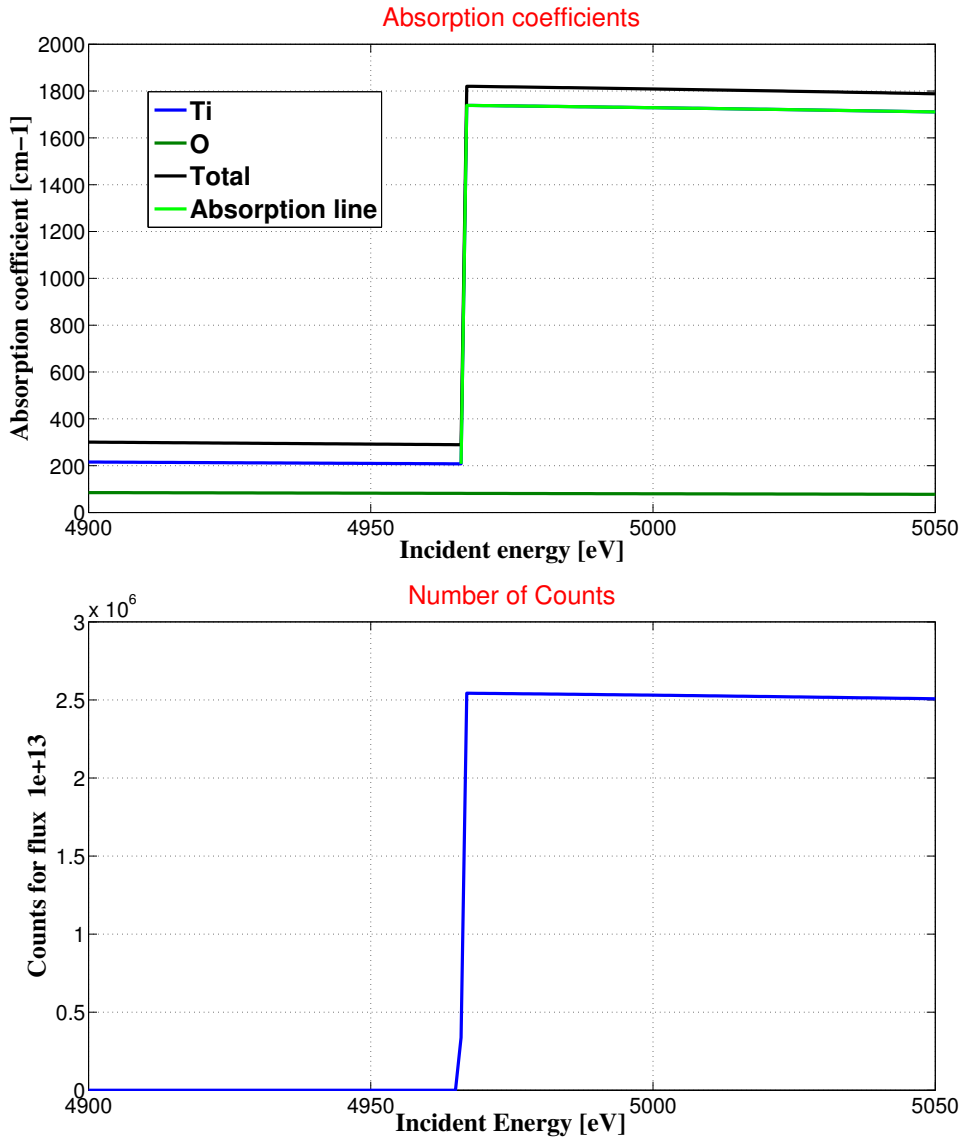

Figure 3.4: Titanium K edge absorption in TiO_2, with emission on K_α line. a) shows the absorption coefficients, b) the expected counts as a function of energy.

3.3 Calculations

Once all the inputs are inserted, the program starts the calculation to determine the *density of atoms* (number of atoms per unit of volume) present in the sample. For liquid samples, this value n is equal to:

$$n = N_A \left[\frac{atoms}{mol}\right] \cdot C \left[\frac{mmol}{l}\right] \tag{3.2}$$

where N_A is Avogadro's number and C is the concentration expressed as molarity. For solid samples, instead, this calculation depends on how the concentration is expressed.

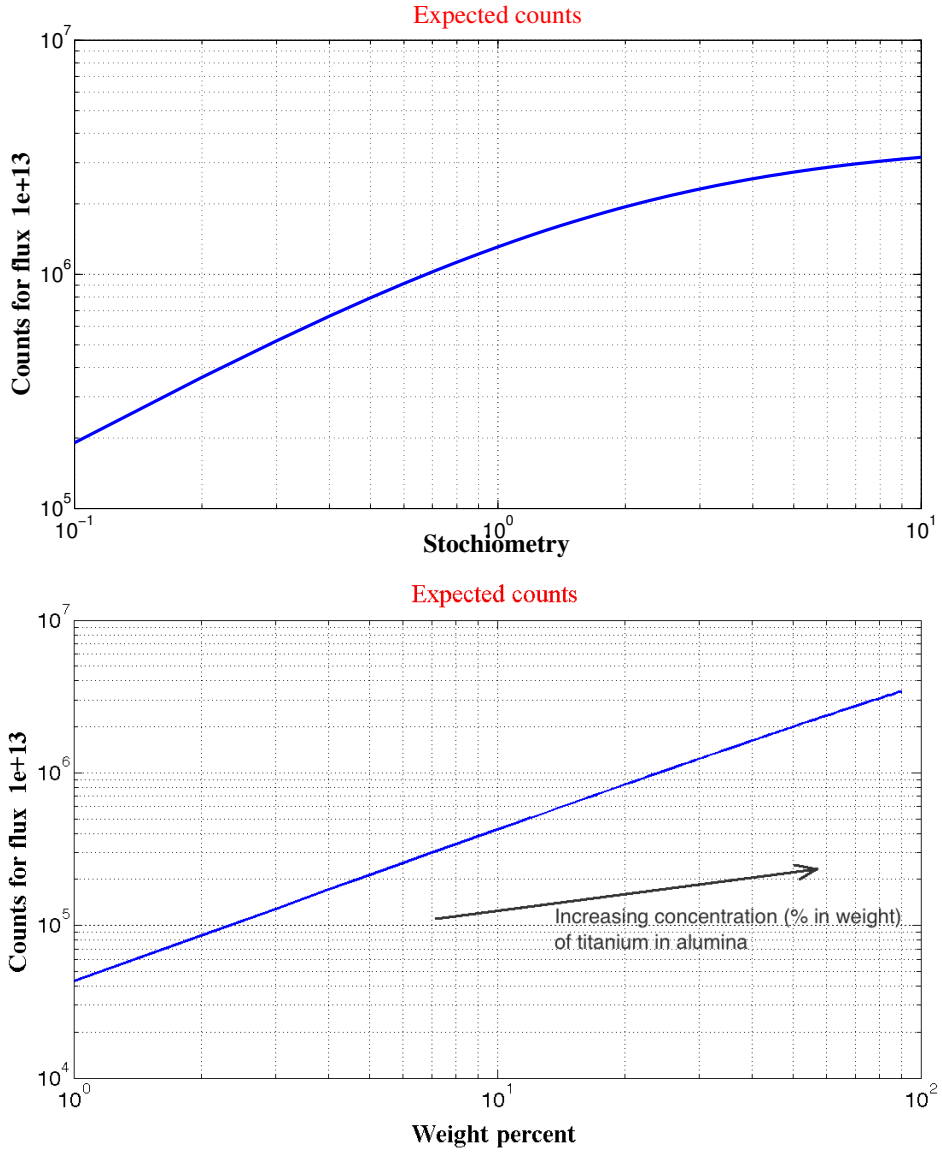

Figure 3.5: Titanium in Al_2O_3 estimated with absorption on K edge and emission line K_α. In a) stoichiometry is variable, which means the sample varies from $Ti_{0.1}Al_2O_3$ to $Ti_{10}Al_2O_3$. In b) weight percent is variable, which means that the sample is Al_2O_3 with impurities of Ti from 1% to 90% in weight.

If it is stoichiometry,

$$n = \frac{N_A \left[\frac{atoms}{mol}\right] \cdot \rho \left[\frac{g}{cm^3}\right]}{\sum_{i=1}^{N} MM_i \left[\frac{g}{mol}\right] \cdot S_i} \tag{3.3}$$

where ρ is the sample density, MM is the molar mass of each element, S the stoichiometry of each element and the sum extends over all N elements in the sample. If concentration is expressed in weight percent wp $(0 < wp < 1)$, instead, one has to find the absorber stoichiometry correspondent to the required weight percent. This

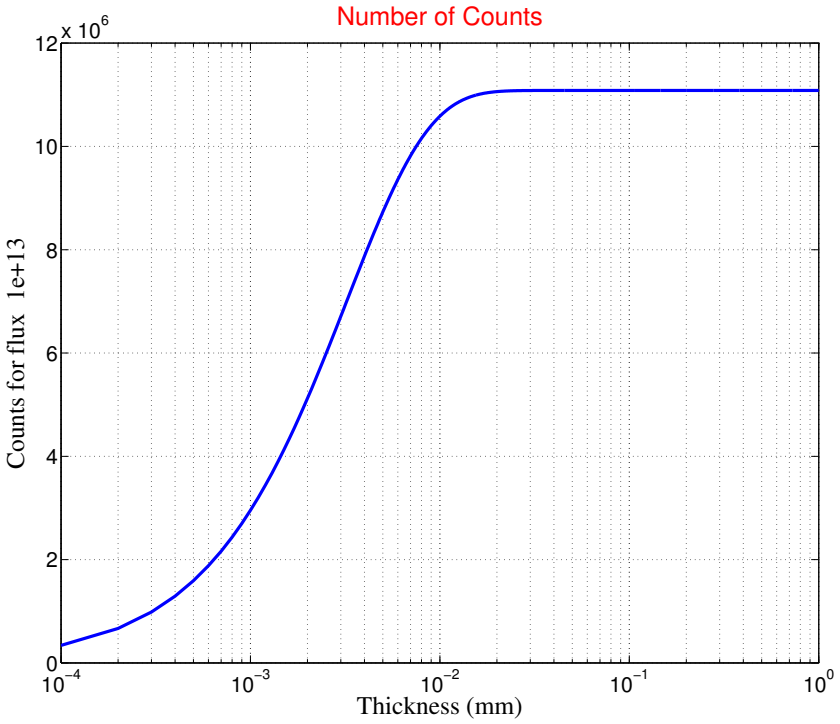

Figure 3.6: TiO_2 K edge with variable thickness of the sample.

is done via the proportion:

$$(MM_1 \cdot S_1) : wp = (\sum_{i=2}^{N} MM_i \cdot S_i) : (1 - wp) \tag{3.4}$$

and the required stoichiometry is found as

$$S_1 = \frac{wp \cdot (\sum_{i=2}^{N} MM_i \cdot S_i)}{MM_1 \cdot (1 - wp)}. \tag{3.5}$$

Now, the old value of S_1, set by default as 1, is replaced by the new one found with eq. 3.5 and with this value eq. 3.3 can be evaluated to find the density of atoms of each element. After this calculations, the program starts loading the *photoelectric cross sections* [55, 56] (which have units of barns/atom) and interpolates them in order to give them 1 eV energy resolution (they have very large energy steps since they cover the entire range 1 keV-1MeV). The interpolation is double, pre-edge and after edge, to generate realistic steep edges in case of K lines. For the same reason, in case of L lines the interpolation is quadruple and the result on the absorption coefficient is shown in Figure 3.7. Cross sections and density of atoms are simply multiplied to give the *absorption coefficients* in the most common unit of cm^{-1}. These are then

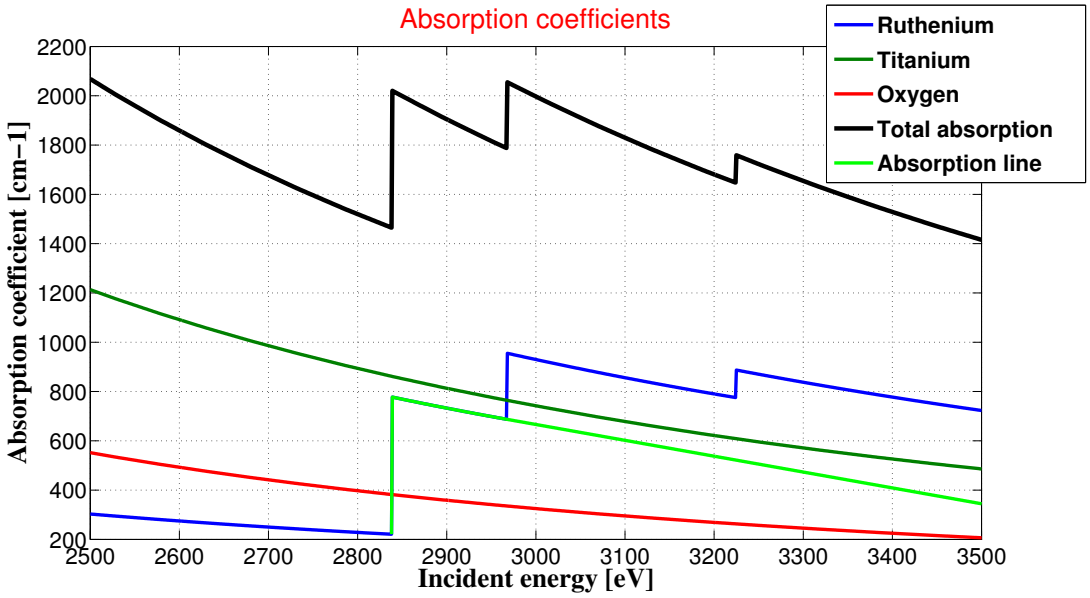

Figure 3.7: Ruthenium L edge in a solid sample of Ruthenium, Titanium and Oxygen. The steepness of the edges is obtained via interpolation in 4 different energy regions.

used to evaluate eq.3.1. To do this, the program also computes the fraction of *solid angle* subtended by the detector, calculated from input parameters as

$$\Omega = \frac{\pi R^2}{r^2}\frac{1}{4\pi}c \tag{3.6}$$

being R the detector radius, r the sample-detector distance and c the number of diffracting crystal, and the *fluorescence yield* function, i.e. a step function which is zero below the edge of interest and ϵ after it (where ϵ is loaded from tabulated values and it represents the probability that the core hole is filled via a radiative transition instead of a non-radiative (e.g. Auger) one).

The final counts are evaluated as:

$$Counts = I_f = I_0 \times y \times K \tag{3.7}$$

where I_0 is the incident photon flux, y is the result of eq.3.1 and K is a reductive factor that contains further different reductive contributions. Within these, two are loaded from tables, which are the *fractional fluorescence yield*, i.e. the probability that a radiative transition would happen on the selected emission line, and the *jumping ratio*, which defines how much of the photoelectric cross section is actually used to ionize the shell of interest (and not shells with lower binding energy). Being J the

jumping ratio, the multiplicative coefficient is $(J-1)/J$ [56]. The other reductive contributions come from inputs and represent the beam absorption in air, the crystal or detector efficiency and the fraction of emission line captured, as already explained in the previous section.

Once counts are calculated, outputs will be displayed. X-count has 4 main typologies of them. If concentration of the absorber element, thickness of the sample and incident photon energy are constant, the counts are simply displayed on the screen of the current matlab session (Figure 3.8). If not, the user can select a variable concen-

```
____________________count estimate for XES_________________

< Ti >
< O >

Absorption line K and Emission line K-L3
Considered values are:
Jump = 8.366
Fluorescence Yield = 0.208
Fractional Fluorescence Yield = 0.5842

Values for spectrometer and experimental geometry:
theta = 45
phi = 45
flux = 1e+13
efficiency = 0.1
fractional line collected = 0.1
detector radius = 50
number of crystals = 3
distance from sample = 1000
absorption in beam path = 0.4
Incident beam flux density is 1e+16 photons/cm^2

_________________ Calculation for solid ________________

Density for ABSORBER Ti is 3.19e+22 atoms/cm3
Absorber cross section at 4966 for ABSORBER Ti is 1730.4047 1/cm
Absorber cross section at 4509 for ABSORBER Ti is 271.7571 1/cm
Density for O is 6.38e+22 atoms/cm3
Absorber cross section at 4966 for O is 80.9577 1/cm
Absorber cross section at 4509 for O is 109.2732 1/cm
_____________________________________________________________
Solid angle of detector is 0.001875
Attenuation K = 5.7867e-06
Considered correction =    0
Integral = 0.0844
>>>>>>>>>>>>>>>>>> Expected counts are 9.5e+06 <<<<<<<<<<<<<<<<<<<<<<
```

Figure 3.8: Matlab screen after calculation on TiO_2 with all parameters constant.

tration, thickness or incident energy (by typing vectors). In this case, outputs will be plots having these variables on the x axis (i.e. as already shown in Figure 3.4, Figure 3.5 and Figure 3.6). On the GUI there is even a command to hold on plots between different iterations of the program. This is very useful to make comparisons

between calculations when a parameter is changed, even if legends and color of the plots usually do not match any more.

3.4 Additional options

Further options are available to simulate more advanced experiments:

3.4.1 Pump & Probe options

The main critical point in a PnP experiment is to achieve a sufficient signal to noise ratio, since the desired spectrum of the excited specie in the sample is often a small signal surrounded by a bigger steady state signal. The necessary parameters are:

- Pumped ratio coefficient. In PnP the total measured spectrum is the sum of the ground state one and the excited one: $S = fS_{exc} + (1 - f)S_{ground}$. The pumped ratio represents this coefficient f.
- Excited-ground spectral difference: $SD = (S_{exc} - S_{ground}/S_{ground})$ which is the spectral difference normalized between the excited spectrum and the normal spectrum.
- Required signal to noise ratio.

All this values are needed only to compute the number of counts necessary to achieve the S/N ratio above, following the relation:

$$Counts_{pnp} = \frac{2(S/N)^2}{(f \times SD)^2} \tag{3.8}$$

However, these parameters do not influence the expected counts and if the user is not interested it is just possible to leave the checkbox inactive. An example of the output can be seen in Figure 3.9.

3.4.2 Corrections

It often happens that samples are complex systems which contain many elements; this further elements may emit fluorescence and affect the expected counts. This can be simulated with the following parameters:

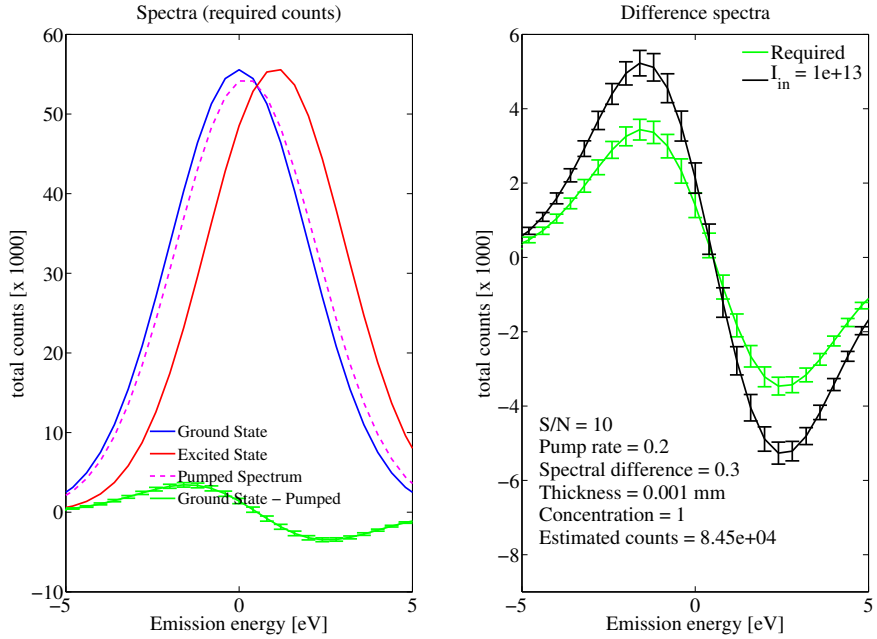

Figure 3.9: Titanium K edge in TiO_2 with emission on K_β line. Both incident energy and concentration are fixed. Left panel: spectral shape of ground, pumped, excited and difference spectra. Right panel: difference spectra shows how required counts to achieve a S/N of 10 are always lower than actual counts, which means that the PnP experiment will give a good signal.

- Fluorescence from other elements: takes into account the fact that another element in the sample is affecting the expected counts (this can happen if the energy of the incident photons reaches the edge of another element (Figure 3.10) and if such an element has an emission line that is close to the absorber element line of interest and finally if the energy resolution on the detector is sufficiently low not to resolve the different lines). For this purpose, the user shall type coefficient, element, absorption line and emission line.

- Coefficient: it must be a number between 0 and 1 (or a vector in the same range). This is used to modify 3.1 as follows: if this coefficient is zero, nothing changes and the expected counts are normally computed. Otherwise, in the left part of the equation the simple

$$\epsilon_{abs}\mu_{abs}(E) \tag{3.9}$$

is replaced by:

$$\{\epsilon_{abs}\mu_{abs}(E) + c\,[\epsilon_{elem2}\mu_{elem2}(E)]\}. \tag{3.10}$$

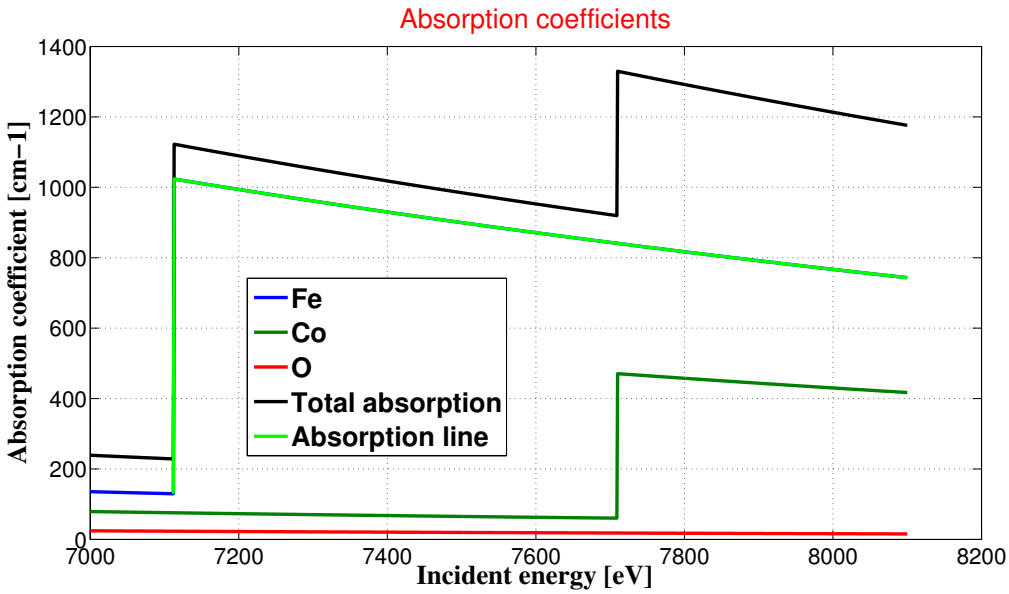

Figure 3.10: Absorption coefficients of $CoFe_2O_4$. It is visible how the cobalt K edge modifies the profile of the total absorption coefficient.

C is the coefficient that estimates what is the % of emission line from another element that is collected by the detector.

- Element: it is the name of the element that affects expected counts.
- Absorption line: for the element above, the absorption edge must be specified.
- Emission line: for the element above, the emission line must be specified. (These two parameters are used to fully correct fluorescence yield, fractional fluorescence yield and jumping ratios, as explained previously).
- Show total fluorescence yield (qualitative): in this case the program shows the counts one would have if 3.9 was changed to:

$$\{\epsilon_{abs}\mu_{abs}(E) + \epsilon_{elem2}\mu_{elem2}(E) + \cdots + \epsilon_{elemN}\mu_{elemN}(E)\}. \tag{3.11}$$

This means that the program estimates counts coming from all the elements in the sample, without any emission energy discrimination, as one would see, e.g., from a photodiode. However, it must be underlined that no informations are given by the user about the absorption/emission lines that are really playing a role in the total fluorescence, so no correct values for jumping ratios and

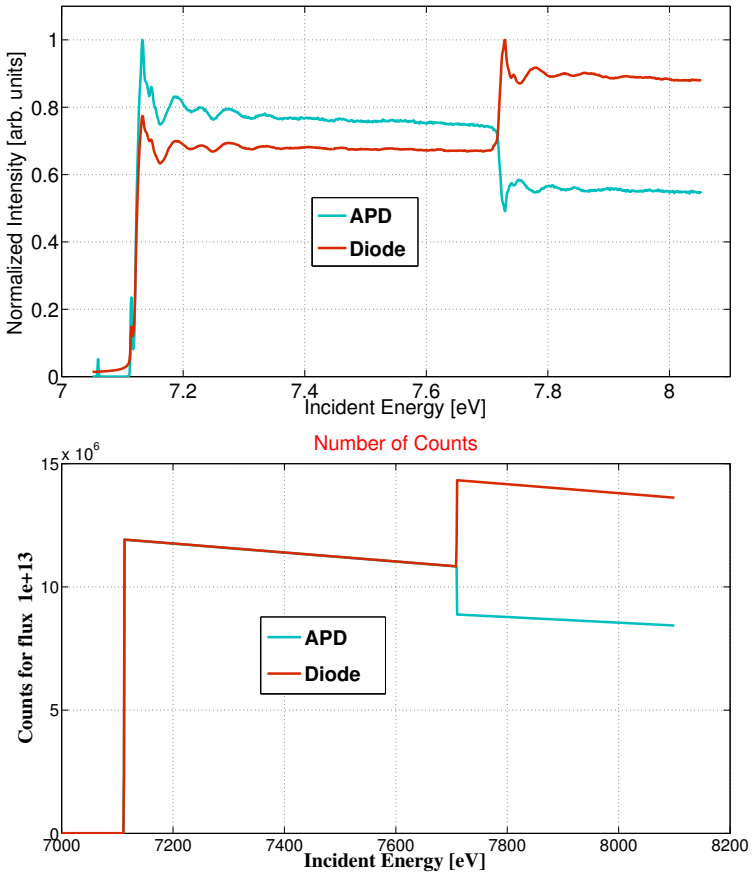

Figure 3.11: Signal expected from a 10 μm thick sample of $CoFe_2O_4$ from different detectors: APD with spectrometer and photodiode. Real measurements normalized in peak (top) and simulated values (bottom).

fractional fluorescence yield are used. Thus, the output plots only have a qualitative value. Nevertheless, Figure 3.11 shows a real measurement on a sample of $CoFe_2O_4$, compared to the simulated output from X-count. Although the quantitative values cannot be compared, it is evident how the program is fully able to reproduce the behavior of the signal expected from an APD placed in a spectrometer (thus, with emission energy discrimination) and from a photodiode (thus, without emission energy discrimination). Indeed, the former shows a pronounced dip when the incident energy reaches the edge of cobalt, due to the fact that its presence increases the TOTAL absorption coefficient, which is present in 3.1 in the denominator. On the other hand, the second one shows a strong increase in the expected signal because now the total absorp-

tion coefficient in the denominator is not anymore the term that dominates the equation. The dip present in Figure 3.11 is really important because it significantly modifies the measured spectrum and therefore it makes impossible to correctly analyze EXAFS measurements, since the oscillations are modified by the dip. The strength of this feature depends on the iron concentration and on the thickness of the sample, since if they are small the exponential term in 3.1 becomes important and tends to cancel the dip. Hence, a good choice of these parameters makes the difference between useful and useless measured spectra. In fact, it is useful only if the dip is small ($\sim$ 1 %) compared to EXAFS oscillation and for this reason X-count is an important tool to simulate the dips strength.

3.4.3 Evaluate Self Absorption

With this option, the program tries to estimate the degree of self absorption present in the sample. This well-known phenomenon has already been touched in chapter 1 but a deeper understanding is required.

We see from 3.1 that the proportionality between the achieved signal and $\mu_{abs}(E)$ in not direct because $\mu_{abs}(E)$ is also included in $\mu(E)$ and therefore it also appears in the denominator and in the exponential function. For thin samples, the exponential can be Taylor expanded at the first order, such that 3.1 becomes

$$\frac{\Omega}{4\pi}\epsilon\frac{\mu_{abs}(E)d}{\sin\theta} \tag{3.12}$$

and the linear relation is fulfilled.

For thick samples, instead, the exponential can be neglected and 1.16 becomes

$$\frac{\Omega}{4\pi}\epsilon\frac{\mu_{abs}(E)}{\sin\theta}\frac{1}{\frac{\mu(E)}{\sin\theta}+\frac{\mu(E_f)}{\sin\phi}}. \tag{3.13}$$

In this case, if the sample is diluted, e.g. $\mu_{abs}(E) \ll \mu_{else}(E) \sim \mu(E)$, the absorption coefficient is multiplied by a slowly varying function of energy (as long as no other elements have an absorption edge in the range of interest) and what one measures is really close to the actual absorption coefficient. On the other hand, concentrated samples have $\mu_{abs}(E) \sim \mu(E) \gg \mu_{else}(E)$. Thus, neglecting the angles for simplicity,

one measures

$$\frac{\Omega}{4\pi}\epsilon\frac{\mu_{abs}(E)}{\mu_{abs}(E)+\mu_{abs}(E_f)} \tag{3.14}$$

where it is evident that the absorption coefficient is present both in the numerator and in the denominator, resulting in an hyperbolic behavior of the measured coefficient as a function of the real one. This means that the measured spectrum has strongly suppressed features (if $\mu_{abs}(E_f)$ was not present, one would have a completely featureless spectrum). This well-known effect is named *self-absorption* and it is the main limiting factor of fluorescence mode detection. Physically, this phenomenon is simply explained: when the sample is thick and the absorber concentrated, the penetration depth into the sample is dominated by the element of interest. In this case, while scanning the incident energy, the main aspect that changes is the photon penetration depth into the sample, but essentially all the x-rays are absorbed by the element of interest. The escape depth for the fluoresced x-ray is generally much longer than the penetration depth, so that basically all absorbed x-rays cause a fluoresced x-ray found on the detector. But, since different incident energies interacted with the sample for a different distance, those who interacted less (because the absorption coefficient was strong) give a lower contribution and this severely dampens the XAFS oscillations on the edge, while those who interacted more (because the absorption coefficient was weak) give a stronger contribution. E.g., pre-edge structures can result stronger than they really are, with respect to the edge structure, not for a real physical effect but only because pre-edge the penetration depth of the photons is higher and thus a longer distance in the sample is probed in this case. A simple solution to reduce this effect is to measure in a grazing exit angle limit, i.e. incident angle around 90 degrees and exit angle very small. This way, $\frac{\mu_{abs}(E_f)}{\sin\phi}$ may become much bigger than $\frac{\mu_{abs}(E)}{\sin\theta}$ and a linear relation is fulfilled again. However, this is not always possible and in literature are present some solutions about how to correct this effect, specially in EXAFS experiments where the intensity of oscillations is very important for determination of structural parameters. In particular, theoretical analysis is developed in [57, 58, 59] and computational tools to reconstruct self-absorption free spectra are described in [60, 61].

From this treatment, the question rises whether one could estimate the relevance

of the self-absorption effect before performing the measurement. A self absorption-free measure would need the ideal situation in which the measured quantity is always directly proportional to the absorption coefficient $\mu_{abs}(E)$. In real life of course this does not happen and, mostly in case of concentrated samples, the measure does not fulfill this direct proportionality any more. However, in the simulation one can try to force this linearity in order to estimate the committed error.

To understand this, it is useful to rewrite 3.1 as:

$$\frac{\Omega}{4\pi}\epsilon\mu_{abs}(E)\frac{1-e^{-\left[\frac{d}{\sin\theta}(\mu_{tot}(E)+g\mu_{tot}(E_f))\right]}}{\mu_{tot}(E)+g\mu_{tot}(E_f)} \tag{3.15}$$

where is $g = \frac{\sin\theta}{\sin\phi}$ and $\mu_{tot} = \mu_{abs} + \mu_{else}$. Now it is important to underline the dependence of this expression from $\mu_{abs}(E)$. For this reason, with the substitutions $x = \mu_{abs}(E)$, $\alpha = \mu_{else}(E) + g\mu_{tot}(E_f)$ and $\beta = d/\sin\theta$ and neglecting the constant terms, the expression above can be written in the form:

$$y = x\frac{1-e^{[-\beta(x+\alpha)]}}{x+\alpha} \tag{3.16}$$

As already shown previously, this equation becomes linear if the sample is very thin, i.e. $\beta \ll (x+\alpha)^{-1}$, because then

$$1-\exp\left[-\beta(x+\alpha)\right] \sim \beta(x+\alpha) \tag{3.17}$$

and

$$y = \beta x. \tag{3.18}$$

If it is thick, instead, $\beta \gg (x+\alpha)^{-1}$ and the exponential term goes to zero, which gives

$$y = \frac{x}{x+\alpha} \tag{3.19}$$

which is clearly an hyperbolic behaviour, i.e. if the absorption coefficient x is big, the measured quantity y is much lower than the real x. Of course, if it is small instead (but still big enough to consider $\beta \gg (x+\alpha)^{-1}$), the hyperboles can be expanded in a neighborhood of the origin giving the linear

$$y = \frac{x}{\alpha}. \tag{3.20}$$

The main idea behind the Self Absorption estimation is to apply a Taylor expansion to eq.3.16 around $x = 0$, without doing any thickness consideration a priori. This means that we consider the case where concentration is not high enough to generate self absorption and therefore the obtained counts are directly proportional to the absorption coefficient. At first order one obtains:

$$y = x\frac{1 - e^{-\alpha\beta}}{\alpha}. \tag{3.21}$$

This approximation is exactly the needed one, because it eliminates the absorber element contribution in the denominator and in the exponential, thus excluding any effect possibly coming from a different probed length in the sample. Moreover, eq.3.21 reduces to eq.3.18 and to eq.3.20 in the very thin and very thick sample regime, respectively, but it is a much better approximation in the intermediate regions, as one could observe in Figure 3.12 and Figure 3.13.

Going back to the general case, the right part of eq.3.21 becomes

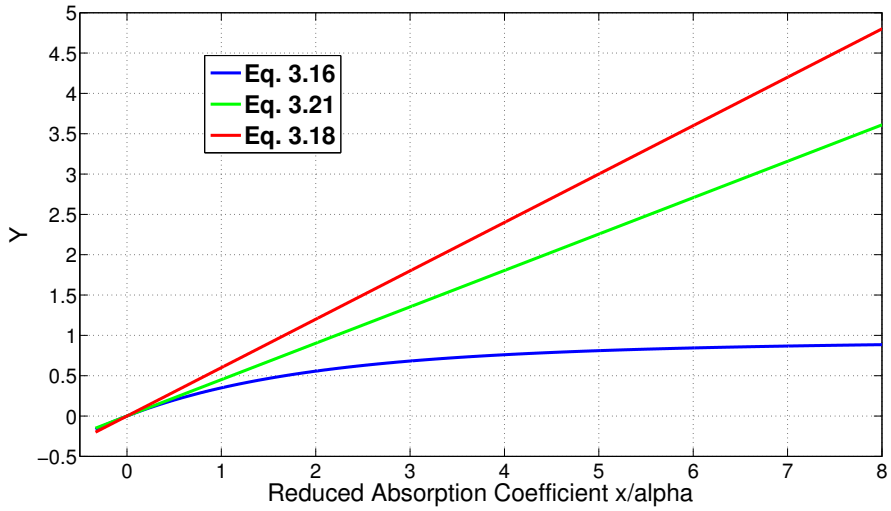

Figure 3.12: Comparison between eq.3.18 and eq.3.21 as different approximations of eq.3.16. The selected values here were $\alpha = 300\,cm^{-1}$ and $\beta = 0.002\,cm$, so it holds the thin sample regime. It is clear how eq.3.21 is the best approximation. Of course, the smaller the thickness become, the more the two approximations coincide.

$$\frac{\Omega}{4\pi}\epsilon\mu_{abs}(E)\frac{1 - e^{-\left[\frac{d}{\sin\theta}(\mu_{else}(E)+g\mu_{tot}(E_f))\right]}}{\mu_{else}(E) + g\mu_{tot}(E_f)} \tag{3.22}$$

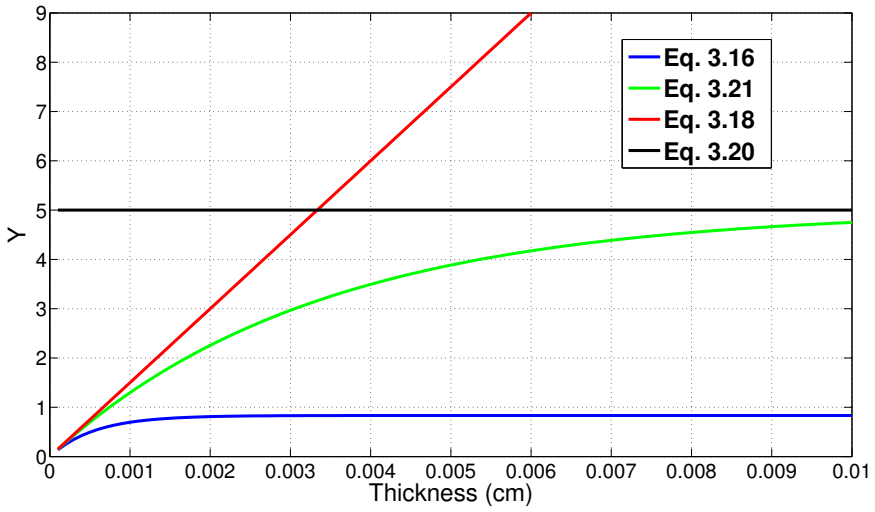

Figure 3.13: Behavior of eqs.3.18, 3.20 and 3.21 as approximations of eq.3.16 for variable thickness. Selected values were $\alpha = 300\,cm^{-1}$ and absorption coefficient $x = 1500\,cm^{-1}$. It should be noted that eqs.3.18 and 3.20 represent the asymptotic behavior of eq.3.21.

which in the case of a thick and concentrated sample reduces to:

$$\frac{\Omega}{4\pi}\epsilon\frac{\mu_{abs}(E)}{\mu_{else}(E)+g\mu_{tot}(E_f)} \tag{3.23}$$

i.e. the denominator is only a constant (or slowly varying) term, which means no damping of XAFS signal and of its features. One could obtain the same result by neglecting $\mu_{abs}(E)$ in assumption 1.13, which makes physical sense because this way one neglects the absorption of the absorber element at the incident energy while deriving the final expression and this further justify the mathematical procedure.

At this point, the program has both the real counts and the counts calculated with 3.22, which are usually much more because they are SA free. SA can be estimated in many ways but what the program shows, when the option is selected, are plots of the obtained counts versus the ideal counts and, also, SA expressed as a %. It is defined as:

$$SA = \frac{Counts_{noself} - Counts_{obtained}}{Counts_{noself}} * 100 = (1 - \frac{Counts_{obtained}}{Counts_{noself}}) * 100. \tag{3.24}$$

This is 0 if the counts obtained in the experiment are equal to the self absorption free counts and goes to 100% when obtained counts are much less than the SA-free ones. This way, if one has a spectrum affected by self-absorption, it is possible to

reconstruct a more realistic spectrum by applying:

$$Counts_{noself} = \frac{Counts_{obtained}}{1 - (SA/100)}. \tag{3.25}$$

Figure 3.14, Figure 3.15, Figure 3.16 and Figure 3.17 are examples of the program's output. The first one and the second one show SA estimation as a function of incident energy for different thicknesses and for different incident angles, the third one shows it as a function of the concentration while the last one as a function of thickness. It is interesting to notice how in Figure 3.16 counts have a plateau even in absence of self absorption. From eq.3.21-3.22 one would not expect so, but this happens because when the concentration is sufficiently high, the sample actually contains only atoms of the absorber element; this way, the plot shows 3.23 where $\mu_{else}(E)$ and $\mu_{else}(E_f)$ are close to zero and therefore $\mu_{abs}(E)$ and $\mu_{abs}(E_f)$ increase in the same way, following the increase in concentration. Since this two quantities are at the numerator and denominator, respectively, the counts plateau at their maximum possible value, which means that all incident photons are converted in fluoresced photons, i.e. eq.3.16 does not reduce the expected counts (however, other reductive factors like fluorescence yield or solid angle are still present).

The SA estimation described above works nicely, although we recently observed how it usually gives an overestimation. Therefore we are currently working to improve it with a more realistic estimation. This will be achieved with a Taylor expansion of 3.16 around the absorption value below the edge, instead of doing it around zero. This means replacing $\mu_{abs}(E)$ in the denominator and exponential of 3.16 with the constant value $\mu_{abs}(E_0)$, where E_0 is the energy just below the edge of interest, instead of putting it to zero. This way SA should be less pronounced and more faithful to the physical nature of the process, since it is obviously a strong approximation to think that the penetration depth into the sample is completely unaffected by the absorber element.

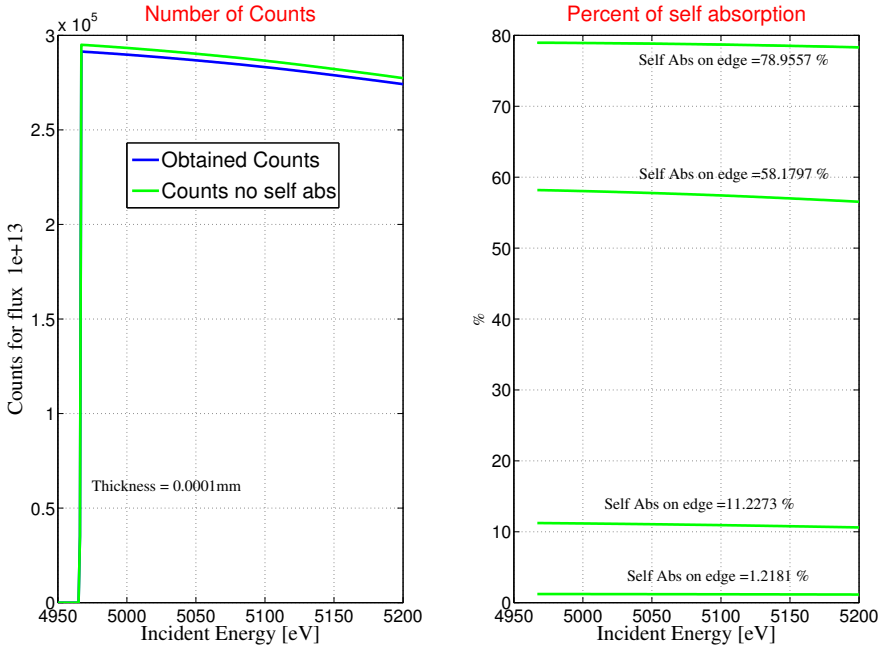

Figure 3.14: Titanium K edge on TiO_2 with emission on K_α line. Left panel: counts expected and SA-free counts from a $0.1\mu m$ thick sample. Right panel: % of self absorption for the 4 different thicknesses of $0.1\mu m$, $1\mu m$, $10\mu m$ and $100\mu m$, respectively from the bottom to the top.

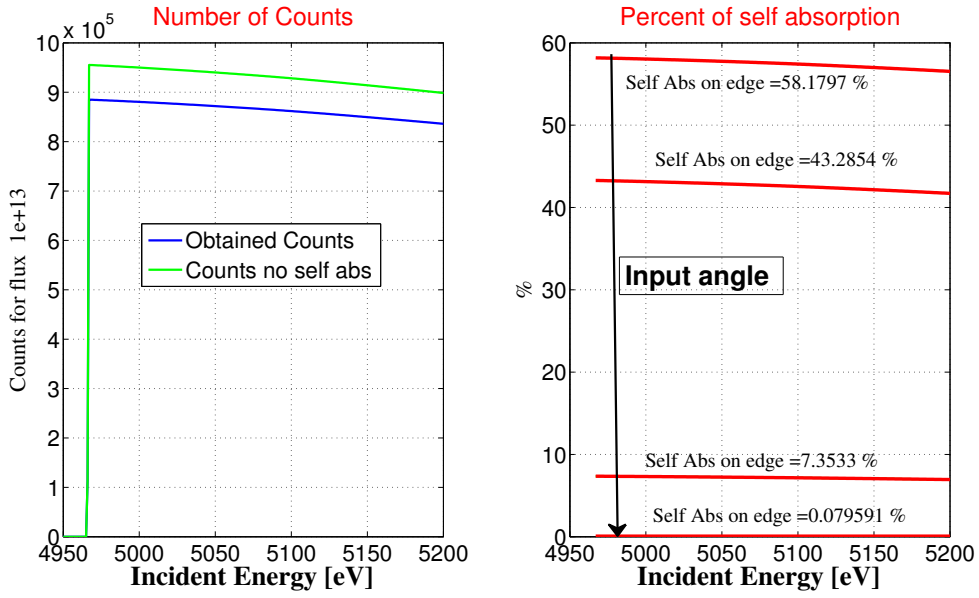

Figure 3.15: Self-absorption estimation on titanium K edge with various incident angles. On the left, counts for $\theta = 75°$ and $\phi = 15°$. On the right, SA for θ=45, 75, 89 and 89.99 degrees (and ϕ complementary) where it is shown how SA goes to zero while θ approaches grazing incidence.

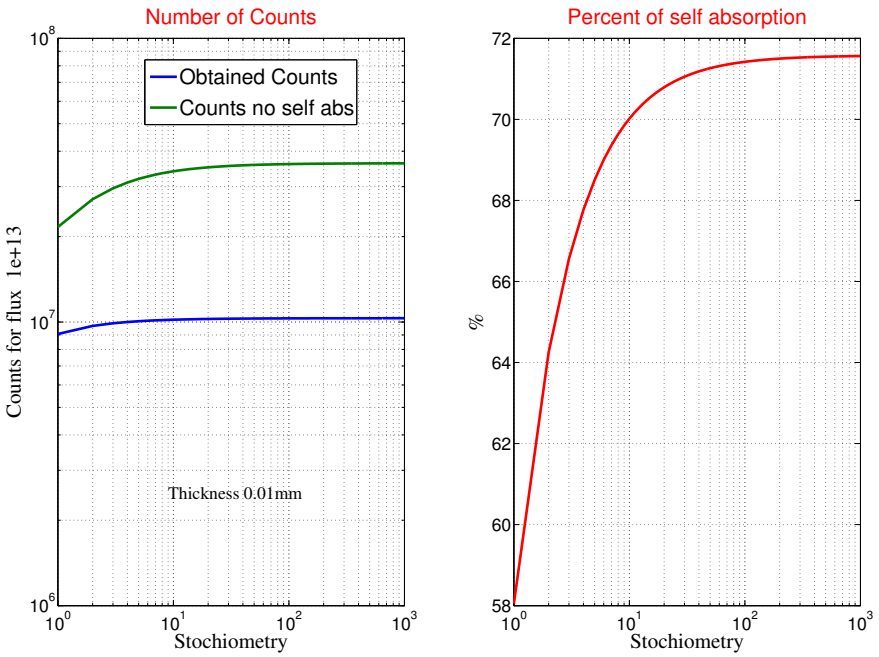

Figure 3.16: Self-absorption estimation on titanium K edge with a variable stoichiometry from Ti_1O_2 to $Ti_{1000}O_2$, i.e. metallic titanium.

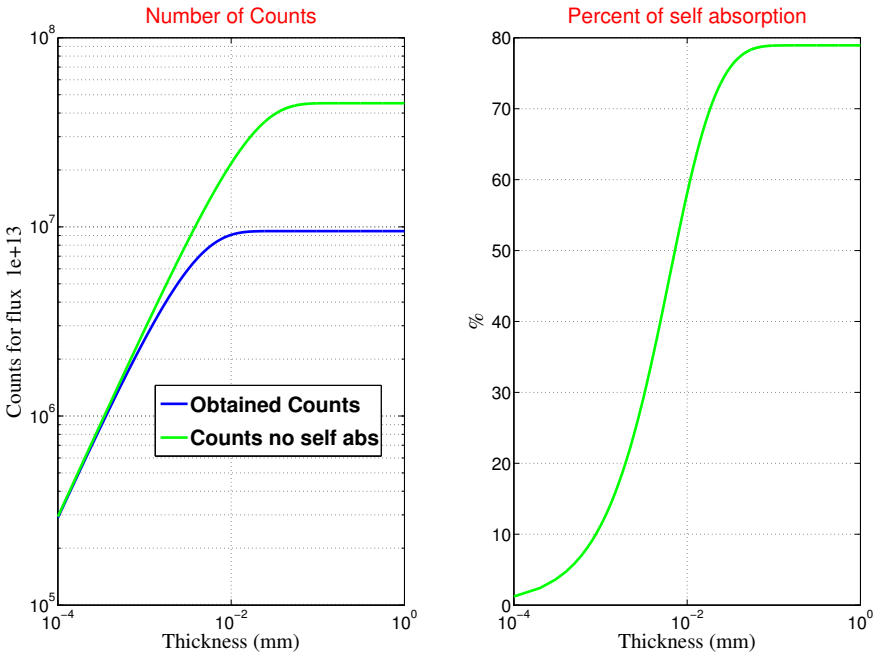

Figure 3.17: Self-absorption estimation on titanium K edge with a variable thickness of the sample.

3.5 Examples and comparison to real data

3.5.1 CIGS solar cells

Copper Indium Gallium Selenide (CIGS) is a compound used as light absorber material in new generation solar cells [62]. It is a tetrahedrally bonded semiconductor, with chalcopyrite crystal structure and with stoichiometry $CuIn_xGa_{1-x}Se_2$, where x goes from 0 to 1 and it determines the band gap and thus the electronic properties of the material. CIGS based solar cells were measured at ID26 and EXAFS spectra were collected at the K edge of copper. Data were taken both from the spectrometer, i.e. resolving the emission energy at the K_α line of copper, and from a photodiode, i.e. in total fluorescence detection. Experimental data are shown in Figure 3.18.

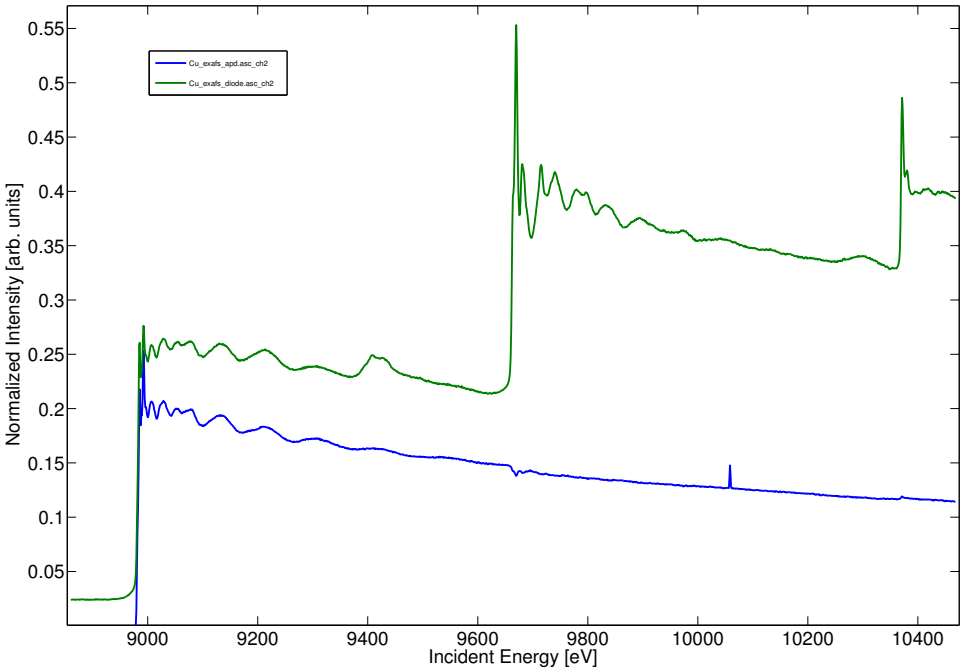

Figure 3.18: EXAFS at the K line of Cu in CIGS solar cells. The characteristic oscillatory structure can be easily noticed. The green line represent the photodiode signal (total fluorescence yield) while the blue line represent the APD signal, resolved in energy on Cu K_α thanks to the spectrometer.

To understand this data, it is useful to analyze the cells' composition. These have a first layer of 0.5 μm conductive glass of aluminum-doped zinc oxide (ZnO) that

works as electrode, a second one of 50 nm cadmium sulfide (CdS) and the third one, where the actual electric carriers are generated, of 1.5 μm thick layer of CIGS. This means that 9 different elements are present in the sample and all of them contribute to the total absorption. Particularly, in the energy range from 8800 to 10500 eV, there are three elements that present an absorption edge: obviously copper, but also zinc and gallium. For this reason, the total fluorescence yield presents three edges at the characteristic energies of 8979 eV (Copper), 9659 eV (Zinc) and 10367 eV (Gallium), which means that all these three elements are giving a contribution to the expected counts on the photodiode, since this typology of detector does not make any photon energy discrimination on the fluorescence it detects. Actually, even other elements with no edges in this range are contributing, as can be seen from the non-zero signal before the copper edge. Concerning the APD signal, instead, it can be noted that when the energy reaches the zinc edge the signal shows a dip. The explanation once again is that zinc is absorbing incident photons, but its fluorescence is not detected by the spectrometer because the Bragg's relation is not fulfilled at zinc's emission lines energy. Thus, the number of photons that can be absorbed by copper atoms decreases and the same does the detected signal. Therefore, we would expect a similar behavior from the signal when it reaches the gallium edge. Surprisingly, instead, a close look at the spectra reveals a small increase in the counts, which means that a small portion of the photons absorbed by gallium are transformed into fluorescence which is able to leak into the useful signal. In fact, during the experiment it was used a silicon Bragg crystal with reflection on the (111) plane (inter-planar distance $d = 3.1356\,\mathring{A}$). For this crystal, the Bragg relation (eq.2.19) is valid at the copper K_α line, which has an energy of 8046.3 eV, for $n = 4$ and a Bragg angle of 79.38°. On the other hand, for the same angle and with the same crystal, $n = 5$ leads to an energy of 10056.3 eV, which is potentially close enough to gallium K_β energy of 10267 eV to allow a few percent of these photons to reach the detector. X-count can be used to model this experiment. Counts were estimated for a uniform sample of Zn, O, Al, Cd, S, Cu, Ga, In, Se with 2.05 μm thickness and density of $5.63\,g/cm^3$ [63]. Of course, real samples have a layer structure which cannot be introduced in the simulation, but since the first two layers have a small thickness with respect to the third one

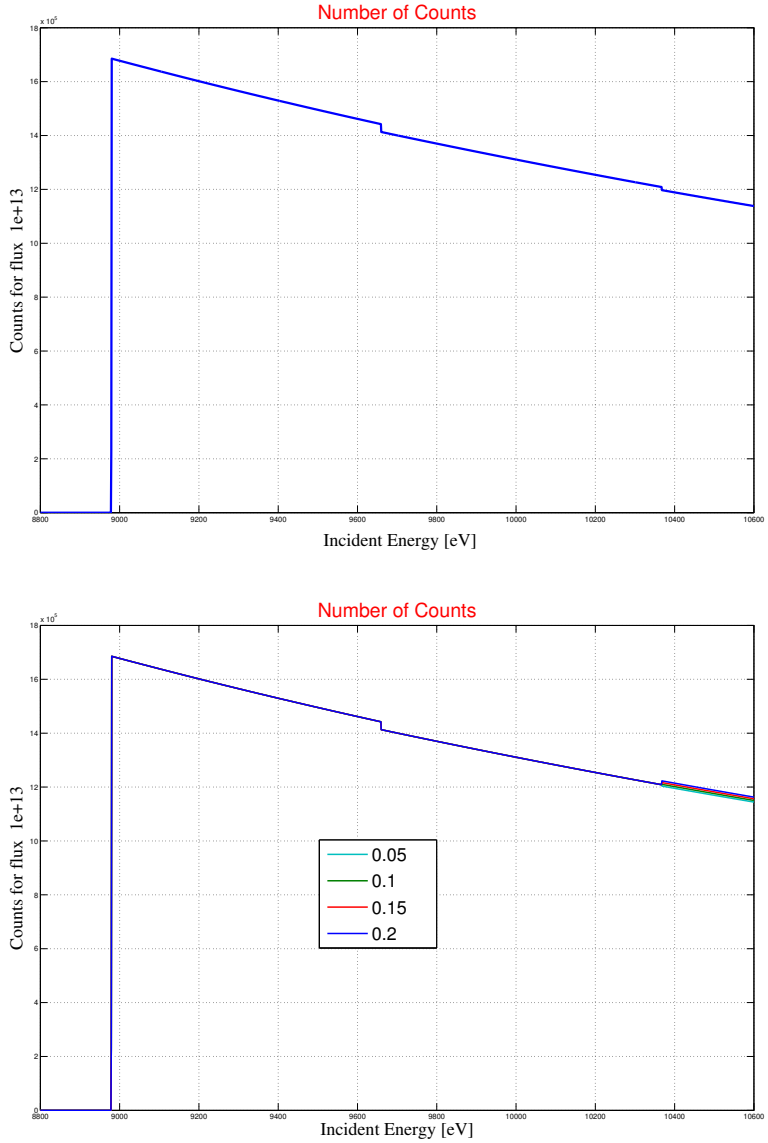

Figure 3.19: Left:Copper K edge in CIGS with no corrections. Emission on K_α line. Right: Copper K edge in CIGS with corrections for gallium K_β emission from 5 to 20%. Copper emission on K_α line.

(500 and 50 nm, compared to 1.5 μm), the results can be compared (obviously, the layers' order is important, since if the ZnO was not on top of the cell it would not receive any photon and thus it would not cause any dip). Figure 3.19(top) shows the expected counts with no correction included. Figure 3.19(bottom), instead, includes a correction from gallium K_β counts, with a percentage of leaking photons from 5 to 20%. Figure 3.20, finally, shows on the same plot the total fluorescence yield and the 15% corrected APD spectra. This last result can be compared with Figure 3.18 and

it is in good agreement with it.

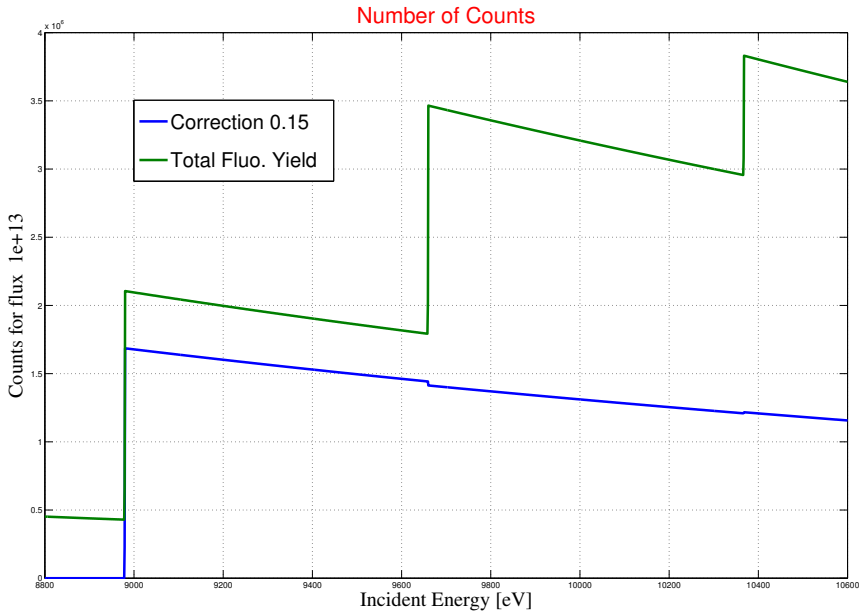

Figure 3.20: Total fluorescence yield (green) and APD signal (blue) simulated at K edge of Cu, with a 15% correction from the counts coming from gallium. This simulation explains the experimental data of Figure 3.18.

3.5.2 Mn_4Ca clusters in photosynthetic systems

Photosynthesis is one of the most important processes that sustain life on earth. In the last few years[64], in literature has been underlined the role of the Mn_4Ca cluster within the photosystem named PS II because of its catalytic effect for water oxidation into the thylakoid membrane of plants and algae. Particularly, EXAFS has been exploited to study Mn-Ca and Mn-Mn distances, whom precise determination is fundamental to fully resolve detailed structures[64, 65]. The main problem present in the EXAFS data analysis is the presence of iron in PS II, with a concentration about 12 times that of manganese. Thus, the iron edge results in a step in the spectrum (Figure 3.21) when the resolution of the detector is low (solid state detectors) and the EXAFS range must stop before it, which means a lower precision in the determination of interatomic distances. Indeed, typically the resolution of EXAFS experiment is $\Delta R = 2\pi/k_{max}$ where k_{max} is the maximum momentum of the pho-

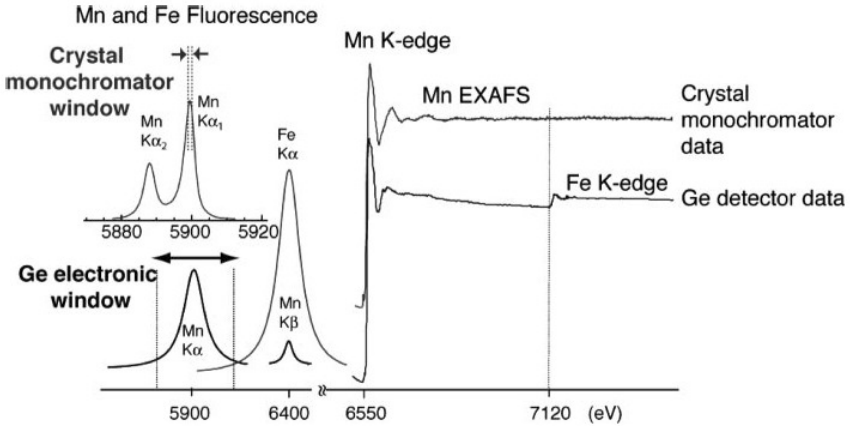

Figure 3.21: EXAFS data for Mn_4Ca clusters and position of emission lines of Mn and Fe[65]. Mn concentration in the measurements was about 1mM.

toelectron, proportional to the energy range. A good solution to eliminate such a step is a high resolution spectrometer, which enables to eliminate the whole contribution from the iron emission line. However, such a solution creates a dip in the spectrum, which is equally problematic for data analysis. Figure 3.22 shows how to eliminate the problem either by the choice of an appropriate thickness or by diluting sufficiently the sample. This way, thanks to the contribution of the exponential term in eq.3.1, no dip or step appears at the iron K edge and EXAFS analysis can reach an higher resolution. E.g. if we want the dip to be 1% or less of the edge jump, we can use Figure 3.23, where the ratio between the depth of the iron dip and the manganese edge jump is showed as a function of the concentration (ratio between water molecules and Mn atoms), to notice that this corresponds to a ratio of at least 20000. Using X-count, one can observe that with a concentration of 2.77 mMol of Mn in water, there are $3.35 \cdot 10^{22}\, atoms/cm^3$ of solvent and $1.67 \cdot 10^{18}\, atoms/cm^3$, i.e this is an estimation of the maximum concentration one can use for the dip to be small enough not to influence EXAFS spectra significantly. Indeed, data in Figure 3.21 were acquired with a concentration of Mn that was about 1mM and, as expected, the dip is not noticeable.

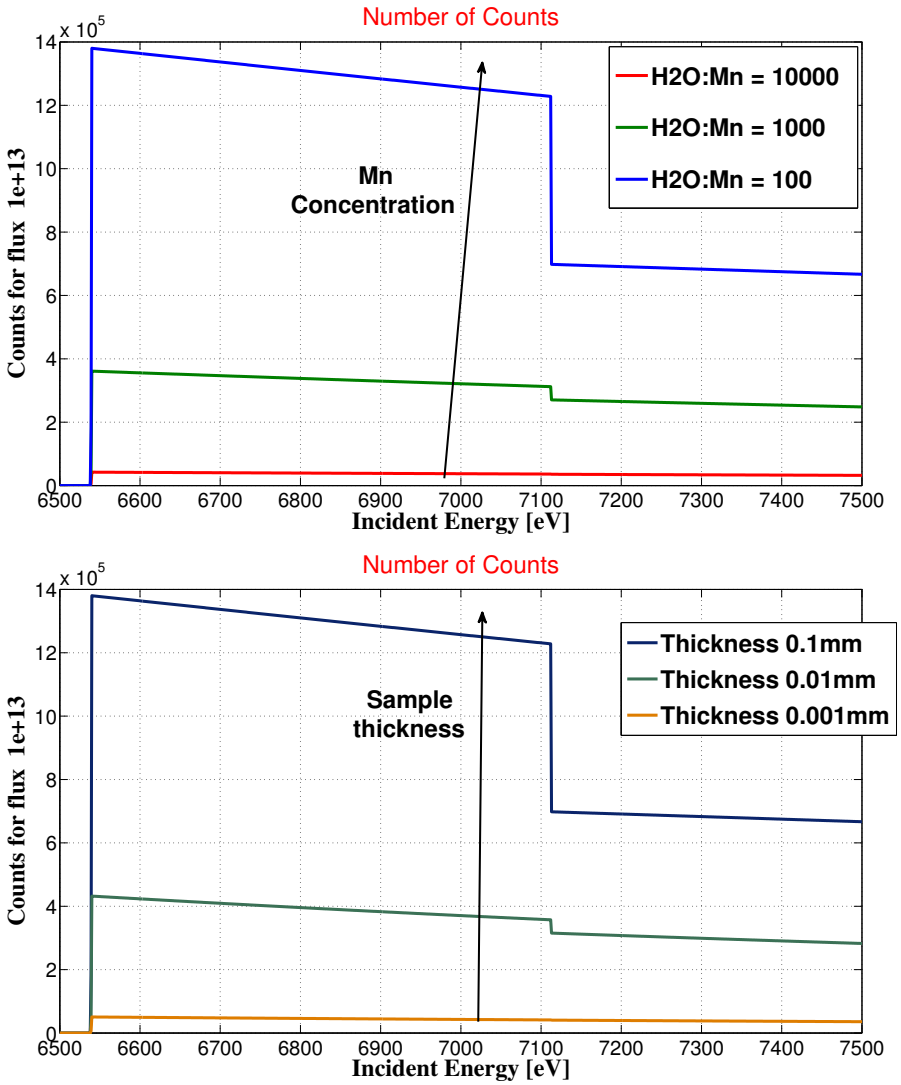

Figure 3.22: Simulated behavior of the EXAFS spectrum on Mn_4Ca clusters in water with presence of iron. Dependence on concentration (ratio between water molecules and manganese atoms) on the top and on the sample thickness on the bottom.

3.6 Conclusions

In this chapter the software X-count was described. Its main goal is the estimation of the useful signal (counts) that one can obtain from a photon-in photon-out experiment. The program gives useful qualitative indications and it can be also used for quantitative measures, if one performs comparative measurements before. Besides from this aspect of evaluation of feasibility, it was shown how the program can faithfully reproduce the behavior of complex samples, like CIGS cells, and how it can be used to estimate the concentration/thickness parameters that one should use to

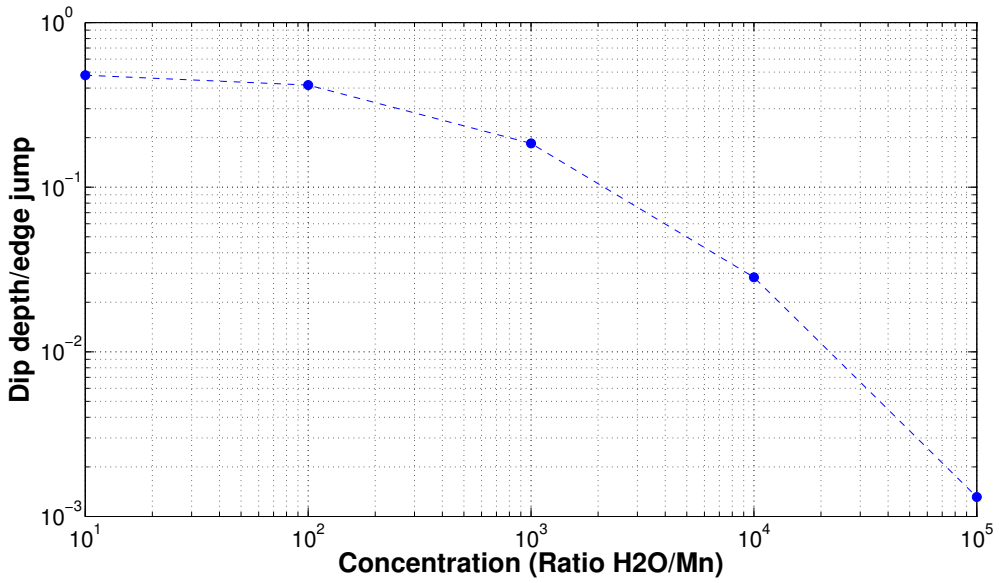

Figure 3.23: Dependence of the dip depth (normalized to the edge jump) on the absorber concentration. As a rule of thumb, a ratio between H_2O and Mn of 10^3 corresponds to 50 mMol, a ratio of 10^4 to 5 mMol and so on.

perform EXAFS experiments without the influence of the edge of other elements in the sample. At the moment, this seems one of the most important practical applications. Furthermore, self absorption estimation is a handy tool since this effect is the main limiting factor in fluorescence detected XAS and therefore it is useful to know whether a spectra will need a correction or not. Finally, it is noteworthy that the software could be improved in many ways in the future; e.g. in principle if one had the cross sections, it would be easy to extend it to the soft x-ray regime.

Chapter 4

TiO_2 and its applications

In the following titanium dioxide will be introduced, from its history to its morphological and electronic properties. Particular emphasis will be given to its application which is wide for commercial and industrial employment, but it also has a great scientific interest which spreads to the fields of catalysis and photovoltaic. The latter has a particular interest to this thesis and thus the Grätzel cell is described, namely the device that exploits TiO_2 as a photoanode to realize a solar cell. Finally, Pulsed Laser Deposition is introduced as a possible technique to realize nanostructured samples with a morphology that resembles that one of a forest, thus maximizing the surface to volume ratio which is a key factor to improve cells' efficiency. This approach was applied to the samples which are the main characters of this thesis, as will be explained in the next chapter.

4.1 History of TiO_2

Titanium is a chemical element with the symbol Ti and atomic number 22. It is the world's fourth most abundant metal and the ninth most abundant element (constituting about 0.63% of the Earth's crust). Titanium was discovered in England by William Gregor in 1791 and named by Martin Heinrich Klaproth for the Titans of Greek mythology. It occurs primarily in minerals like rutile, ilmenite, leucoxene, anatase, brookite, perovskite, and sphene, and it is found in titanates and many iron ores. Ilmenite, also called titanic iron ore, is a weakly magnetic iron-black or

steel-grey mineral found in metamorphic and plutonic rocks. It is used as a source of titanium metal, which appears as a light, strong, lustrous, corrosion-resistant transition metal with a grayish color.
Besides, titanium tends to oxidize and rutile is the most stable form of titanium dioxide and its major ore was discovered in 1803 by Werner in Spain[11]. Its name is derived from the Latin "rutilus", red, in reference to the deep red color observed in some specimen when the transmitted light is viewed. Another phase of TiO_2 is anatase, earlier called octahedrite, which was named by R.J. Hauy in 1801 from the Greek word "anatasis" meaning "extension", due to its longer vertical axis compared to that of rutile. It is associated with rock crystal, feldspar, and axinite in crevices in granite, and mica schist in Dauphiné (France) or to the walls of crevices in the gneisses of the swiss alps. However titanium dioxide is rarely extracted directly from the mineral form; it is rather produced via chemical purification and conversion from titanium tetrachloride.

Today, titanium dioxide pigment is by far the most important material used by the paints and plastics industry (4 million tons annually) for whiteness and opacity. These unique properties are derived from its refractive index ($n = 2.5 - 2.6$), in which it is surpassed only by a few other materials. This semiconductor oxide is in fact the most diffused white pigment, which finds application from paints to sunscreens to food coloring. It has received a great deal of attention due to its chemical stability, non-toxicity, low cost, and other advantageous properties. Another result of its high refractive index is that it is also used as anti-reflection coating in silicon solar cells and in many thin-film optical devices. Besides, due to its hemocompatibility with the human body, TiO_2 is used as a biomaterial (as bone substituent and reinforcing mechanical supports)[11].

Within its other application, titanium dioxide is widely studied in scientific literature because of its demonstrated use as a photo-catalyst under ultraviolet light and as a photocathode for solar cell applications. These last two application, in particular, will be discussed in the following.

Figure 4.1: TiO_2 powder (left) and crystals (right). Both from[11].

4.2 TiO_2 structure

Titanium dioxide occurs in nature as a mineral in three main crystallographic phases, namely rutile, anatase and brookite, and additionally as two high pressure forms, a monoclinic baddeleyite-like form and an orthorhombic $\alpha - PbO_2-$like form, both found recently at the Ries crater in Bavaria. The most common form is rutile, which is also the equilibrium phase at all temperatures. The metastable anatase and brookite phases both convert to rutile upon heating. Rutile, anatase and brookite all contain six-coordinated titanium, which means titanium has basically an octahedral symmetry.

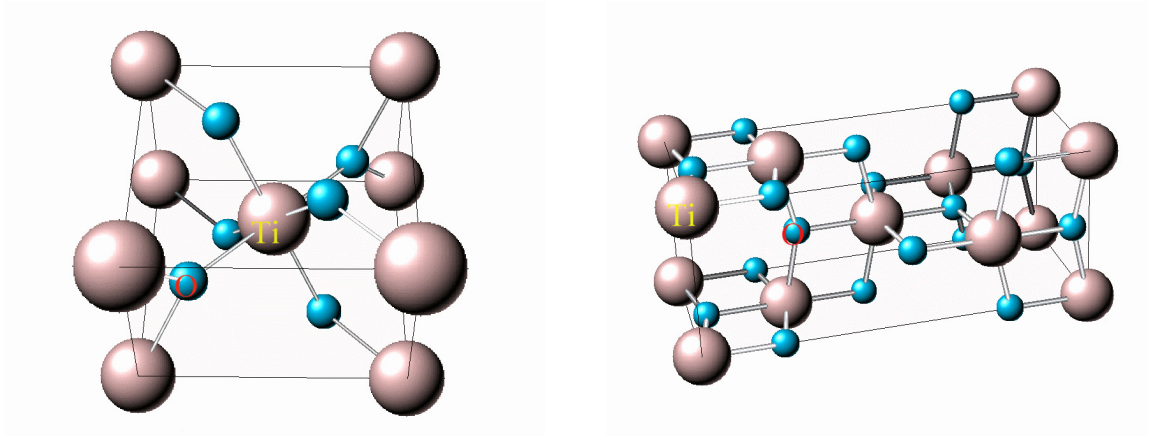

Figure 4.2: Left: Rutile phase of Titanium dioxide. Right: anatase phase[66].

A more detailed look at the structure of the two former phases (showed in Figure 4.2), which are the most important for practical applications, reveals that both ru-

tile and anatase have a tetragonal crystal system (one of the 7 lattice point groups[51]), containing six atoms per unit cell in the first case and twelve in the second one. As already mentioned, in both structures each titanium is coordinated to six oxygen atoms and each oxygen to three titanium atoms. The Ti-Ti distances in anatase are greater (3.79 and 3.04 Å against 3.57 and 2.96 Å in rutile) whereas the Ti-O distances are shorter than in rutile (1.934 and 1.980 Å in anatase against 1.949 and 1.980 Å in rutile). Even if the overall structure is octahedral, in each case it is distorted, two Ti-O distances being slightly greater (with a difference of less than 0.1 Å) than the other four and some or all the O-Ti-O angles deviating from 90°. This distortion is slight in rutile, while it is greater in anatase. This lowers the local point group symmetry of the titanium atom from O_h to D_{2h} and D_{2d} in rutile and anatase, respectively. This is the essential difference between the two phases, together with the secondary coordination and with the fact that in rutile two edges are shared between different TiO_6 octahedra, while in anatase four[67]. As a consequence, the lowest unoccupied molecular orbitals show a different splitting in the 2 cases. As can be seen in Figure 4.3, levels t_{2g} and e_g are not degenerate any more; the second one splits in two levels both for anatase and rutile, while the first one splits in two levels (e and b_1) for anatase and in three levels for rutile (b_{2g}, a_g and b_{3g}). The energy diagram of Figure 4.3 is useful to explain the main features appearing in XANES spectra at the K edge of titanium in TiO_2, which is shown below (Figure 4.4 [69]).

These XANES measurements are rather useful because they allow to understand the electronic structure of the bands of TiO_2 that are closer to the Fermi level, above all thanks to the pre-edge region where many different peaks are labeled. The assignment of these to their respective transition was not an easy task and it has been debated for a long time. Brydson et al.[69], who performed the experiments showed below, used one-electron multiple-scattering calculations, considering only dipole transitions, to explain their measurements, but the peak correspondences were not always satisfactory (most of all the intensity of the peaks). Later on, Wu et al.[68] and Uozomi et al.[70] (further discussions can be found in [71, 72]) performed calculations as well on TiO_2, trying to reproduce the experimental features with different theoretical approaches, with good agreement between their results. Their

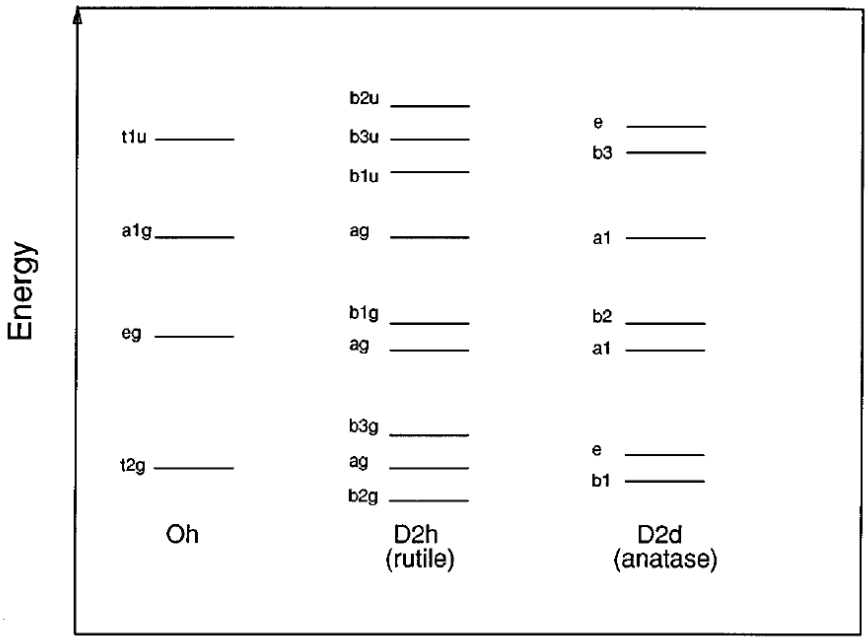

Figure 4.3: Schematic energy diagram of the lowest unoccupied molecular orbitals of a $[TiO_6]^{8-}$ cluster for an ideal octahedral symmetry (left) and for distorted symmetries of rutile (centre) and anatase (right)[68]. It is important to underline that the contribution of neighboring Ti shells is not taken into account here.

conclusions can be summarized as follows:

- Peak A3 and B correspond to the $1s$ transition into the e_g band and $a_1 - a_g$ level, respectively. Both the transitions have a dominant dipolar nature. This is possible, although these bands have mainly $3d$ or $4s$ nature, because they also show a contribution from the oxygen $2p$ levels (and an hybridization of $3d$ and $4p$ levels). A3 shows also a small quadrupole contribution.

- Peak A2 is a shoulder of A3 and it also originates from a transition to e_g band; it is only present in the anatase phase, reflecting the contribution from the two neighboring Ti subshells. These are shown[68] to determine a different degree of hybridization with the central Ti $4p$ orbitals due to the different distance of the two Ti shells.

- Peak A1 is due to a quadrupole transition $1s - t_{2g}$ band. To describe its position in a satisfactory manner, Uozomi et al.[70] had to introduce the effect of the

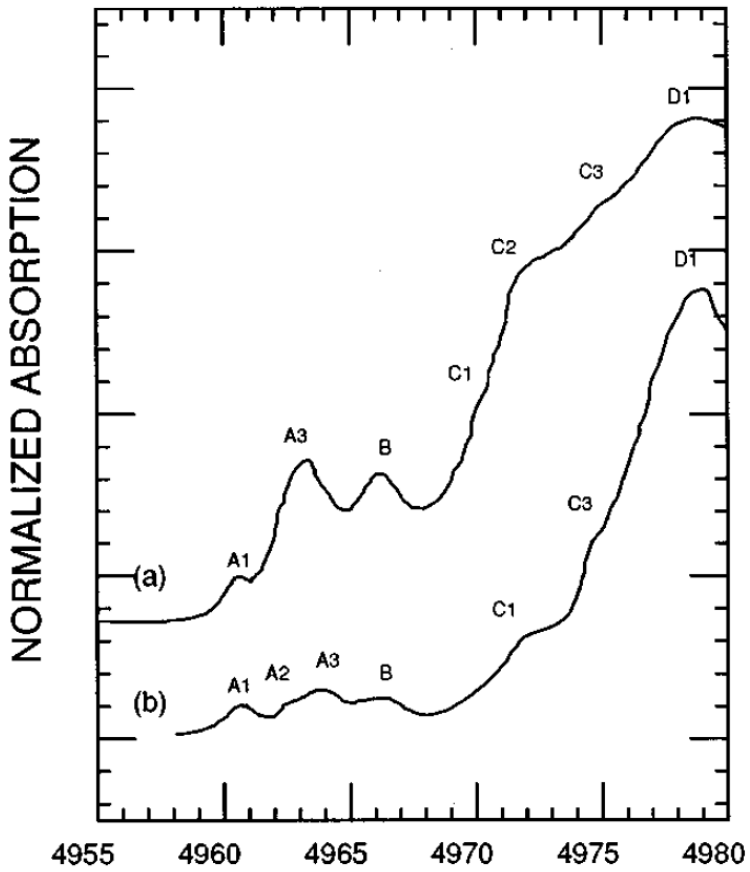

Figure 4.4: Experimental K edge of titanium for rutile (a) and anatase (b) from [69]. Energies on the x-axis suffer an 8eV offset.

core hole on the $3d$ Ti states in the final states of the XAS process.

- Peaks C1, C2 and C3 are transition from $1s$ to b_{1u},b_{2u} and b_{3u} in rutile phase, while peaks labeled C1 and C3 are transitions from $1s$ to e and b_3 levels in the anatase phase. All these levels have mainly p contribution, so that the transitions are dipolar.

- Finally, the main peak D1 is associated with electronic transitions to higher-lying p states.

Higher quality image of the pre-edge of anatase, together with the relative RIXS map, can be found in [34] and it is reported in Figure 4.5.

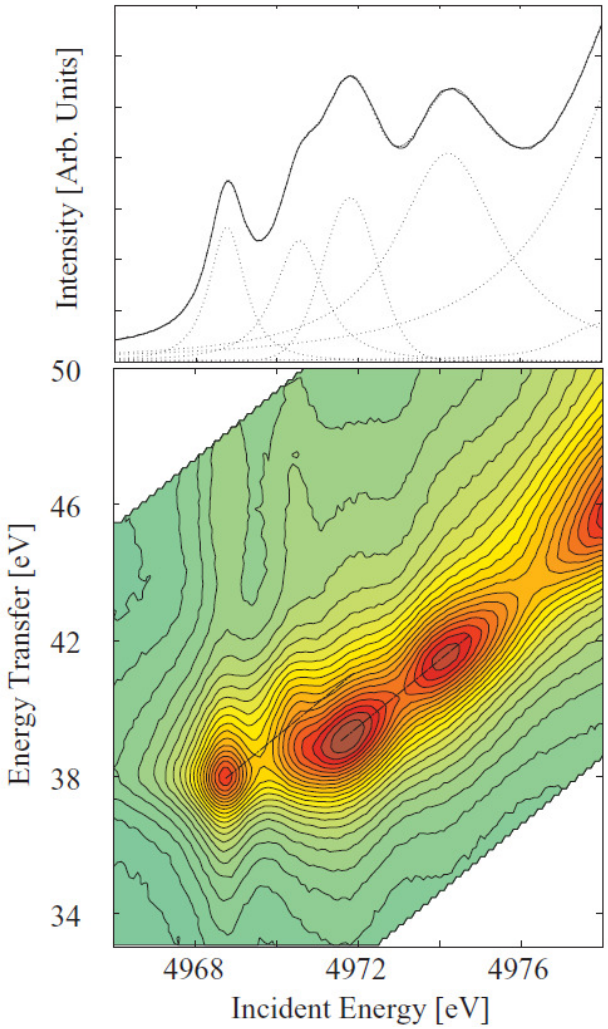

Figure 4.5: High resolution pre-edge and RIXS map of anatase TiO_2 in the region of peaks A1,A2,A3 and B [34].

4.3 Application of TiO_2 in photovoltaics and catalysis

TiO_2 is characterized by the presence of photo-induced phenomena, riassumed in Figure 4.6 [73]. They take advantage from the semiconductor band gap (3 eV for rutile and 3.2 eV for anatase); in fact, when photons have a higher energy than this band gap, they can be absorbed and an electron is promoted to the conduction band, leaving a hole in the valence band. This excited electron can either be used directly to create electricity in photovoltaic solar cells or drive a chemical reaction, process which is called photocatalysis. Also, a special phenomenon was recently discovered:

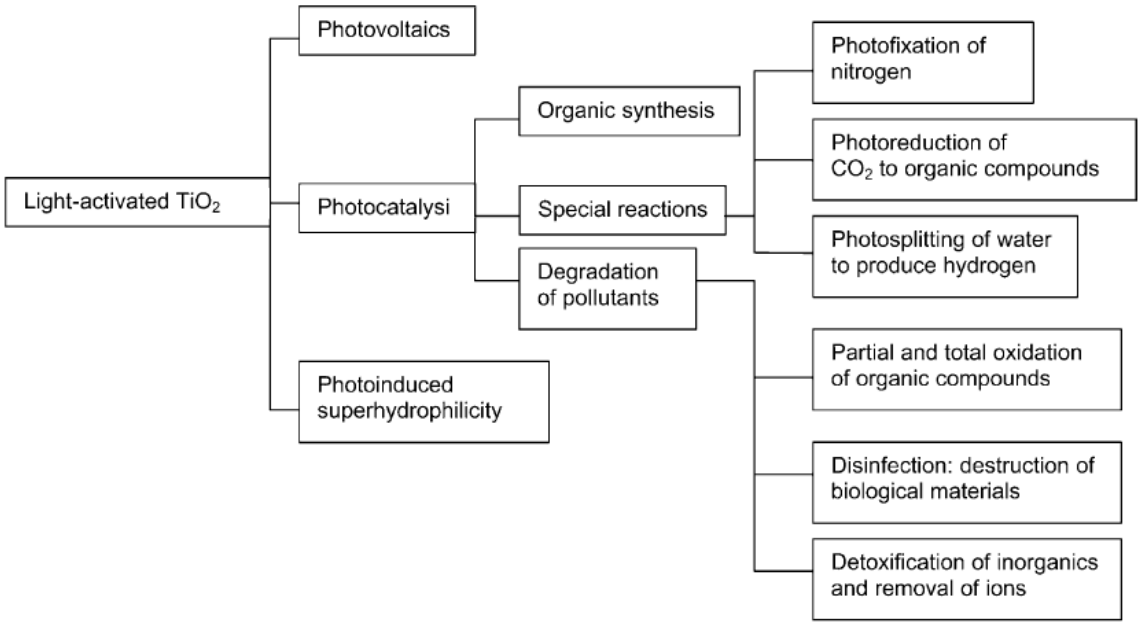

Figure 4.6: Applications of TiO_2 based on its interaction with light[73].

trapping of holes at the TiO_2 surface causes a high wettability and is termed "photoinduced superhydrophilicity" (PSH) [74]. All photo-induced phenomena involve surface bound redox reactions. Nowadays, TiO_2 mediated photocatalytic reactions are gaining more and more importance (this is reflected in the huge number of publications on this topic; a review is [4]) and the term is used to group a really wide range of applications. Within these, an important place is occupied by the splitting of water to produce hydrogen. In 1972 the first photoelectrochemical cell for water splitting ($2H_2O \Rightarrow 2H_2 + O_2$) was reported by Fujishima and Honda[75] using a rutile TiO_2 photoanode and Pt counter electrode. However, the most active field of TiO_2 photocatalysis is by far the photo-degeneration of organic compounds. It has become a photocatalyst in environmental decontamination for a large variety of organics, viruses, bacteria, fungi, algae, and even cancer cells, which can be totally degraded and mineralized to CO_2, H_2O, and harmless inorganic anions. This performance is attributed to highly oxidizing holes and hydroxyl radicals that are known as indiscriminate oxidizing agents.

Concerning photovoltaic applications, instead, the properties of TiO_2 were exploited in 1991 by O'Regan and Grätzel[76], who reported about an efficient solar

cell working with an electrode constituted by nano-sized TiO_2 particles. From this first article on, the technique was developed and more and more efficient cells were built[77]. They are grouped under the name of dye sensitized solar cells (or Grätzel cells) and they will be described in the following.

4.4 The Grätzel cell

The current technology of solar cells is mainly based on the properties of solid-state material p-n junctions between a n-doped crystal and a p-doped one: indeed, such a structure generates a barrier of potential across the junction (about 0.7 eV in silicon) as a consequence of the equalization of the Fermi levels on the two sides and thus it originates an electric field in the region. For this reason, when the cell is exposed to sunlight, the photons with energy higher than the band gap (1.1 eV for silicon, which means that almost all the visible and ultraviolet spectrum are absorbed) are able to generate electron-hole pairs, which are subsequently separated by the electric field and can travel to the electrodes. Finally, they flow through an external load to generate electricity and the circuit is closed when they arrive on the other side of the junction and recombine.

Nowadays, the most used material for solar cells application is silicon, either in amorphous, poly-crystalline of perfect crystal phase, which could exploit the great experience achieved in the development of electronics industry. The efficiency of silicon solar cells is theoretically limited by the Shockley-Quassier limit[78] ($\sim 30\%$) and efficiencies up to 25% has been practically realized (although commercial solar cells do not usually exceed 10-15%). Many other materials have been investigated, like III/V semiconductors (for example GaAs) which can provide even higher efficiencies (up to 43.5% for layered structures of different semiconductors) but they are mainly used for aerospace applications, since their cost is definitely high, or copper-indium-gallium-selenide (CIGS) solar cells[62], with efficiencies up to 20%.

An interesting alternative to solid state devices is represented by hybrid cells, i.e. a junction between a solid semiconductor electrode and a liquid electrolyte, thereby forming a photoelectrochemical device[6]. An example of such a device is a Dye Sen-

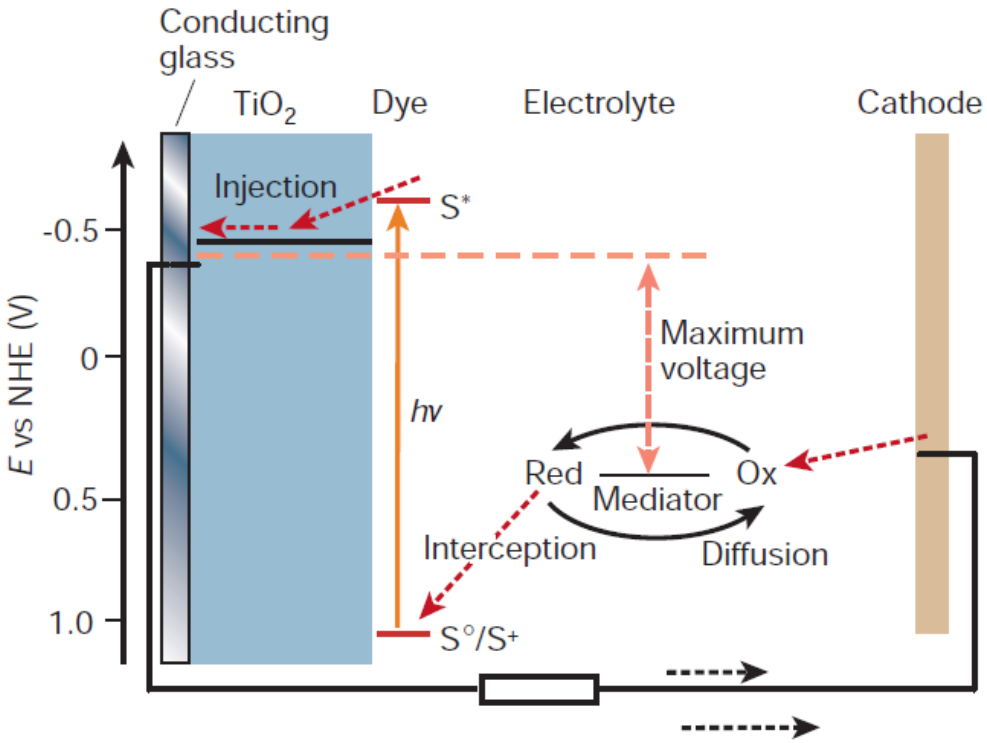

Figure 4.7: Scheme of the functioning of a Grätzel cell[5].

sitized Solar Cell (DSSC) or Grätzel cell, whose structure is shown in Figure 4.7. Here, the two tasks of absorbing the incoming photons and transporting the excited electrons are carried out by two different parts of the cell. Indeed, a semiconductor electrode (generally a photoanode) of mesoporous TiO_2 is wetted (or, better, sensitized) with a molecule which strongly absorbs light. This is usually a dye with a broad absorption band in the visible range and it provides the photons absorption and the electron promotion in the LUMO orbitals. Since these dyes are chosen in such a way that their LUMO orbitals match the energy of the conduction band of the TiO_2 being slightly greater than it, this excited electron finds energetically favorable to migrate into the conduction band of the semiconductor and travels through it, reaching the external circuit. The circuit is closed by a transparent cathode (where the light also enters the cell) where the electron incur a redox reaction with the electrolyte and recombinates with the holes left in the HOMO orbital of the dye. The electrolyte is usually an organic solvent containing a redox system, such as the iodide/triiodide couple. The voltage generated from a DSSC cell under illumination corresponds to

the difference between the quasi-Fermi level of the semiconductor conduction band and the redox potential of the electrolyte. Overall, the device generates electric power from light without suffering any permanent chemical transformation[5].

The porosity of the material in the anode, which is in contact with the dye, is an important factor because it determines the efficiency of the electron transfer between the two. Indeed, the absorption of light by a monolayer of dye is weak because the area occupied by one molecule is much larger than its cross section for light capture. Thus, it is important to maximize the contact surface between the two, which means to maximize the surface-to-volume ratio on the semiconductor. Figure 4.8 shows the structure of a nanocrystalline semiconductor oxide electrode used nowadays in DSSC. Nanoparticles of the oxide are deposited, for example, by screen printing onto a glass or flexible plastic support covered with a transparent conducting layer of fluorine-doped tin dioxide (FTO) or tin-doped indium oxide (ITO). Each particle is coated with a monolayer of sensitizer. Typically, the anatase nanoparticles are prepared with a hydrothermal method. They exhibit predominantly a bi-pyramidal shape, with the exposed facets having (101) orientation, which is the lowest energy surface of anatase. Their average size is 20 nm. A short sintering process is usually applied to ensure that the particles are electronically interconnected.

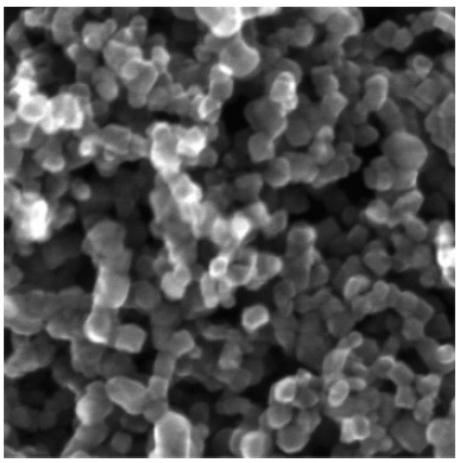

Figure 4.8: STM image of a sintered mesoscopic TiO_2 film. Here, the average particle size is 20 nm[5].

Concerning the dye sensitizers, molecular engineering focused lately on the study of ruthenium-based molecules, which show an excellent stability (e.g. it respects

the requirement to work for about 20 years without any loss of performances). Figure 4.9 illustrates the cis-Di-(thiocyanato) bis(2,2'-bipyridyl)-(4,4'-dicarboxylate) ruthenium-(II) complex, coded as N3 or N-719 dye depending on whether it contains four or two protons, which has been for long the most efficient known dye. A few years ago, its performances has been matched by another complex, named "black dye"[9], showed in green in the figure below. Its formula is RuL(NCS)3 with L = 2,2',2"-terpyridyl-4,4',4"-tricarboxylic acid. Both for N3 and black dye, researchers found that the dyes bind with the anatase TiO_2 surface though a carboxyl group binding (COO-) rather than ester binding (C=O)[79, 80]. The carboxylate either

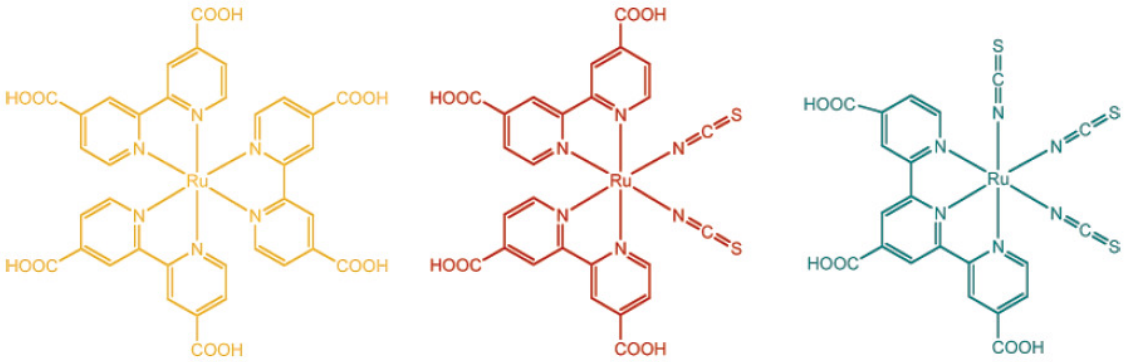

Figure 4.9: Ruthenium-based dye sensitizers. In particular, N3 is showed in red and the black dye in green[5].

bridges two adjacent rows of titanium ions through bidentate coordination or interacts with surface hydroxyl groups through hydrogen bonds. Model studies, using the L ligand of N3 adsorbed onto single-crystal TiO_2 (110) rutile, investigated by means of X-ray photoelectron spectroscopy, X-ray absorption spectroscopy, and quantum chemical calculations[81], are also in favor of the bridging bidentate configuration.

DSSCs reached an efficiency of about 11%, which is a good result but it is not as high as solid state solar cells. Instead, the main advantage of these devices is that they are produced with cheap material and cheap techniques, which allow the efficiency/price ratio to be competitive with the major technologies currently in commerce. Hence, major advantages of this technology are:

- Low fabrication price.

- No hole creation in the semiconductor, only one electron is injected; this result in a low recombination rate of excited electrons.
- High capability to dissipate the heat in excess. This is important because efficiency of solar cells decreases with increasing temperatures.

Of course, there are also some drawbacks. The main one is due to the presence of the liquid electrolyte, which has problems of stability with temperature and can lead to physical damages of the cell.

After the initial introduction of this devices, a lot of research had been developed to overcome their limitations and improve their performances. Mainly, important steps had been done about improving the dye absorption[5], replacing the electrolyte with a gel or solid compound, building tandem cells where the cathode is also sensitized[82] and creating TiO_2 anodes with a large surface-to-volume ratio in order to guarantee high electron transfer. This last field of research has been studied at Politecnico di Milano, where researchers developed new growth techniques to obtain better results, which will be described in the following.

4.5 TiO_2 photoanodes deposited by Pulsed Laser Deposition

As already mentioned, since the dimension of a dye molecule is much greater than its optical cross section, the absorption of light by a monolayer of dye is weak. A respectable photovoltaic efficiency cannot, therefore, be obtained by use of a flat semiconductor surface but rather by use of the porous, nanostructured film of very high surface roughness discussed above. This way, when light penetrates the photosensitized semiconductor, it crosses hundreds of adsorbed dye monolayers. The mesoporous structure thus fulfills a function similar to the thylakoid vesicles in green leaves, which are stacked in order to enhance light harvesting by chlorophyll.

Following this idea, researchers in Politecnico di Milano tried to exploit a different deposition technique to achieve an higher surface-to-volume ratio. Such a technique is

named *Pulsed Laser Deposition (PLD)* [83, 84]. This is a physical vapor deposition, i.e. a method that involves the deposition of a thin film of material through its condensation from a vapor phase onto various surfaces. In PLD (Figure 4.10), in

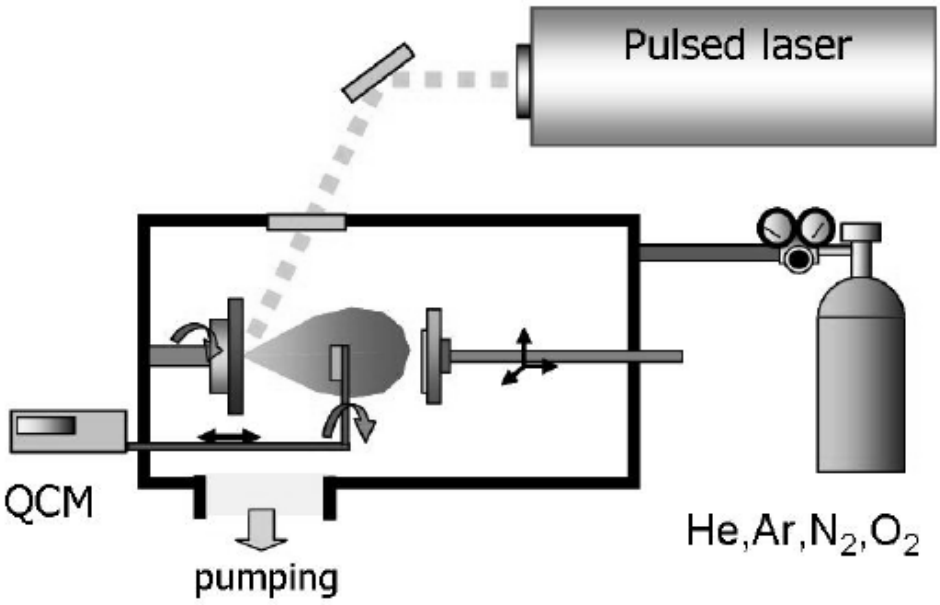

Figure 4.10: PLD apparatus scheme. In particular are shown the laser, the valve to inject various gases and the QCM (quartz crystal microbalance) that allows to observe the deposition rate at different distances from the substrate target[85].

particular, the vaporization is obtained thanks to a high-power pulsed laser beam that strikes the material that has to be deposited; as a consequence of the really high energy that the laser transfers to the material, it reaches the plasma phase in a plume that deposits it on a substrate such as a silicon wafer. The whole process is done in a high vacuum chamber with well controlled conditions of pressure and temperature. In fact, the growth process can be guided by tuning such conditions, together with the laser parameters. Particularly, for the nucleation process it is very important the laser fluence $[J/cm^2]$, energy and pulse duration. The substrate and chamber temperatures are also determinant, together with the background pressure. In case of oxides, for example, although the process happens in ultra-high vacuum, a residual pressure of oxygen is needed both to obtain cluster aggregation as plumes and to ensure stoichiometric transfer from the target to the film.

Di Fonzo et al.[7] applied PLD to the growth of hierarchically organized TiO_2 films. In particular, they describe how proper choices of the deposition parameters can lead from a normal aerogel-like film to a dense forest of distinct hierarchical assembly of ultrafine nanoparticles (even less than 10 nm) with a degree of porosity going from 48% to 90%. Figure 4.11 shows a sample of TiO_2 deposited in atmosphere of 40 Pa after annealing at 400 degrees (a thermal treatment used to increase the crystalline order) where it can be noted the organization at different scales. Such a morphology leads to an extremely high surface to volume ratio, as can be understood by the specific surface area, which is about 100 m^2/g in these samples. Since the tree structure is achieved via aggregation of clusters with a diameter of about 10 nm, as a rule of thumb one can think that the ratio of surface atoms to volume atoms is about 20%, i.e. the ratio calculated for such clusters[86].

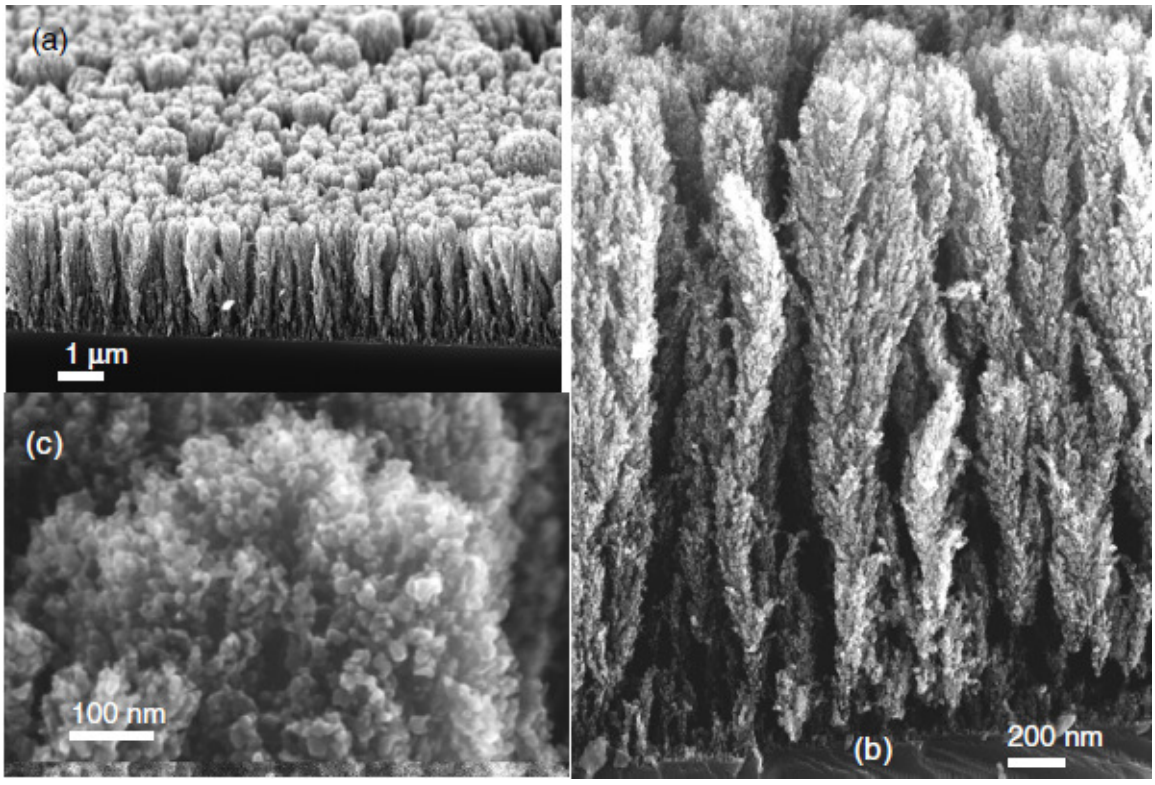

Figure 4.11: SEM images of a TiO_2 sample obtained by PLD at 40 Pa after annealing at 400 degrees. (a) the uniform "forest" like assembly; (b) single "trees"; (c) a "tree" tip [7].

In Fusi et al.[87] the properties of PLD-deposited and subsequently annealed films are studied in order to understand the relation between the oxide morphology and its electronic and crystalline structure. In particular it is shown that thermal treatment

increases the crystalline order while the morphology and the surface roughness are not significantly modified. Raman measurements in this work show how for low pressures (10 Pa) the crystalline phase is anatase, for intermediate pressures (30 Pa) it is still anatase even if small features typical of rutile start to appear, while for higher pressures ($\geq$ 60 Pa) such features are fully visible, indicating the presence of both phases.

Finally, in 2010 TiO_2 hierarchical nanostructures were used as photoanodes in DSSCs[8]. In this work a 4.9% efficiency was achieved with a 7 μm thick film together with C101 dye sensitizer. Detailed analysis demonstrated that this morphology hampers the electron recombination, most of all impairing the electron back reaction with tri-iodide. In particular, electron lifetime can be increased by more than 1 order of magnitude in comparison to the benchmark mesoporous TiO_2 films. This is important because a longer lifetime τ_r means a longer diffusion length L_n, since they are related through the diffusion coefficient D_e via:

$$L_n = \sqrt{D_e \tau_r}. \tag{4.1}$$

In order to achieve a satisfactory collection of charge carriers it must be $L_n > d$, where d is the film thickness. This ensures an high internal-photon-to-electron (IPCE) conversion, which is an important step to reach high conversion efficiencies. These results confirm the interest in such tree-like structures and in their application in DSSCs, although the efficiencies achieved are still rather far from the results obtained in silicon solar cells.

4.6 Conclusions

TiO_2 has been widely studied in the past years thanks to its many properties which make it a good candidate for many industrial and scientific applications. In this chapter it was described the basic structure of titanium dioxide together with a part of the research which has been made on it with synchrotron radiation (to understand the structure of XANES pre-edge measurements on Ti K edge, which is useful to understand the measures showed in the next chapter). The discovery of a device like the Grätzel cell brought even more interest on this semiconductor material because

this constitute an important step in the road to cheaper and greener energy exploitation. For this reason the functioning of the cell was discussed with some detail, particularly regarding the importance of the semiconductor-dye interface. This is a key factor which has to be well understood and engineered to obtain efficient cells. Therefore scientific research faced the problem trying to maximize the surface to volume ratio of the photocatode to have the maximum electron transfer at the interface; one possible approach was described, namely that one used in Politecnico di Milano which employs the PLD technique to create forest-like assemblies of nanoparticles, which allows to obtain an extremely high porosity of the sample. For this reason, the samples studied in this thesis are all deposited with such a technique and, expecting a strong interaction with the dye, their electronic properties can be studied to understand the relevance of the interaction.

Chapter 5

Experimental data and analysis

This final chapter presents the experimental data that were acquired at ID26. First, the two kind of samples are described, namely a nanostructured TiO_2 film grown with PLD and an analogue sample sensitized with "black dye"[9]. Secondly, some details about the experimental setup are given. Finally, the spectra are shown and discussed. These are XANES measurements on the K edge of titanium, XES on the K_β emission line and on its satellites and RIXS measurements on the same energy ranges. The idea behind this measurements was simple: x-ray spectroscopies are powerful tools to determine the electronic structure in the neighborhood of an absorber atom (i.e. Ti). However, photons have a strong penetration length in the sample, so these techniques are mainly sensitive to the bulk and not to the surface, which is the key part of the samples considered here. So if one wants to study how the dye affects the electronic structure, he should perform e.g. XPS (X-ray Photoemission spectroscopy) measures. Indeed this was done in literature[88] with interesting results, although these are not element-selective. For this reason, the measures showed here want to show whether is possible to see differences between the spectra taken on the samples with and without dye, despite the fact that bulk-sensitive techniques are used. This could bring some implications, like e.g. that the interaction between the dye and the semiconductor (and particularly, the titanium atoms) is quite deep and that the number of surface atoms with respect to the volume ones is high and affects the electronic properties of the structure.

5.1 Samples

All the samples considered in this thesis are composed by titanium dioxide. Particularly, the measurements focused on nanostructured layers with thickness of 200 nm, deposited via pulsed laser deposition on a silicon substrate of 1 cm^2. The most important parameters for the deposition comprehend a deposition pressure of 30 Pa in atmosphere of Ar and O_2 (4:1) with a target-substrate distance of 5 cm and, for the laser, 15 ns pulses with $\lambda = 248$ nm and a fluence of 3 J/cm^2. The resulting morphology is very similar to the one showed in Figure 4.11. All the samples were subsequently treated with a thermal annealing procedure which reaches 400 °C and induces a better crystalline phase, as explained in the previous chapter and showed in Figure 5.1. From [7] further informations about the samples can be found. In

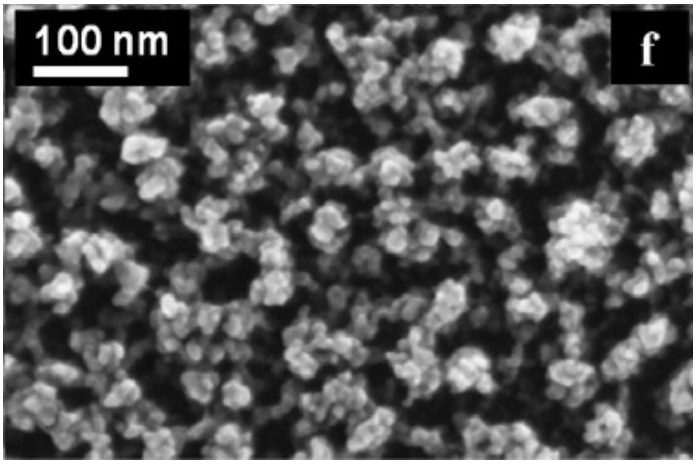

Figure 5.1: SEM image of the TiO_2 nanostructured samples deposited at 30 Pa after annealing at 400 °C [87].

this work, the deposited mass was measured for each sample and thus the density of the samples was estimated to be $\sim 0.4\, g/cm^3$ (against a density of anatase TiO_2 of 3.895 g/cm^3) therefore with a degree of porosity that reaches 90%. Also, analysis of Raman spectra shows an expected crystalline phase which is mainly anatase (anatase to rutile ratio $\sim 95\%$).

The TiO_2 layers were subsequently treated in two different ways: the first one consisted in a bath of "black dye"[9], where the sample was left for 18 hours and subsequently washed with acetonitrile, in order to leave a monolayer of dye attached

on top of the TiO_2 nanostructure. This is a standard technique used to prepare photoanodes for dye sensitized solar cells. For this reason, in the following this sample will be referred to as DYE sample (Figure 5.2). The treatment to the second sample consisted of enclosing it in a quartz cell, where it was subjected to a linear thermal increase up to 150 °C to clean it from impurities and water absorbed from atmosphere and then treated with an oxygen atmosphere to recover the correct stoichiometry. After that, the cell preserved the clean condition of the sample in a vacuum atmosphere until the moment of the measurements. Its cleanliness was checked by analysis of

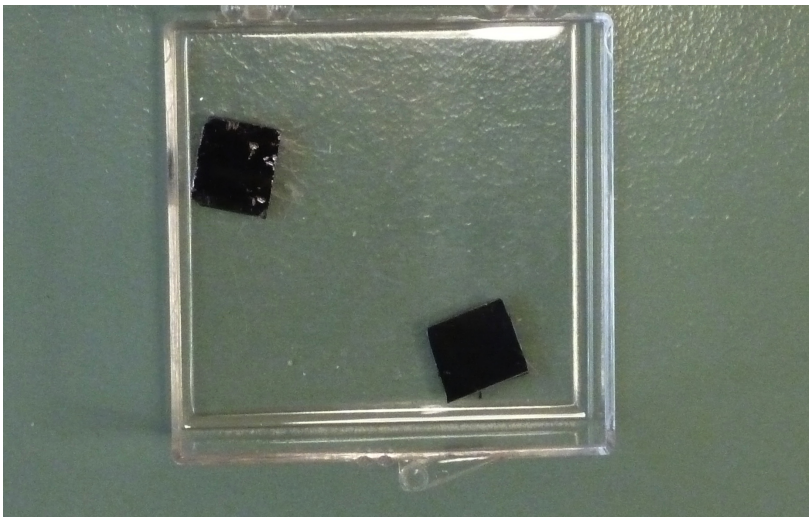

Figure 5.2: DYE samples with the dye sensitizer on top.

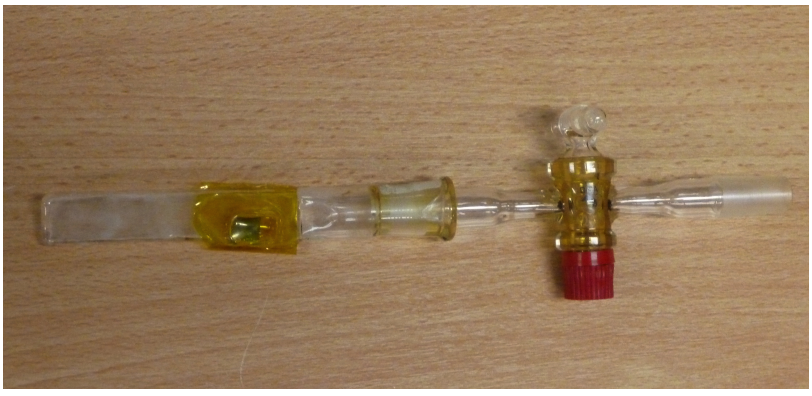

Figure 5.3: DEG sample inside the quartz cell that was keeping it under vacuum.

the IR spectrum, which evidenced no traces of water and good agreement with reference spectra known for TiO_2. In the following, this second sample will be referred

to as degassed or DEG (Figure 5.3). Finally, two pellet of 99.9% anatase TiO_2 were measured as a reference before the measures of each one of the samples.

5.2 Experimental details

Experiments were performed at ID26 within two different beamtimes. Unfortunately, such beamtimes were dedicated to different purposes so that a few changes were made in the setup. Mainly, the DYE sample was measured in March 2011 during a pump and probe dedicated beamtime and for this reason it was used the Si(111) monochromator. Indeed, this can provide very high photon flux at the expense of a resolving power ($E/\Delta E$) of 7000. The DEG sample was instead measured in July 2011 during a beamtime dedicated to catalysis on titanium. Here, a higher resolving power was necessary and thus it was chosen a Si(311) monochromator ($E/\Delta E = 35000$). The wavelength dispersive spectrometer, instead, had the same crystals in both cases. In particular, there were five Germanium(311) crystals. Therefore, the overall spectrometer resolution was calculated with beamline software to be 0.91 eV in the first case and 0.8 eV in the second one. For the DEG sample, the whole cell was mounted on a motorized stage in the correct position on the Rowland circle of the spectrometer and subsequently aligned. For the DYE sample, it was measured in air and therefore it was simply mounted on a holder upon the motorized stage and aligned. Finally, the same APD detector with a voltage of 340V was used to acquire the signal in both cases, together with a photodiode placed close to the samples to measure total fluorescence yields.

The considerations above lead to the conclusion that the DEG sample was measured with a better resolution, considering both the monochromator and the spectrometer, than the DYE sample. An estimation of this different total resolution can be given thanks to beamline software. Such a tool considers all the important mechanisms which determine the peak broadening for measurements of HERFD XAS and RIXS. These are the intermediate and final state core hole lifetime, the incident x-rays resolution, the monochromator resolving power and the spectrometer resolution. Considering these, the different FWHMs of Gaussian and Lorentzian shapes

can be taken into account and their overlap can be calculated. Implementing these calculations, it is possible to estimate the total FWHM expected resolution of the experiment. Here, the result shows a resolution of 0.93 eV for the DEG sample, while for the DYE sample it shows a resolution of 1.3 eV.

5.3 Experimental data

Three experimental techniques were mainly employed to acquire HERFD XANES spectra, XES spectra and the technique that combines the two, namely RIXS maps.

XANES. X-ray absorption near edge structure spectra were acquired around the

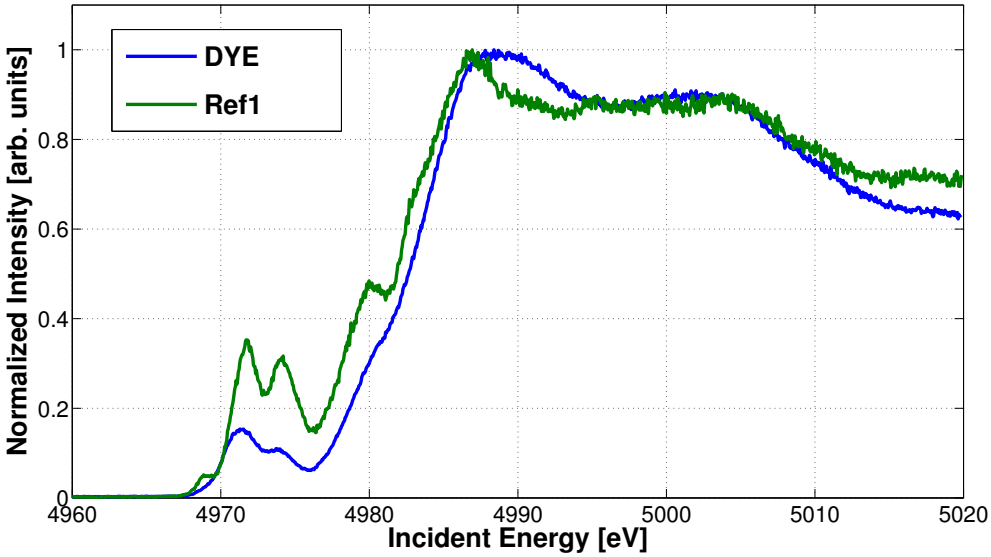

Figure 5.4: XANES spectra of DYE sample compared with reference pellet.

K edge of titanium in a window of about 100 eV. Given the experimental setup, all spectra are High Energy Resolution Fluorescence Detected XANES. This was done for the DYE sample and the DEG sample. For both of them a reference pellet of TiO_2 anatase was also measured in the same beamtime. The results are shown in Figure 5.4, Figure 5.5 and Figure 5.6, normalized in peak at the white line.

XES. X-ray emission spectra were acquired at the $K_{\beta_{1,3}}$ emission line and at its satellites ($K_{\beta_{2,5}}$) at higher energy. It is noteworthy that $K_{\beta_{1,3}}$ represents the transition between 3p and 1s levels of titanium, and it can be interesting because

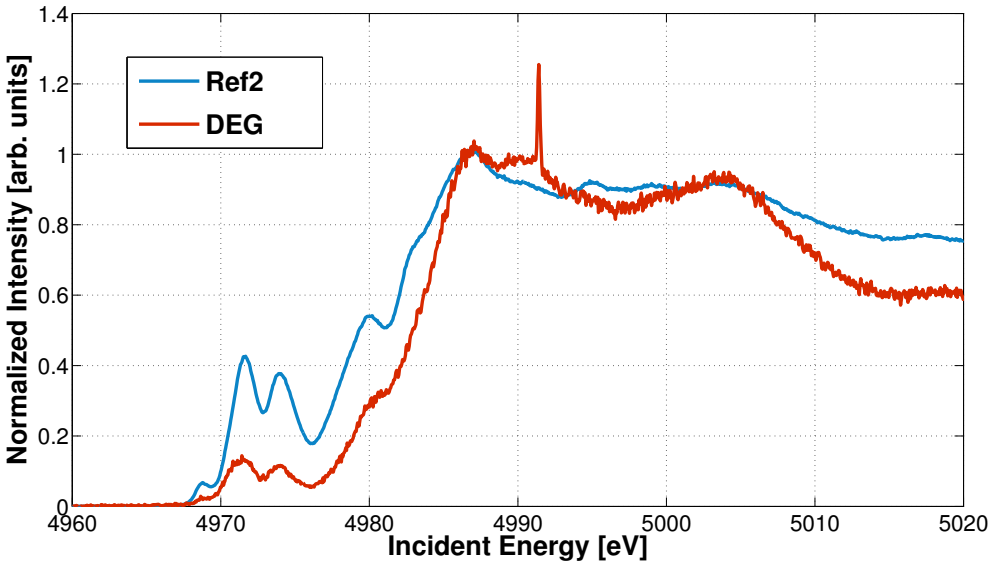

Figure 5.5: XANES spectra of DEG sample compared with reference pellet.

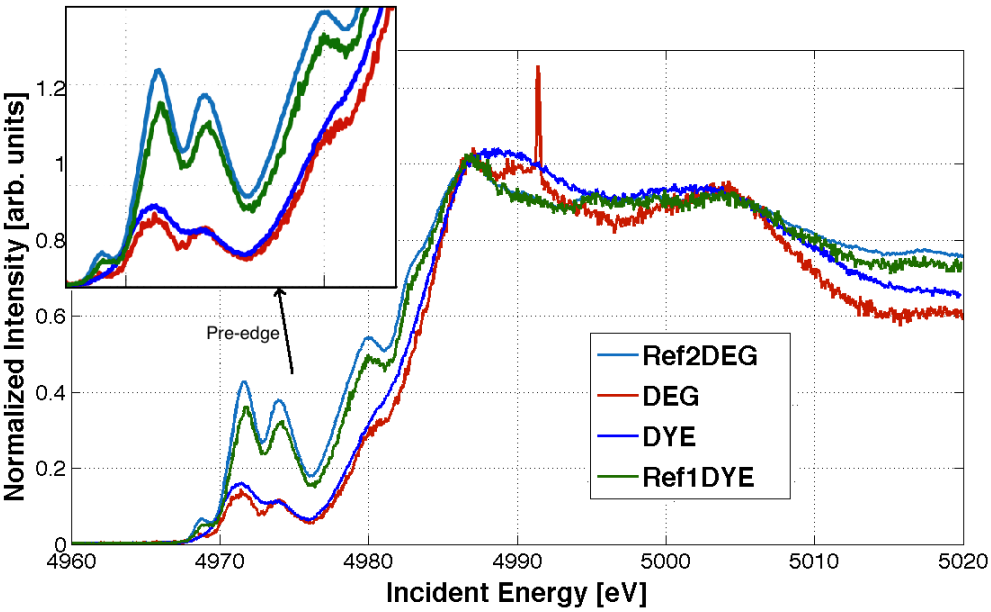

Figure 5.6: All XANES measurements showed with the same normalization on the white line. Zoom on the pre-edge structure is also present.

of its chemical sensitivity (e.g. oxidation state of an ion) while $K_{\beta_{2,5}}$ represents the transitions between the valence band states of the semiconductor and the 1s levels of titanium. Thus, the importance of these lines is that they are sensitive to chemical changes in the valence band as we could expect, e.g., because of the bondings of the dye with the titanium dioxide. During the measurements, DYE and DEG were found

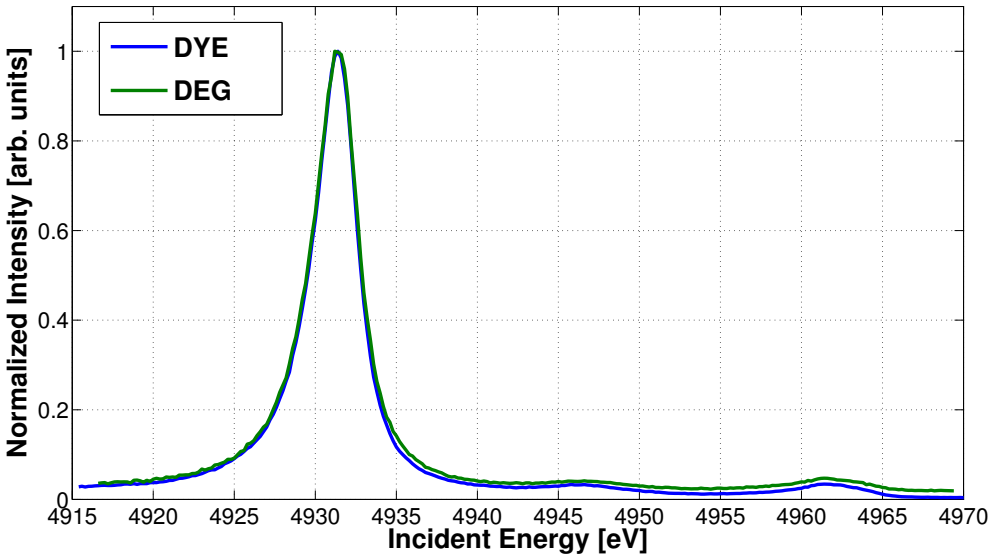

Figure 5.7: K_β emission line of TiO_2. Such feature is due to the emission of a photon generated from the electronic transition $3p \rightarrow 1s$. Also, at higher energies the satellite lines can be noted.

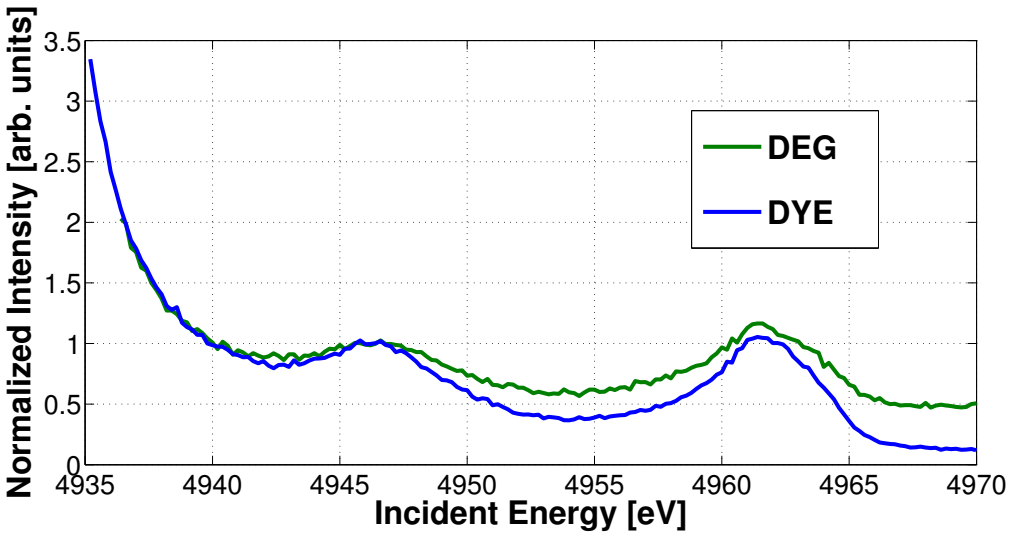

Figure 5.8: Satellites at the K_β emission line. Normalization is not applied yet and the background of the main K_β must be subtracted to perform a correct analysis (it has different intensity in the two cases because of a different amount of counts on the detector).

to have a relative 1 eV energy shift. This was present because of the different energy calibration of spectrometer and monochromator, as we could observe since references were also taken. For this reason such a shift was removed. Figure 5.7 shows the K_β main peak, together with the long tail containing the satellites. These are also shown in Figure 5.8 (no background removed yet).

RIXS. Resonant inelastic x-ray scattering is a technique useful to underline the

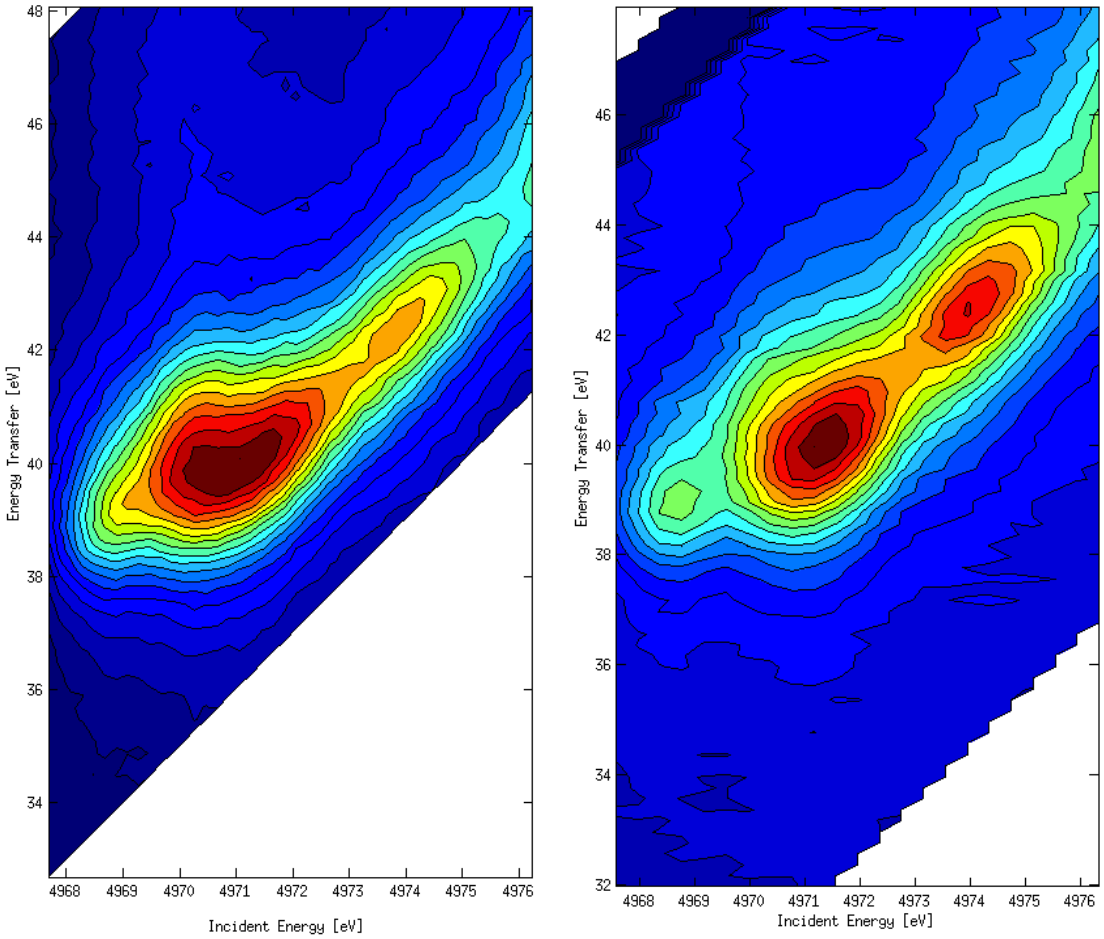

Figure 5.9: RIXS maps of DYE (left) and DEG (right) sample.

interconnections between x-ray absorption end emission. In the maps measured at ID26 on TiO_2 the region of the XANES pre-edge energies was scanned (about 4968-4976 eV) while the spectrometer was moving to collect the K_β main emission (emitted energy range 4920-4936 eV, or 32-48 eV of energy transfer). It should be noted that XANES and XES measurements were taken before the RIXS maps and they were independent to them, namely they were not cuts through them. Figure 5.9 shows the comparison between the two maps.

5.4 Discussion and analysis

XANES spectra show a number of features that shall be discussed. From the comparison between the nanostructured samples and the TiO_2 pure anatase pellets it is possible to notice that in the formers the pre-edge structure is much less pronounced. This is not a real effect but a self-absorption effect. Indeed, DYE and DEG samples are very thin and have low density, while the pellets are around 50 μm thick and very concentrated. A first estimation with X-count gives a value of SA of 0.231% for the nanostructured samples, while it gives 77.8% for a 50 microns-thick pellet. Unfortunately, it is not trivial to obtain self absorption-free measures on pellets because the particle size has to be below the order of magnitude of microns and thus the pellet must be strongly dilute. In Figure 5.5 a strong feature is also present around 4992 eV for the DEG sample. This is clearly an artifact (a diffraction peak from the substrate) and should not be considered.

Nevertheless, a couple of important differences between the DEG and DYE samples can be noted. First of all, the comparison between both DYE and DEG with their respective references show a general trend of the nanostructured samples to present less resolved and smoother features. This may be due to the fact that in the nanostructures the forest-like morphology results in a crystalline order which is extended on a shorter range than in the TiO_2 powder constituting the pellets (guaranteed from the producer to be 100% bulk anatase, i.e. behaving like a crystal). Also, it is important to remember that the nanostructured samples have a high surface to volume ratio and it is known that electronic structure at the surface can be different from the bulk one, because of the missing atoms (defects) and because of the reconstruction and relaxation effects. The most important effect is however the one observed in the inset of Figure 5.6, which shows how the peak A1 (for peaks nomenclature see [69]), present in the references and slightly noticeable in the DEG sample, almost disappears in the DYE sample. Being A1 the peak consisting in a quadrupole transition between the level $1s$ and the lowest unoccupied level above the Fermi energy, this seems to suggest that such a level is not totally unoccupied any more when the dye is attached on the TiO_2 surface, namely some electrons from the dye are displaced and occupy energy levels of the semiconductor. Actually, a slight

change in the curve slope is still noticeable, which means that this effect is very weak, above all because in the DYE sample there is also the broadening effect discussed above which can help flattening the peak. Therefore, although this effect seems to be present, it is rather difficult to estimate quantitatively. The reason is mainly the different experimental resolution, i.e. slightly worse for the DYE sample, which results in smoother features for it and thus it makes difficult to estimate to which extent a feature disappears because of resolution effect or of real physical effects. Another evidence of this smoothening is present on the white line of the DYE sample. In fact, Figure 5.6 shows the same position in energy for the highest edge both in the reference samples and in the DEG sample. However, this is not true for the DYE sample where this feature seems to move from 4987 eV to 4988 eV, together with a strong widening, which does not allow to understand whether the effect is real or not. A better understanding would require a modeling through DFT or multiplet theory calculations on a system of a dye deposited on a TiO_2 cluster, but this is beyond the goal of this thesis.

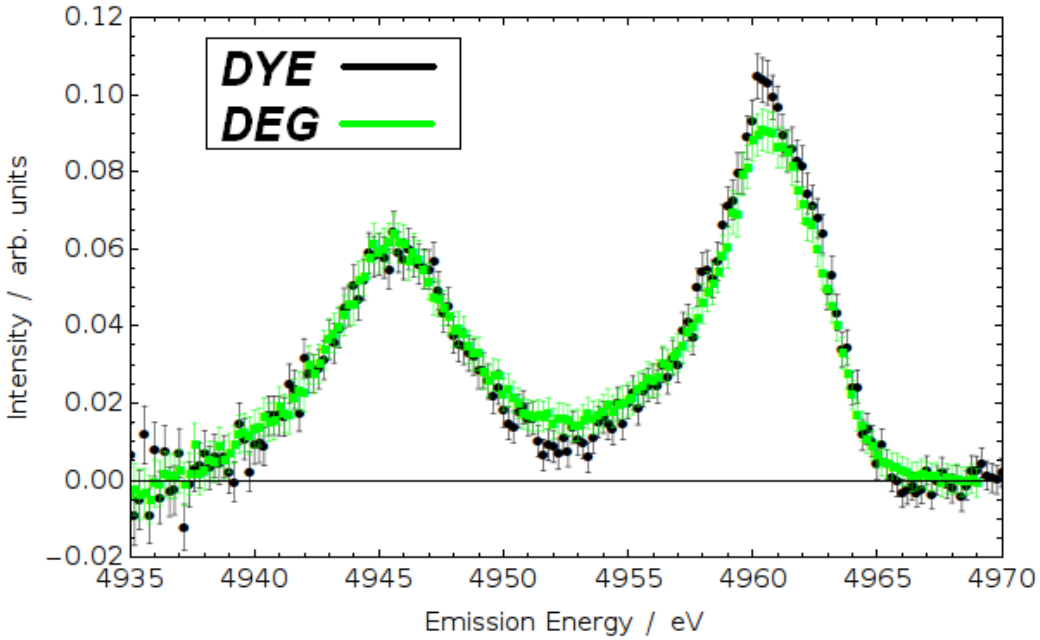

Figure 5.10: Background removed K_β satellite peaks for DYE and DEG samples. Black line shows the DYE sample, while the green one shows the DEG one. Error bars include the uncertainty coming from the procedures of merging, normalizing to the incident flux, normalizing in area and fitting of the K_β tail.

Concerning X-ray emission spectra, the K_β emission line does not show any significant difference between the DYE and DEG samples, meaning that nothing is affecting the 3p energy levels. To evaluate the differences between the satellites further analysis are necessary. Indeed, the background of the K_β main line must be removed with a fit with a Voigt function for them to be compared realistically. The fitting procedure was implemented in Mathematica, with a careful estimation of the expected error on every point, and the result is shown in Figure 5.10. The lowest energy peak, which is known to be due to transitions starting from orbitals mainly constituted by the oxygen ligands of the titanium atom (Figure 5.11), does not seem to show remarkable differences. The same cannot be said for the highest energy peak, which reflects the intensity of the emission between the highest occupied valence level (with mainly Ti 3d component) and a 1s core hole. Such a peak has in fact a higher

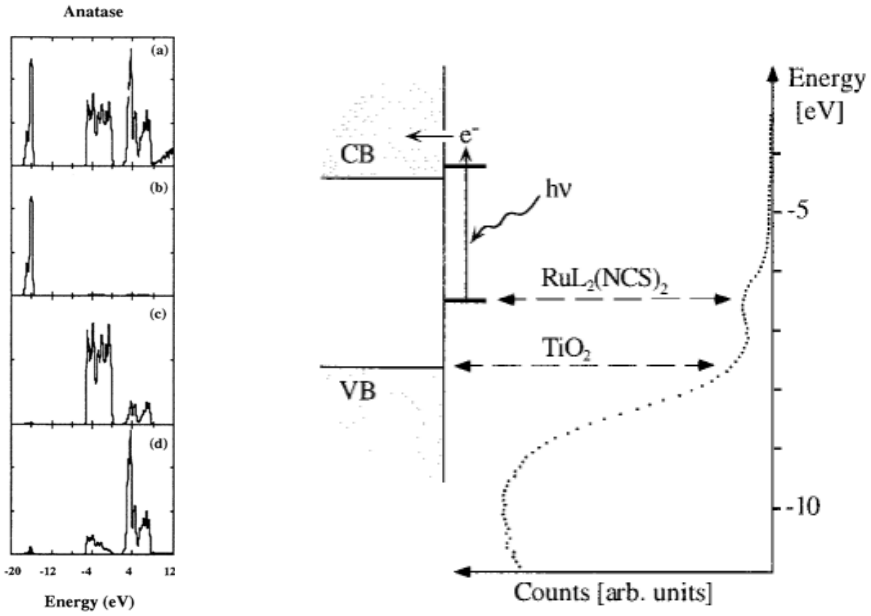

Figure 5.11: Left: calculated density of states of TiO_2, which shows the contribution from different orbitals: a) Total, b) O_{2s}, c) O_{2p} and d) Ti_{3d} [89]. Right: valence band spectrum of a nanostructured TiO_2 film sensitized with N3, where the HOMO levels of the dye are evident[79]. N3 and black dye have the same bonding with the anode, which means that no differences are expected in such an optical spectrum between the two.

intensity in the DYE sample. This would also need computational calculations to be explained properly, but an explanation can be given anyway taking into account the optical spectrum found in [79] and reported in Figure 5.11, which shows how the

contribution of the dye HOMO orbital is significant in the valence band structure, i.e. the dye introduces further energetic levels in the band gap (the HOMO) and below it (the other occupied orbitals). Hence, the peak height is enhanced because of the dye levels that contribute to the emission and overlaps in energy with the valence band levels of TiO_2.

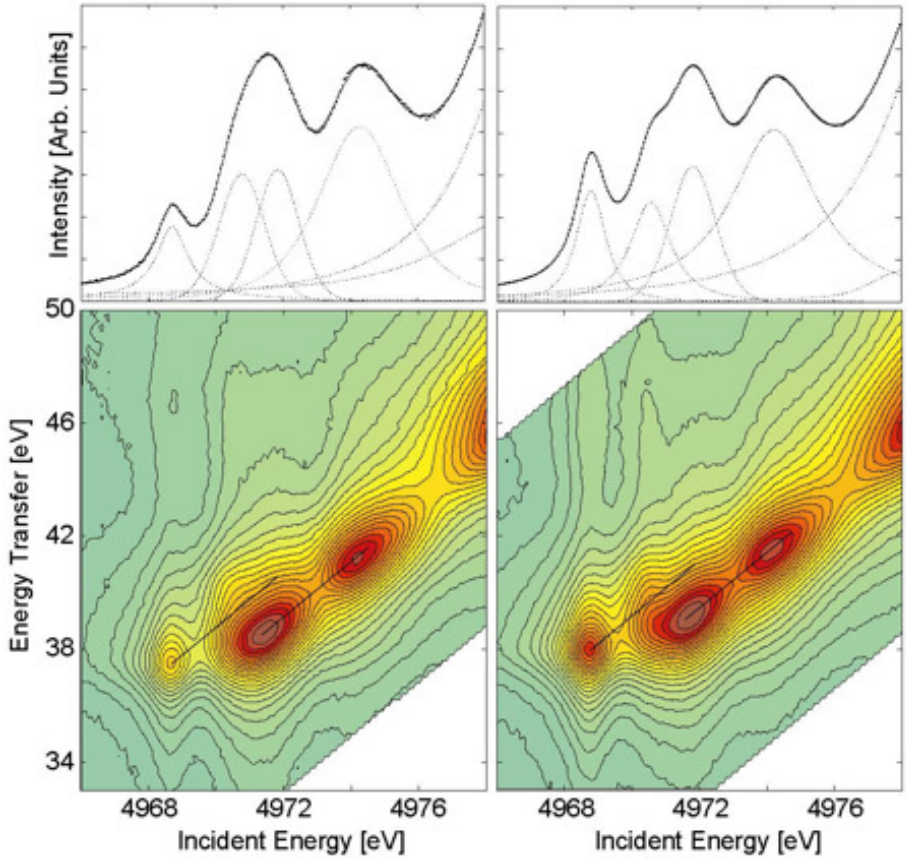

Figure 5.12: Reference RIXS map of TiO_2 anatase(right) and rutile(left) taken at ID26 (unpublished).

Finally, Figure 5.9 shows the RIXS maps taken for the DYE and DEG sample, while Figure 5.12, reported from unpublished data taken at ID26, is showed as a reference. From this an important fact should be underlined: the RXES plane for both rutile and anatase TiO_2 shows a displacement of the first two absorption features (A1 and A2) to higher energy transfer. The origin for this displacement has been treated in literature e.g. by Kotani et al.[70] and it is basically an effect of different interaction between the core hole in the intermediate state and the p and d orbitals which are differently influenced because of their different delocalization.

From Figure 5.9 we can see that the structure of DYE and DEG samples confirms the observations done for XANES on the pre-edge. In the DEG sample, 3 features can be clearly resolved, corresponding to the peaks A1, A3 and B. They show a good agreement with the reference map. The peak A2, difficult to see in the XANES spectra, is a bit easier to notice here because it occurs at a different energy transfer. In the DYE sample, instead, two features are clearly visible, even if the worse resolution of the incident energy is here evident (it shows up as a broadening in the diagonal direction), while the third one, corresponding to the peak A1, is only slightly noticeable and almost completely disappeared. However, the peak A2 is more evident here.

5.5 Conclusions

The data shown in this thesis aim to demonstrate how bulk-sensitive techniques can evidence differences between samples which only differ from one to another because of a surface treatment. This is possible because of the extremely high surface to volume ratio of the samples, which makes surface atoms a great percentage of the total. The discussion above clearly shows that differences arise in the electronic levels close to the Fermi energy when a dye monolayer is attached upon a nanostructured TiO_2 photoanode. Moreover, the combined use of different techniques can provide a complete picture of the electronic structure in the surroundings of a titanium atom in a certain energy region. However, the spectra show some problems too. In fact, the evidenced differences are small and they would need an accurate planning of the experiment in order to be observed without the influence of external factors, like the different energy resolution the experimental setup had for the samples described above. This was unavoidable because of the limited time that one has to measure at a synchrotron radiation facility, where the machine is shared between many people and where important scientific and economic factors also play. Nevertheless, the spectra previously shown are sufficient to demonstrate the interest of the topic and it would be extremely stimulating to compare them with numerical simulation, which could complete the experimental data explanation. The relevance of the matter is high

because of the commercial importance that the spreading of DSSCs will potentially have; the detailed understanding of the electronic configuration that a dye brings to a nanostructured semiconductor requires exploitation of different experimental techniques and it is a fundamental step to find the best engineering of the energy levels at the interface and thus a more efficient electron transfer.

Acknowledgements

I would like to thank many people that in different ways contributed to this thesis. First of all Pieter Glatzel, my boss at ID26, and all the beamline's staff (Erik, Mauro, Nikolay, Kristina, Janine...) for everything they taught me and for making me feel at home during my stay at ESRF. Secondly, thank to my professor Giacomo Ghiringhelli, which gave me the amazing chance to spend a period abroad, studying and working in one of the greatest scientific environments and which provided me all the support a student can need. Also, thank to Andrea Li Bassi and Carlo Casari for the samples they sent me and for the helpfulness they always showed me.

A special mention goes to my family, that never stopped sustaining me during these years spent at university and that I always felt so close, no matter if I was in a different city or in a different country. And of course to my girlfriend, which experienced how annoying a man can possibly be as a consequence of his pre-exam tension, but nevertheless always supported him.

Last but not least, thank to my friends. You have been the most important part of my life in these years, what makes life really worth living. Thus thanks to all Milan's friends: Bet, Caddi, Mez, Miki, Gio, Ale, Petra, Cri, Berri... To Erasmus friends: Hans, Matteo, Rodrigo, Valentin, Maria, Lotte... And Brescia's friends: Andre, Marcy, Niki, Cava, Fava, Bordon, Teo, Piter, Bricco, Gio, Bose, Marta, Viola, Franci&Franci, Cami, Ale...

List of Figures

Bibliography

[1] D.C. Koningsberger and R. Prins. *X-ray absorption: principles, applications, techniques of EXAFS, SEXAFS, and XANES*. Chemical Analysis: A Series of Monographs on Analytical Chemistry and Its Applications. Wiley, 1988.

[2] Uwe Bergmann and Pieter Glatzel. X-ray emission spectroscopy. *PHOTOSYNTHESIS RESEARCH*, 102(2-3, Sp. Iss. SI):255–266, DEC 2009.

[3] A. Kotani and S. Shin. Resonant inelastic x-ray scattering spectra for electrons in solids. *Reviews of Modern Physics*, 73(1):203, 2001.

[4] A.L. Linsebigler, G. Lu, and J.T. Yates Jr. Photocatalysis on tio2 surfaces: principles, mechanisms, and selected results. *Chemical Reviews*, 95(3):735–758, 1995.

[5] M. Grätzel. Solar energy conversion by dye-sensitized photovoltaic cells. *Inorganic Chemistry*, 44(20):6841–6851, 2005.

[6] M. Grätzel. Photoelectrochemical cells. *Nature*, 414(6861):338–344, 2001.

[7] F. Di Fonzo, CS Casari, V. Russo, MF Brunella, A. Li Bassi, and CE Bottani. Hierarchically organized nanostructured tio2 for photocatalysis applications. *Nanotechnology*, 20:015604, 2009.

[8] F. Sauvage, F. Di Fonzo, A. Li Bassi, CS Casari, V. Russo, G. Divitini, C. Ducati, CE Bottani, P. Comte, and M. Graetzel. Hierarchical tio2 photoanode for dye-sensitized solar cells. *Nano letters*, 2010.

[9] M.K. Nazeeruddin, P. Pechy, and M. Gratzel. Efficient panchromatic sensitization of nanocrystalline tio2 films by a black dye based on a trithiocyanato-ruthenium complex. *Chemical communications*, (18):1705–1706, 1997.

[10] European Synchrotron Radiation Facility (ESRF). http://www.esrf.fr/AboutUs.

[11] Wikipedia. http://it.wikipedia.org/wiki.

[12] ALS. X-ray data booklet. http://xdb.lbl.gov/.

[13] D.J. Griffiths. *Introduction to quantum mechanics*. Pearson Prentice Hall, 2005.

[14] J.J. Sakurai and S.F. Tuan. *Modern quantum mechanics*. Advanced book program. Benjamin/Cummings Pub., 1985.

[15] F. Groot and A. Kotani. *Core level spectroscopy of solids*. Advances in condensed matter science. CRC Press, 2008.

[16] M. Newville. Fundamentals of xafs. http://xafs.org/Tutorials.

[17] R.M. Eisberg and R. Resnick. *Quantum physics of atoms, molecules, solids, nuclei, and particles*. Quantum Physics of Atoms, Molecules, Solids, Nuclei and Particles. Wiley, 1985.

[18] C.T. Chantler, K. Olsen, R.A. Dragoset, J. Chang, A.R. Kishore, S.A. Kotochigova, and D.S. Zucker. X-ray form factor, attenuation, and scattering tables. http://www.nist.gov/pml/data/ffast/index.cfm, 2001.

[19] G. Bunker. *Introduction to XAFS: a practical guide to X-ray absorption fine structure spectroscopy*. Cambridge University Press, 2010.

[20] Simon R. Bare. Xanes measurements and interpretations. http://www.chm.colostate.edu/nel/Bare_XANES.pdf, 2005.

[21] G. Bunker. Element of xafs. http://gbxafs.iit.edu/training/xafsoverview.pdf.

[22] C. Bressler and M. Chergui. Ultrafast x-ray absorption spectroscopy. *Chemical reviews*, 104(4):1781–1812, 2004.

[23] A. Bianconi, L. Incoccia, and S. Stipcich. *EXAFS and near edge structure: proceedings of the International Conference, Frascati, Italy, September 13-17, 1982*. Springer series in chemical physics. Springer, 1983.

[24] D.E. Sayers, E.A. Stern, and F.W. Lytle. New technique for investigating non-crystalline structures: Fourier analysis of the extended x-ray—absorption fine structure. *Physical Review Letters*, 27(18):1204–1207, 1971.

[25] JJ Rehr and RC Albers. Scattering-matrix formulation of curved-wave multiple-scattering theory: Application to x-ray-absorption fine structure. *Physical Review B*, 41(12):8139, 1990.

[26] JJ Rehr and RC Albers. Theoretical approaches to x-ray absorption fine structure. *Reviews of Modern Physics*, 72(3):621, 2000.

[27] B. Ravel. A practical introduction to multiple scattering theory. http://cars9.uchicago.edu/xafs_school/APS_2005/Ravel_Theory.pdf, 2005.

[28] S. Bordiga, S. Coluccia, C. Lamberti, L. Marchese, A. Zecchina, F. Boscherini, F. Buffa, F. Genoni, and G. Leofanti. Xafs study of ti-silicalite: Structure of framework ti(iv) in the presence and absence of reactive molecules (h2o, nh3) and comparison with ultraviolet-visible and ir results. *The Journal of Physical Chemistry*, 98(15):4125–4132, 1994.

[29] Erik Gallo. Modification of the electronic structure of catalitycally active ti metal center upon molecular adsorption: a xas/xes study. Master's thesis, Università degli studi di Torino, April 2010.

[30] Wojciech Gawelda. *Time-resolved x-ray absorption spectroscopy of transition metal complexes*. PhD thesis, ÉCOLE POLYTECHNIQUE FÉDÉRALE DE LAUSANNE, 2006.

[31] G. Bunker. Basic techniques for exafs. http://gbxafs.iit.edu/training/errors_in_fluorescence.pdf, 1988.

[32] P. Glatzel, F.M.F. de Groot, and Uwe Bergmann. Hard x-ray photon-in photon-out spectroscopy. *Synchrotron radiation news*, 22(2):12–16, 2009.

[33] P. Glatzel and U. Bergmann. High resolution 1s core hole X-ray spectroscopy in 3d transition metal complexes - electronic and structural information. *COORDINATION CHEMISTRY REVIEWS*, 249(1-2):65–95, JAN 2005.

[34] P. Glatzel, M. Sikora, and M. Fernández-García. Resonant x-ray spectroscopy to study k absorption pre-edges in 3d transition metal compounds. *The European Physical Journal-Special Topics*, 169(1):207–214, 2009.

[35] M. Matsubara, T. Uozumi, A. Kotani, Y. Harada, and S. Shin. Polarization dependence of resonant x-ray emission spectra in early transition metal compounds. *JOURNAL-PHYSICAL SOCIETY OF JAPAN*, 69(5):1558–1565, 2000.

[36] L.J.P. Ament, G. Khaliullin, and J. Brink. Resonant inelastic x-ray scattering on spin-orbit coupled insulating iridates. *Arxiv preprint arXiv:1008.4862*, 2010.

[37] SG Chiuzbăian, G. Ghiringhelli, C. Dallera, M. Grioni, P. Amann, X. Wang, L. Braicovich, and L. Patthey. Localized electronic excitations in nio studied with resonant inelastic x-ray scattering at the ni m threshold: Evidence of spin flip. *Physical review letters*, 95(19):197402, 2005.

[38] G. Ghiringhelli, NB Brookes, E. Annese, H. Berger, C. Dallera, M. Grioni, L. Perfetti, A. Tagliaferri, and L. Braicovich. Low energy electronic excitations in the layered cuprates studied by copper l_3 resonant inelastic x-ray scattering. *Physical review letters*, 92(11):117406, 2004.

[39] J. Singh, C. Lamberti, and J.A. van Bokhoven. Advanced x-ray absorption and emission spectroscopy: in situ catalytic studies. *Chem. Soc. Rev.*, 2010.

[40] L.J.P. Ament, M. van Veenendaal, T.P. Devereaux, J.P. Hill, and J. Brink. Resonant inelastic x-ray scattering studies of elementary excitations. *Arxiv preprint arXiv:1009.3630*, 2010.

[41] L.J.P. Ament, G. Ghiringhelli, M.M. Sala, L. Braicovich, and J. van den Brink. Theoretical demonstration of how the dispersion of magnetic excitations in cuprate compounds can be determined using resonant inelastic x-ray scattering. *Physical review letters*, 103(11):117003, 2009.

[42] J.J. Sakurai. *Advanced Quantum Mechanics*. Pearson Education, Inc., 2006.

[43] A. Hofmann. *The physics of synchrotron radiation*. Cambridge monographs on particle physics, nuclear physics, and cosmology. Cambridge University Press, 2004.

[44] SOLEIL. Ring structure. http://www.synchrotron-soleil.fr/.

[45] G. Gautier. R.f. timing. http://www.esrf.fr/.

[46] D. Attwood. *Soft X-Rays and Extreme Ultraviolet Radiation: Principles and Applications*. Cambridge University Press, 2007.

[47] G. Margaritondo. *Introduction to synchrotron radiation*. Oxford University Press, 1988.

[48] Roberto Alonso Mori. *Sulfur-metal interaction in silicate glasses studied by x-ray spectroscopy*. PhD thesis, Università di Camerino, European synchrotron radiation facility, 2009.

[49] C. Gauthier, VA Solé, R. Signorato, J. Goulon, and E. Moguiline. The esrf beamline id26: X-ray absorption on ultra dilute sample. *Journal of Synchrotron Radiation*, 6(3):164–166, 1999.

[50] J.M. Rigal. Avalanche photodiodes at esrf. http://www.esrf.fr/files/Conferences/APDWorkshop/Jean-Marie_Rigal.PDF.

[51] N.W. Ashcroft and N.D. Mermin. *Solid state physics*. Holt-Saunders International Editions: Science : Physics. Holt, Rinehart and Winston, 1976.

[52] HH Johann. Die erzeugung lichtstarker röntgenspektren mit hilfe von konkavkristallen. *Zeitschrift für Physik A Hadrons and Nuclei*, 69(3):185–206, 1931.

[53] T. Johansson. Über ein neuartiges, genau fokussierendes röntgenspektrometer. *Zeitschrift für Physik A Hadrons and Nuclei*, 82(7):507–528, 1933.

[54] S. Takagi. Dynamical theory of diffraction applicable to crystals with any kind of small distortion. *Acta Crystallographica*, 15(12):1311–1312, 1962.

[55] European Synchrotron Radiation Facility (ESRF). Dabax library. http://www.esrf.fr/computing/scientific/dabax/.

[56] A. Brunetti, M. Sanchez del Rio, B. Golosio, A. Simionovici, and A. Somogyi. A library for x-ray-matter interaction cross sections for x-ray fluorescence applications. *Spectrochimica Acta Part B: Atomic Spectroscopy*, 59(10-11):1725–1731, 2004.

[57] CH Booth and F. Bridges. Improved self-absorption correction for fluorescence measurements of extended x-ray absorption fine-structure. *Physica Scripta*, 2005:202, 2005.

[58] L. Tröger, D. Arvanitis, K. Baberschke, H. Michaelis, U. Grimm, and E. Zschech. Full correction of the self-absorption in soft-fluorescence extended x-ray-absorption fine structure. *Physical Review B*, 46(6):3283, 1992.

[59] P. Pfalzer, J.P. Urbach, M. Klemm, S. Horn, A.I. Frenkel, and JP Kirkland. Elimination of self-absorption in fluorescence hard-x-ray absorption spectra. *Physical Review B*, 60(13):9335, 1999.

[60] B. Ravel and M. Newville. Athena, artemis, hephaestus: data analysis for x-ray absorption spectroscopy using ifeffit. *Journal of Synchrotron Radiation*, 12(4):537–541, 2005.

[61] D. Haskel. Fluo: Correcting xanes for self-absorption in fluorescence measurements. *Computer program and documentation [online]. Available from http://www. aps. anl. gov/xfd/people/haskel/fluo. html (accessed January 4, 2009)*.

[62] I. Repins, M.A. Contreras, B. Egaas, C. DeHart, J. Scharf, C.L. Perkins, B. To, and R. Noufi. 19.9%-efficient zno/cds/cuingase2 solar cell with 8.2% fill factor. *Progress in Photovoltaics: Research and applications*, 16(3):235–239, 2008.

[63] M. Bär, W. Bohne, J. Röhrich, E. Strub, S. Lindner, MC Lux-Steiner, C. Fischer, TP Niesen, and F. Karg. Determination of the band gap depth profile of the penternary cu (in (1-x) gax)(syse (1-y)) 2 chalcopyrite from its composition gradient. *Journal of applied physics*, 96(7):3857–3860, 2004.

[64] J. Yano, Y. Pushkar, P. Glatzel, A. Lewis, K. Sauer, J. Messinger, U. Bergmann, and V. Yachandra. High-resolution mn exafs of the oxygen-evolving complex in photosystem ii: structural implications for the mn4ca cluster. *Journal of the American Chemical Society*, 127(43):14974–14975, 2005.

[65] Y. Pushkar, J. Yano, P. Glatzel, J. Messinger, A. Lewis, K. Sauer, U. Bergmann, and V. Yachandra. Structure and orientation of the mn4ca cluster in plant photosystem ii membranes studied by polarized range-extended x-ray absorption spectroscopy. *Journal of Biological Chemistry*, 282(10):7198, 2007.

[66] http://cst-www.nrl.navy.mil/users/sullivan/TiO2/tio2.html.

[67] R.W.G. Wyckoff. *Crystal structures*. Number v. 1 in Crystal Structures. Interscience Publishers, 1963.

[68] ZY Wu, G. Ouvrard, P. Gressier, and CR Natoli. Ti and ok edges for titanium oxides by multiple scattering calculations: Comparison to xas and eels spectra. *Physical Review B*, 55(16):10382, 1997.

[69] R. Brydson, H. Sauer, W. Engel, JM Thomass, E. Zeitler, N. Kosugi, and H. Kuroda. Electron energy loss and x-ray absorption spectroscopy of rutile and anatase: a test of structural sensitivity. *Journal of Physics: Condensed Matter*, 1:797, 1989.

[70] T. Uozumi, K. Okada, A. Kotani, O. Durmeyer, JP Kappler, E. Beaurepaire, and JC Parlebas. Experimental and theoretical investigation of the pre-peaks at the ti k-edge absorption spectra in tio2. *EPL (Europhysics Letters)*, 18:85, 1992.

[71] D. Cabaret, Y. Joly, and H. Renevier. Pre-edge structure analysis of ti k-edge polarized x-ray absorption spectra in tio2 by full-potential xanes calculations. *Journal of Synchrotron Radiation*, 6(3):258–260, 1999.

[72] P.C. Angelomé, L. Andrini, M.E. Calvo, F.G. Requejo, S.A. Bilmes, and G.J.A.A. Soler-Illia. Mesoporous anatase tio2 films: Use of ti k xanes for the quantification of the nanocrystalline character and substrate effects in the photocatalysis behavior. *The Journal of Physical Chemistry C*, 111(29):10886–10893, 2007.

[73] O. Carp, CL Huisman, and A. Reller. Photoinduced reactivity of titanium dioxide. *Progress in Solid State Chemistry*, 32(1-2):33–177, 2004.

[74] R. Wang, K. Hashimoto, A. Fujishima, M. Chikuni, E. Kojima, A. Kitamura, M. Shimohigoshi, and T. Watanabe. Light-induced amphiphilic surfaces. *Nature*, 388:431–432, 1997.

[75] A. Fujishima. Electrochemical photolysis of water at a semiconductor electrode. *Nature*, 238:37–38, 1972.

[76] B. O'regan and M. Grätzel. A low-cost, high-efficiency solar cell based on dye-sensitized colloidal tio2 films. *Nature*, 353(6346):737–740, 1991.

[77] M. Grätzel. Perspectives for dye-sensitized nanocrystalline solar cells. *Progress in photovoltaics: research and applications*, 8(1):171–185, 2000.

[78] W. Shockley and H.J. Queisser. Detailed balance limit of efficiency of p-n junction solar cells. *Journal of Applied Physics*, 32(3):510–519, 1961.

[79] A. Hagfeldt and M. Grätzel. Molecular photovoltaics. *Accounts of Chemical Research*, 33(5):269–277, 2000.

[80] V. Thavasi, V. Renugopalakrishnan, R. Jose, and S. Ramakrishna. Controlled electron injection and transport at materials interfaces in dye sensitized solar cells. *Materials Science and Engineering: R: Reports*, 63(3):81–99, 2009.

[81] L. Patthey, H. Rensmo, P. Persson, K. Westermark, L. Vayssieres, A. Stashans, Å. Petersson, PA Brühwiler, H. Siegbahn, S. Lunell, et al. Adsorption of bi-isonicotinic acid on rutile tio (110). *The Journal of chemical physics*, 110:5913, 1999.

[82] A. Nattestad, AJ Mozer, MKR Fischer, Y.B. Cheng, A. Mishra, P. Bäuerle, and U. Bach. Highly efficient photocathodes for dye-sensitized tandem solar cells. *Nature Materials*, 9(1):31–35, 2009.

[83] D.B. Chrisey and G.K. Hubler. *Pulsed laser deposition of thin films*. Wiley-interscience publication. J. Wiley, 1994.

[84] PR Willmott and JR Huber. Pulsed laser vaporization and deposition. *Reviews of Modern Physics*, 72(1):315, 2000.

[85] Carlo S. Casari and Andrea Li Bassi. *Pulsed laser deposition of nanostructured oxides: from clusters to functional films*, volume 7 of *Advances in Laser and Optics Research*. Nova Science Publishers, Inc., 2011.

[86] P.M. Ossi. *Disordered materials: an introduction*. Advanced Texts in Physics. Springer, 2006.

[87] M. Fusi, E. Maccallini, T. Caruso, C.S. Casari, A. Li Bassi, C.E. Bottani, P. Rudolf, K.C. Prince, and R.G. Agostino. Surface electronic and structural properties of nanostructured titanium oxide grown by pulsed laser deposition. *Surface Science*, 2010.

[88] K. Westermark, A. Henningsson, H. Rensmo, S. Södergren, H. Siegbahn, and A. Hagfeldt. Determination of the electronic density of states at a nanostructured tio2/ru-dye/electrolyte interface by means of photoelectron spectroscopy. *Chemical physics*, 285(1):157–165, 2002.

[89] S.D. Mo and WY Ching. Electronic and optical properties of three phases of titanium dioxide: Rutile, anatase, and brookite. *Physical Review B*, 51(19):13023, 1995.